Digital Comprehensive Summaries of Uppsala Dissertations
from the Faculty of Science and Technology 2426

Searching for IceCube Neutrinos from the Death of Stars and Beyond: From MeV to PeV Energies

NORA VALTONEN-MATTILA

ACTA UNIVERSITATIS
UPSALIENSIS
2024

ISSN 1651-6214
ISBN 978-91-513-2185-1
urn:nbn:se:uu:diva-535303

UPPSALA
UNIVERSITET

Dissertation presented at Uppsala University to be publicly examined in Häggsalen, Ångströmlaboratoriet, Lägerhyddsvägen 1, Uppsala, Thursday, 19 September 2024 at 13:15 for the degree of Doctor of Philosophy. The examination will be conducted in English. Faculty examiner: Professor Amanda Weinstein (Iowa State University, Department of Physics & Astronomy).

Abstract
Valtonen-Mattila, N. 2024. Searching for IceCube Neutrinos from the Death of Stars and Beyond: From MeV to PeV Energies. *Digital Comprehensive Summaries of Uppsala Dissertations from the Faculty of Science and Technology* 2426. 121 pp. Uppsala: Acta Universitatis Upsaliensis. ISBN 978-91-513-2185-1.

The stellar death and its aftermath are compelling systems to study due to their extreme conditions and a rich array of observable messengers, such as photons, gravitational waves, and neutrinos. Neutrinos, as messengers of these systems, are particularly interesting due to their ability to traverse space unimpeded by interstellar debris, magnetic fields, or photons, thus preserving important information about the source, with different sites of production that influence the neutrino energy from nuclear processes in very dense and hot environments producing thermal MeV energy neutrinos to cosmic acceleration sites, where matter collides in shocks, producing high energy neutrinos in the O(>GeV-TeV). These neutrinos can be observed by neutrino telescopes such as the IceCube Neutrino Observatory, which has sensitivity for neutrinos from the MeV to >PeV energy ranges. In this thesis, we performed several searches, focusing on MeV neutrinos from Gamma Ray Bursts and Neutron Star Mergers, making use of information from other messengers such as photons and gravitational waves to inform our search, and >GeV neutrinos from Core-Collapse Supernovae. We produced MeV neutrino flux limits for GRB 221009A and provided detection horizon limits for >GeV neutrinos from Core-Collapse Supernovae. We also introduced a novel methodology for producing model-independent MeV neutrino flux and luminosity limits, developed a new IceCube MeV energy real-time fast analysis for the follow-up of external alerts from other observatories, and demonstrated how to search for MeV neutrinos correlated with gravitational waves.

Keywords: Neutrinos, Gravitational Waves, Neutron Star Mergers, Core-Collapse Supernova, Supernovae, High-Energy Neutrinos, Low-Energy Neutrinos, Astrophysical Neutrinos

Nora Valtonen-Mattila, Department of Physics and Astronomy, High Energy Physics, Box 516, Uppsala University, SE-751 20 Uppsala, Sweden.

© Nora Valtonen-Mattila 2024

ISSN 1651-6214
ISBN 978-91-513-2185-1
URN urn:nbn:se:uu:diva-535303 (http://urn.kb.se/resolve?urn=urn:nbn:se:uu:diva-535303)

To my best buddy, Muffy. Fly high in the heavens.

List of papers

This thesis is based on the following papers, which are referred to in the text by their Roman numerals.

I **Limits on Neutrino Emission from GRB 221009A from MeV to PeV Using the IceCube Neutrino Observatory**
R. Abbasi et. al. (Including N. Valtonen-Mattila)
The Astrophysical Journal Letters, 946:L26, 2023.

II **IceCube search for neutrinos from GRB 221009A**
K. Kruiswijk & B. Brinson & R. Procter-Murphy & J. Thwaites. & N. Valtonen-Mattila
Proceedings of Science, (ICRC 2023), 1511.

III **Realtime Follow-up of External Alerts with the IceCube Supernova Data Acquisition System**
N. Valtonen-Mattila
Proceedings of Science, (TAUP 2023), 236.

IV **IceCube Search of MeV Neutrino Bursts Correlated with Gravitational Waves from LIGO-Virgo-KAGRA**
N. Valtonen-Mattila
IceCube Internal Report, 202408001, 2024.

V **Prospects for Extending the Core-collapse Supernovae Detection Horizon using High-energy Neutrinos**
N. Valtonen-Mattila & E. O'Sullivan
The Astrophysical Journal, 945:98, 2023.

Reprints were made with permission from the publishers.

My contribution to each paper is briefly explained below:

Paper I
I led the MeV analysis for GRB 221009A, from analysis methodology to implementation. I authored the original draft of the MeV section and contributed to the revision of both the MeV section and the entire paper.

Paper II
I was responsible for the MeV section, including its methodology and implementation. I wrote the MeV neutrino section and participated in the overall revision of the paper.

Paper III
I led the analysis from planning through implementation, and I authored the paper. On the technical side, I developed the Northern Hemisphere software and managed the project involving the communication interface between the North and South Poles and the software deployed at the South Pole.

Paper IV
I led the analysis, from methodology development to software to results. I wrote the paper.

Paper V
I led the analysis, from methodology to software to results, and I wrote the paper along with the second author.

Cover page

Searching for neutrinos from the death of stars. Image taken in Great Sand Dunes, Colorado, U.S.A.
*By **Nora Valtonen-Mattila***

This thesis is partly based on the licentiate dissertation *"Extending the observational reach of core-collapse supernovae for IceCube using high-energy neutrinos"* by Nora Valtonen-Mattila, Uppsala University, 2022. Particularly parts of Chapters 1, 2, 4, and 5, Sections 3-3.1, and 6.5, with some edits and updates

Contents

List of Acronyms

AGN Active Galactic Nuclei
CC Charged Current
CJ Choked-Jet
CR Cosmic Ray
NS Neutron Star
CCSN Core-Collapse Supernova
CSM Circumstellar Material
DIS Deep Inelastic Scattering
DOM Digital Optical Module
EM Electromagnetic
GW Gravitational Wave
SNDAQ Supernova Data Acqusition
GRB Gamma-Ray Burst
sGRB Short Gamma-ray burst
LGRB Long Gamma-ray burst
BNS Binary Neutron Star
NSBH Neutron Star - Black Hole
BH Black Hole
HE High-Energy
LMC Large Magellanic Cloud
NC Neutral Current
PNS Proto-Neutron Star
PMT Photo-Multiplier Tube
SBO Shock Breakout
SN Supernova
NDAF Neutrino Dominated Accretion Flow
SNEWS Supernova Early Warning System
PNS Proto-Neutron Star
CBC Compact Binary Coalescence
HMNS Hyper Massive Neutron Star
LVK LIGO-Virgo-KAGRA
DIS Deep Inelastic Scattering
IBD Inverse Beta Decay
SMT Simple Multiplicity Trigger
BBH Binary Black Hole

1. Introduction

One of the most magnificent and powerful events in the universe is the death of a star, marking the end of billions of years of nuclear burning, where, in an instant, essential elements for life formation are blown into the cosmos with an immense burst of energy. Star deaths can be a spectacular optical event, visible to the naked eye if close enough, and observable through neutrinos, providing crucial information about extreme astrophysical conditions. The importance of neutrinos in Core-Collapse Supernova (CCSN) was first proposed by Colgate and White [1] in 1966. In 1978, Nadyozhin calculated the initial phase of neutrino luminosity [2], shedding light on what we might be able to expect. It was not until 1985, when Bethe and Wilson suggested that the stalled shock could be re-ignited through neutrinos [3], that the importance of the system dynamics was highlighted. Not long after, in 1987, the first Supernova (SN) [1] was observed not only via Electromagnetic (EM) messengers but also MeV neutrinos, detected by Kamiokande-II [4], Irvine-Michigan-Brookhaven detector [5], and Baksan [6]. This observation confirmed the role of neutrinos in such explosions and their connection to extreme nuclear densities [7, 8].

Since 1987, no other SN has been observed through neutrinos, despite advancements in neutrino detection capabilities, with large-scale Cherenkov light detectors like KM3NeT in the Mediterranean sea [9], IceCube Neutrino Observatory in the South Pole [10] or Super-Kamiokande in Japan [11]. In addition to searching for supernovae (SNe), we can also search for other astrophysical sources arising from the death of a star that, just like SNe, have extreme states of matter conducive for thermal cooling via neutrinos, such as Neutron Star (NS) mergers and Gamma-Ray Burst (GRB), which have not yet been observed with neutrinos. In searching for these sources, we can set competitive limits on the neutrino emission, and if they are very bright in neutrinos, we can hopefully detect them. Both NS mergers and GRB could produce MeV neutrinos, but also other messengers such as Gravitational Wave (GW) and EM emission that would help search for neutrinos through correlations between different messengers. However, unless the sources are very bright, even with the help of other messengers that can inform when to look for neutrinos, observing them remains challenging due to their small cross-section. All currently available neutrino observatories have a limited reach with MeV neutrinos to a few tens to hundreds of kpc [9, 12, 10, 11]. Within this detection horizon, SNe are rare, with about $\sim$2 per century in our galaxy [13, 14].

[1] The first supernova to be observed via telescopes in modern times.

Higher energy neutrinos (>GeV) are also considered to expand the detection horizon as their cross-section increases with energy.

This thesis focuses on searching for low-energy neutrinos from transients like GRBs and NS mergers using the IceCube Neutrino Observatory. It also explores IceCube's SN detection horizon with High-Energy (HE) neutrinos. IceCube, located at the South Pole, can detect HE neutrinos (>GeV) and has a sensitivity to bursts of low-energy neutrinos (O(MeV)) by detecting the Cherenkov light produced by neutrino interactions in ice and operated with a high duty cycle (>95%), observing the cosmos with a whole-sky coverage.

The thesis is structured as follows: In Chapter 2, *Astrophysical Messengers*, we will cover the background of multi-messenger astronomy and introduce neutrinos. In Chapter 3, *Death of Stars and Beyond*, the neutrino production mechanisms for SNe, GRBs, and neutron star mergers will be covered from the lowest-energy neutrinos that are produced via nuclear processes to the HE neutrinos that are produced via acceleration mechanisms. In Chapter 4, *How to Observe Neutrinos from Transients*, we will discuss how neutrinos are observed from MeV to PeV energies, emphasizing water Cherenkov detection techniques. In Chapter 5, *IceCube Observatory*, we will cover the detector, from how it can observe neutrinos in both low and high energy regimes, highlighting the low-energy data acquisition system that monitors in real-time for supernovae called Supernova Data Acqusition (SNDAQ) System. In Chapter 6, *Search Strategies for MeV and GeV-TeV Neutrinos*, we present summaries for the analyses attached to this thesis's publications. Finally, we end this thesis with a summary and conclusions to this body of work.

2. Astrophysical Messengers

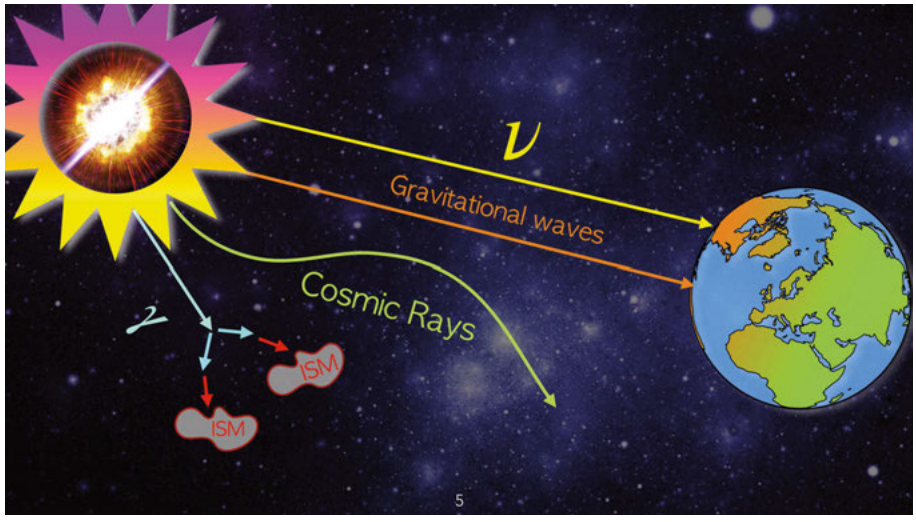

Figure 2.1. The different astrophysical messengers that can come from a source. Note how cosmic rays can get deflected by magnetic fields and photons can get absorbed by the interstellar medium (ISM).

We live in an era where technological advancements allow us to observe neutrinos through many messengers produced at cosmological distances. These messengers come in many forms (Fig. 2.1) such as GW, which are ripples in space-time, EM emissions ranging from radio waves to gamma rays, Cosmic Ray (CR) (highly energetic protons and nuclei) traveling from sites of acceleration, and neutrinos, which are neutral particles that interact through the weak forces and gravity. In this multi-messenger era, we can use all these forms of data to understand astrophysical sources and the fundamentals of our universe.

The field of multi-messenger astronomy began in the 1960s with the detection of solar neutrinos by John N. Bahcall and Raymond Davis Jr. in the Homestake experiment [15]. However, it wasn't until 1987 that, for the first time, an extragalactic astrophysical event was through multi-messengers, both EM emission and neutrinos: The famous supernova SN 1987A, located in the Large Magellanic Cloud (LMC). Two water Cherenkov detectors, Kamiokande-II and IMB, detected 19 low-energy neutrinos [4, 5], while the scintillator detector Baksan observed five neutrinos [6] totaling 24 neutrinos. These observations improved our understanding of the role of neutrinos in CCSNe [16] and

the interactions of the ejecta with the surrounding material [7, 17]. Subsequent observation with the ALMA radio array revealed particle acceleration in SN 1987A [18]. Some decades after this event, in 2013, the IceCube Neutrino Observatory provided the first evidence of HE astrophysical neutrinos [19], and in 2015, LIGO detected GWs for the first time [20]. A significant milestone in multi-messenger astronomy occurred in 2017 with the detection of the neutrino event IC-170922A by IceCube, with an energy of 290 TeV [21]. A coordinated follow-up search with electromagnetic telescopes revealed an association with a flaring blazar, TXS 0506+056 [21] in the GeV-TeV gamma-rays. This association suggested hadronic interactions [22], identifying the blazar as a potential source of CR, which are particles with the highest known energies in the universe. That same year, GWs from the NS merger GW170817 was detected by LIGO [23], associated with GRB 170817A detected by Fermi-GBM [24], and the first kilonova AT 2017gfo [25]. This kilonova event provided the first direct observation of r-process nucleosynthesis [26]. More recently, in 2022, IceCube found evidence of neutrino emission from the galaxy NGC 1068 [27], and in 2023, from our Galactic plane [28].

These discoveries demonstrate the great potential of multi-messenger astronomy; however, not all messengers can survive the journey from their origin to Earth. CR, being charged particles, are influenced by intergalactic magnetic fields that bend their paths, making it difficult to trace their sources. Similarly, photons generated in astrophysical environments interact with dust and the interstellar medium, leading to absorption and scattering that limit their effectiveness as probes, such as for identifying accelerator sites. GWs are only produced in compact sources such as mergers [29], offering limited information. Neutrinos, on the other hand, are produced in CR accelerator sites and nuclear reactions, including the Sun, SNe, Active Galactic Nuclei (AGN), and cataclysmic events like mergers. Neutrinos can provide excellent pointing accuracy[1], and are crucial for understanding the origin of CR, which remains a major mystery in astroparticle physics. They can also help probe extremely dense and hot environments, which cannot be replicated in laboratories. This thesis will focus on sources capable of producing low- to high-energy neutrinos, exploring their significance, production mechanisms, and observation methods.

2.1 Neutrinos

Neutrinos belong to the lepton family of elementary particles as described by the Standard Model, which details the fundamental particles and their interactions with three out of the four[2] fundamental forces. Particles are classified as

[1] Although gravitational waves can provide us with directionality, the uncertainty is typically larger than for neutrinos.

[2] The fourth one being gravitational forces

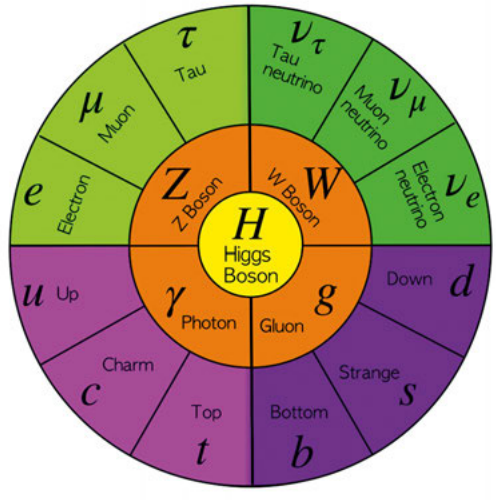

Figure 2.2. Standard model particles, showing the three generations of matter for quarks (purple) and leptons (green), where the darker purple and darker green represent the partner pair, as well as the force mediators (orange) and force carrier (yellow).

fermions (matter constituents) and bosons (interaction mediators/force carriers) (see Fig. 2.2). Fermions can be divided into quarks and leptons, each with three generations; Generation I comprises up and down quarks, electrons, and electron neutrinos. Generation II comprises charm and strange quarks, muons and muon neutrinos. Finally, Generation III comprises top and bottom quarks, tauons, and tau neutrinos. Neutrinos come in three flavors (ν_e, ν_μ, ν_τ), are electrically neutral, lack a color charge, and interact only via the weak force and gravity. The vector bosons mediate the weak force interactions: $W^\pm$ for Charged Current (CC) interactions and Z^0 for Neutral Current (NC) interactions (see Fig. 2.3). Because of charge conservation, a partner lepton of the same flavor is produced in CC interactions. Neutrinos have a tiny mass, which we know due to neutrino oscillation, a phenomenon where a neutrino of one flavor converts to another. This oscillation occurs because neutrinos travel as a superposition of three mass eigenstates. Neutrino oscillation was confirmed in 1988 by the Super-Kamiokande experiment [30] through the observed deficit in atmospheric muon neutrinos, and in 2001 by the Sudbury Neutrino Observatory using solar neutrinos [31, 32]. This work led to the awarding of the 2015 Nobel Prize in Physics[3]. In the following chapters, we will explore the production sites of neutrinos, their interaction channels, and the methods we use to observe them.

[3] `https://www.nobelprize.org/prizes/physics/2015/press-release/`

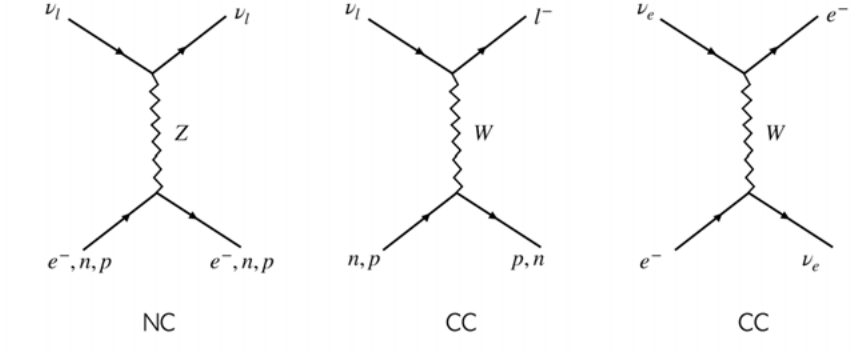

Figure 2.3. Feynman diagrams for the different interactions, where the time axis is from left to right. The left figure shows a NC interaction, where ν_l is the neutrino of flavor $l = e, \nu, \tau$, and e^-, p, n are electrons, protons and neutrons. The middle and right panels show CC interactions, where the middle depicts the quasi-elastic scattering of ν_l on nucleons, and the right panel shows the quasi-elastic scattering of ν_e on electrons.

3. Death of Stars and Beyond

> The nitrogen in our DNA, the calcium in our teeth, the iron in our blood, the carbon in our apple pies were made in the interiors of collapsing stars. We are made of starstuff.
>
> *Carl Sagan in Cosmos, 1980*

Star formation begins when clouds of interstellar matter, primarily hydrogen, and some helium, become large enough for self-gravity to cause the gas to fall inward toward the center of gravity. This infall happens because the gravitational energy exceeds the thermal energy, leading to the cloud's collapse and increasing the density and pressure at the center. The minimum mass required to trigger the collapse is given by the Jeans criterion [33], which quantifies the gravitational pressure required to overcome the internal pressure. The star formation process involves multiple phases of collapse and stabilization. When the gravitational pressure overcomes the internal pressure, adiabatic compression will increase the internal pressure and temperature, slowing the collapse. At some point, when the density becomes sufficiently high, a protostar forms. The protostar's evolution is controlled by its adjustment to the collapse and the burning of primordial deuterium into hydrogen. Once the temperature reaches several million Kelvin (K), hydrogen fusion begins, forming helium. Depending on the star's mass, hydrogen fusion becomes the only energy source, and the star enters main sequence[1], where it remains for many millions of years. For low-mass stars ($M \lesssim 4M_\odot$, where $M_\odot$ is the solar mass), the evolution over billions of years leads them to become carbon-oxygen white dwarfs, having only burned helium. Intermediate-mass stars, up to $\approx 8M_\odot$, end up as oxygen-neon-magnesium white dwarfs after entering the carbon-burning phase. In both cases, however, there is insufficient energy to overcome the Coulomb barrier of heavier nuclei.

For massive stars $\gtrsim 8M_\odot$, the fate is significantly different. Due to their higher mass and gravitational attraction, these stars reach temperatures sufficient for carbon burning and are hot enough to fuse heavier elements. Progressively, the time required for each element's fusion process decreases until iron is reached. Since iron has one of the highest binding energies per nucleon, its fusion is endothermic, meaning that it absorbs energy rather than releasing it, leading to the termination of the fusion process at this element. What

[1] Main sequence is a classification of the star based on the luminosity against the surface temperature, and it can indicate the life cycle and evolution of a star.

occurs after a star reaches iron is detailed in Section 3.1, which discusses the explosion mechanism, focusing on neutrino production for both low and high energies [2]. In Section 3.2, we will explore NS–remnants of stars in certain scenarios–and NS mergers, which are sites of supra-nuclear densities and can produce significant amounts of low-energy neutrinos. Finally, in Section 3.3, we will cover GRBs, which can result from massive stars collapsing or NS mergers and are also sites of low-energy neutrino production.

3.1 Supernovae

It all begins with Chandrasekhar's mass limit, M_{Ch}, which determines the maximum mass at which a star can counteract the gravitational pull with the electron degeneracy pressure. It is defined as

$$M_{Ch} = 5.38\bar{Y_e}^2 \left(1 + \left(\frac{\bar{s_e}}{\pi \bar{Y_e}}\right)^2\right) M_{\odot}, \tag{3.1}$$

where $\bar{Y_e}$ is the mean electron fraction per baryon and $\bar{s_e}$ is the mean electron entropy, highlighting that this mass limit is not a static quantity. When the mass of the iron core exceeds M_{Ch}, the end of the fusion process can trigger a spectacular event called a supernova, marking the final stage of stellar evolution, where elements required for star formation and life are ejected into the cosmos. SNe are categorized into two main types, thermonuclear and core-collapse, and are typically classified based on their electromagnetic spectral features [37] following the Minkowski-Zwicky system [38]. As shown in Fig. 3.1, the first distinction is whether the hydrogen lines are present or absent: Type I SNe lack hydrogen lines, and Type II have them. From there, we can further categorize them as with the silicon lines, where the absence indicates a thermonuclear explosion or Type Ia, and the presence of the silicon lines indicates that the explosion mechanism was a core collapse. We can then further categorize the core-collapse SNe depending on the presence or absence of helium lines or light curves. Types Ib, Ic, and IIb are associated with Wolf-Rayet stars, which are typically massive O(15-50$M_{\odot}$) [39] at the end of their lifecycles. These types of SNe have lost most if not all of their hydrogen and/or helium envelope due to very high wind velocities by the time of the explosion [39]. In contrast, Types IIn, II-P, and II-L, the more common types of CCSNe, retain their hydrogen envelope at the time of the explosion. Their different naming convention arises from the lightcurve shape and spectra, with II-P standing for a *plateau* in the lightcurve, II-L having a *linear* evolution of its lightcurve. Finally, IIn stands for *narrow* hydrogen lines in their spectra.

Thermonuclear SNe are believed to occur when a white dwarf accretes matter from a companion star, such as another white dwarf. However, Type Ia

[2]For a complete description of stellar evolution and formation, refer to [34, 35, 36].

supernovae are not considered promising sources of significant neutrino production [40]. Only a few events from a nearby Type Ia explosion (within a few kpc) would be detectable by large-scale neutrino observatories [41]. In contrast, CCSNe are believed to produce vast amounts of both low- and high-energy neutrinos. Therefore, this thesis will only focus on CCSNe types.

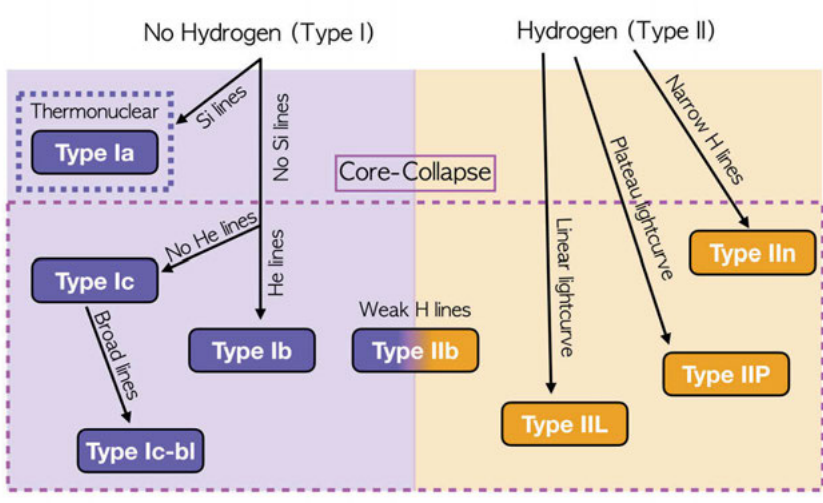

Figure 3.1. Supernova classification scheme. Depending on which spectral lines and/or lightcurve shape is observed, they can be categorized as Type I or Type II, with further sub-categories.

3.1.1 Core-collapse explosion

CCSNe are a type of SNe that can produce a high flux of MeV neutrinos through nuclear processes. These neutrinos offer a unique real-time view into the dynamics of stellar collapse, as they are one of the two direct probes, alongside GWs, that can escape the dense inner region of the star [42]. Observing MeV neutrinos could provide an early warning signal in multi-messenger astronomy since their detection precedes the arrival of photons. This early signal can help optical telescopes capture the Shock Breakout (SBO) (see Fig. 3.2), which can last about one hour [43]. Observing the SBO is crucial for understanding the explosion and progenitor properties, including the progenitor's radius, mass, energy release [44, 45] and pre-explosion mass-loss, which aids in progenitor classification [42, 43]. An existing early warning system, the Supernova Early Warning System (SNEWS) [46], facilitates this process. SNEWS is a public alert system where multiple neutrino experiments report candidate MeV neutrino bursts. When a potential burst is detected, it is reported to a central server, which then disseminates the alert to the astronomical community. Besides providing early warnings, observing MeV neutrinos is

also valuable for understanding SN dynamics and identifying those that ended in a Black Hole (BH)[37, 47].

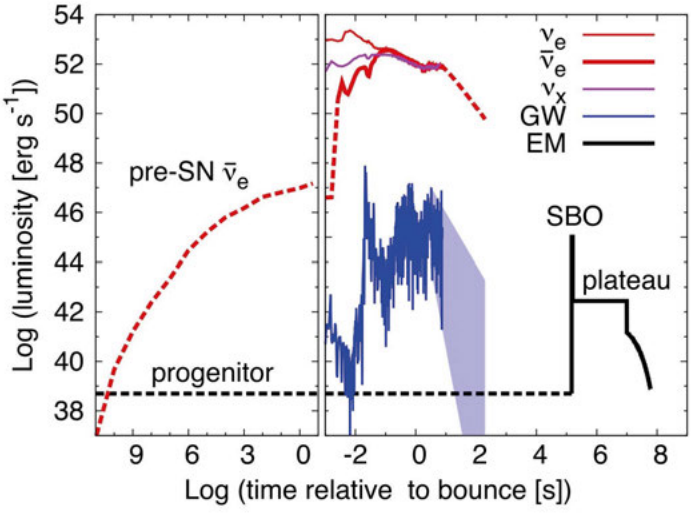

Figure 3.2. The luminosity as a function of time for different messengers from a CCSN. We can see how the neutrinos and gravitational waves would appear before the SBO electromagnetic signal. Reproduced from [48].

To understand the production of MeV neutrinos and their significance, we can look at the stages of core collapse and explosion that create an environment conducive to high fluxes of these neutrinos. The discussion on this topic will be brief here, enough to understand the contrasting differences between the low- and high-energy neutrino production in CCSNe. Core collapse begins when silicon fusion produces iron peak nuclides, forming an iron core surrounded by lighter element shells. Until this point, the gravitational pressure of the core was balanced by the endothermic pressure from fusion reactions. The core, which continues to grow due to fusion in the surrounding silicon shell, is supported by electron degeneracy pressure until it reaches Chandrasekhar limit, $M_{Ch} \gtrsim 1.2 - 1.4 M_{\odot}$. At this point, the electron degeneracy pressure can no longer counteract gravitational pressure, leading to gravitational instability and the onset of collapse. As the core contracts, its temperature rises, generating thermal photons that photodisintegrate iron nuclides into α-particles and free nucleons (neutrons, protons). From this moment on, the rest of the star's lifetime is dominated by neutrino processes.

3.1.2 Low-Energy Neutrinos

Iron photodisintegration during the initial phase of stellar collapse results in many free nuclides. As the core density increases, electron capture becomes

the dominant process (see Table 3.1 for key reactions), producing electron neutrinos. These neutrinos initially escape, reducing the lepton number and accelerating the collapse (see upper diagrams from Fig. 3.3). However, neutrinos are eventually trapped as the collapse progresses because their diffusion time exceeds the collapse time due to NC scattering of ν_e with heavy nuclei.

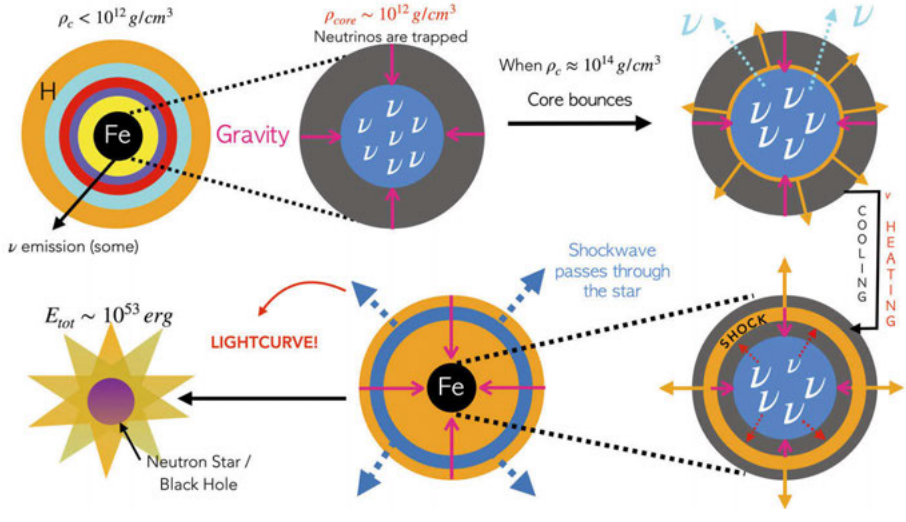

Figure 3.3. Condensed view of the core-collapse supernova process, where we can see the key moments in the collapse, along with the different densities.

When the core reaches nuclear matter density ($\rho_c \approx 10^{14}$ g/cm^3), the equation of state becomes stiffer due to nucleon repulsion, causing the inner core to rebound. This rebound generates a shockwave that moves outward, expelling the infalling layers. However, this shockwave alone is insufficient to trigger a supernova explosion as it loses energy by dissociating iron. Simulations indicate that purely hydrodynamic mechanisms are inadequate [49, 50]. Instead, delayed neutrino heating is a favored mechanism for reviving the shock and causing the explosion [51, 50]. As the shockwave expands, electron capture generates more ν_e, which remain trapped behind the shockwave until it reaches the neutrinosphere[3], about 1-2 ms after bounce. This release of neutrinos causes a sudden reduction in lepton number, leaving an abundance of positrons, resulting in shock stagnation.

In order to revive the shock, the gravitational binding energy must be released. As plasma infall continues, the pressure and temperature behind the shock increases, disintegrating heavy nuclei into free nucleons. Now, with an excess of neutrons, positron capture takes place, producing electron antineutrinos. Heavy lepton neutrinos are produced through pair production as the

[3]Neutrinospheres are regions where neutrinos undergo one last interaction before escaping.

Beta processes	
β^- decay	$(A,Z) \rightarrow (A-1,Z+1)+e^-+\bar{\nu}_e$
e^- and ν_e capture by nucleons	$e^-+p \leftrightarrow n+\nu_e$
e^+ and $\bar{\nu}_e$ capture by nucleons	$e^++n \leftrightarrow p+\bar{\nu}_e$
e^- and ν_e absorption by nuclei	$e^-+(A,Z) \leftrightarrow (A,Z-1)+\nu_e$
Thermal pair production and annihilation processes	
Nucleon-nucleon Bremsstrahlung	$N+N \leftrightarrow N+N+\nu+\bar{\nu}$
Electron-positron pair process	$e^++e^- \leftrightarrow \nu+\bar{\nu}$
Neutrino scattering	
Neutrino scattering with nuclei	$\nu+(A,Z) \leftrightarrow \nu+(A,Z)$
Neutrino scattering with nucleons	$\nu+N \leftrightarrow \nu+N$
Neutrino scattering with $e^\pm$	$\nu+e^\pm \leftrightarrow \nu+e^\pm$
Neutrino-neutrino reactions	
Neutrino pair annihilation	$\nu_e+\bar{\nu}_e \leftrightarrow \nu_x+\bar{\nu}_x$
Neutrino scattering	$\nu_x+(\nu_e,\bar{\nu}_e) \leftrightarrow \nu_x+(\nu_e,\bar{\nu}_e)$

Table 3.1. *Important neutrino processes in CCSNe and other transients.* $\nu_x = \nu_\mu, \bar{\nu}_\mu, \nu_\tau, \bar{\nu}_\tau$, *N = nucleon.* ν *= all flavors. A = mass number (total protons and neutrons), Z = atomic number (number of protons).*

core temperature rises. The interplay of energy loss and gain forms a cooling and gain layer around the neutrinosphere, where neutrino energy deposition helps to revive the shock. The most important reactions that deposit the most energy behind the shock are beta processes, also referred to as URCA processes[4]. Upon shock revival, an explosion occurs, heating the outer shells and synthesizing radioactive isotopes like ^{56}Ni. As the Proto-Neutron Star (PNS) cools, it emits energy through neutrinos, resulting in a mass outflow known as the neutrino wind. After the explosion, the PNS enters the Kelvin-Helmholtz cooling phase, where it continues to lose its remaining gravitational energy via neutrinos over approximately 10 seconds.

Low-Energy neutrino lightcurves

There have been many efforts to simulate the hydrodynamical conditions [50, 53, 54, 55, 8] in order to explain the explosion mechanism, requiring theoretical input of equations of state, neutrino physics, progenitor conditions, magnetohydrodynamics of the stellar plasma, and relativistic gravity to obtain a simulation of the signal output such as optical lightcurves, spectra, neutrinos or gravitational waves. One such example of simulations is the theoretical prediction of the neutrino lightcurves.

[4]This name comes from Casino de Urca, where George Gamow and Mario Schenberg noticed the rapid loss of money. In this case, the process of neutron decay that produces a proton and a $\bar{\nu}_e$ is only followed by a proton-electron capture which emits another ν_e, thereby rapidly losing energy [52]

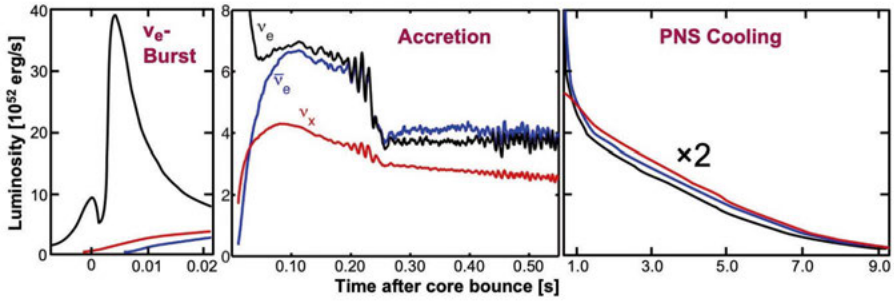

Figure 3.4. Neutrino luminosity evolution for different flavors as a function of the time post-core bounce, separated into three stages: Left panel) Neutrino burst post-core bounce. Middle panel) Shock stagnation and neutrino heating emission. Left panel) PNS neutrino cooling (the plotted values are scaled up by a factor of 2). Reproduced from [56].

In the pre-shock breakout phase (left panel of Fig. 3.4), the luminosity of ν_e rises briefly due to electron capture, but it is too low for detection. A sudden dip occurs when neutrino trapping sets in, followed by a significant burst in luminosity. The luminosity for $\bar{\nu}_e$ and the other flavors ν_x remains minimal due to low positron capture and pair production rates. In the post-bounce phase (middle panel), the ν_e luminosity declines and then plateaus. The $\bar{\nu}_e$ luminosity increases due to positron capture in the hot PNS mantle alongside electron capture. The ν_x luminosity also rises due to nucleon Bremsstrahlung. Finally, during the cooling phase (right panel), ν_x slightly dominates as the core releases 90% of its gravitational binding energy over approximately 10 seconds through neutrino emission. Most neutrinos have mean energies between 9-18 MeV. Some models also propose shock acceleration within the SN shockwave, where heavy lepton neutrinos with energies around $\sim 100 - 200$ MeV could be produced [57].

SN 1987A

The first, and to date, only SN to be observed through neutrinos is SN 1987A. This SN originated from an $18M_\odot$ blue giant and was a Type II SN visible to the naked eye in the LMC, located 50 kpc away from our Galaxy [7]. On February 23rd, 1987, it was detected by two water Cherenkov detectors, Kamiokande-II [4] and IMB [5], which recorded 19 low-energy $\bar{\nu}_e$ (O(MeV)) neutrino candidates over a 13-second interval, consistent with the delayed-neutrino heating model. Additionally, the scintillator detector Baksan observed neutrino candidates coinciding with those detected by the two water Cherenkov detectors [6], bringing the total to 25 neutrinos (Fig 3.6).

In addition to neutrinos, SN 1987A was the first SN to be observed through multi-wavelength EM observations due to its proximity [7]. These observa-

Figure 3.5. Optical image of the supernova SN 1987A. Right image) SN 1987A image taken after exploding in February 1987. Left image) SN 1987A image taken prior to the explosion, highlighted by an arrow. Reproduced from [58].

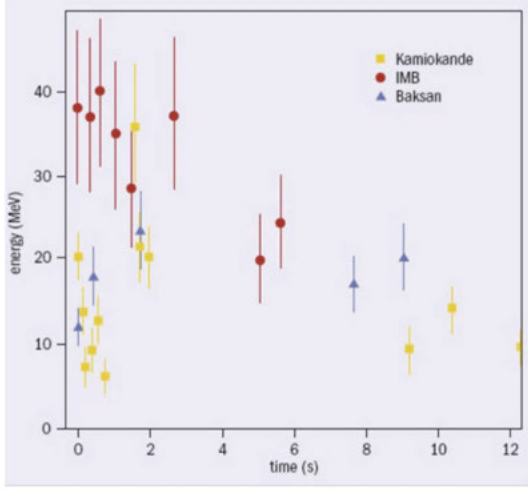

Figure 3.6. The SN 1987A neutrino candidates observed by Kamiokande, IMB and Baksan. The y-axis shows the neutrino energy and the x-axis the time of the observation. Reproduced from [59].

tions allowed for detailed studies on the energetics and the light curve, providing a deeper understanding of the progenitor and core collapse. They also offered insights into dust formation and Circumstellar Material (CSM) emission before the explosion by analyzing the evolution of the light curve [7]. Furthermore, the interaction between the shock and the surrounding CSM led to studies of HE (O(GeV)) neutrino candidates that Kamiokande-II and IMB

observed after the MeV neutrino events, where a 3σ significance was found [60].

3.1.3 High-Energy Supernova Neutrinos

So far, we have only discussed the mechanism of thermal neutrino production. However, there is also the mechanism of interaction-powered supernovae, where the ejecta or jetted material shocks with a medium, accelerating protons that produce HE neutrinos immediately after or with a delay relative to MeV neutrinos. Most CCSNe likely have some degree of shock interaction with the CSM [61, 62, 63, 64, 65] because the observed EM luminosities from these sources cannot be fully explained by radioactive decay alone, such as the decay of ^{56}Ni which is produced during the explosion. This shock-interaction mechanism relies on particle acceleration, with proposed scenarios like relativistic jets produced during the collapse, such as those from low-luminosity GRBs [66] or post-collapse such as SN ejecta-CSM interaction [67], or even pulsar winds from fast-rotating NS interacting with the supernova remnant [68]. All these scenarios typically model emission through the diffusive shock acceleration of charged particles. In this Section, we will cover the HE neutrino production mechanism, focusing on two sites of acceleration: the interaction of the ejecta with CSM and the interaction of a jet with material, where the jet becomes choked and only neutrinos can escape.

High-energy neutrino production

High-energy neutrinos are produced via the decay of mesons that are generated when CRs are accelerated to high energies. The exact mechanisms by which CRs achieve these very high energies are not entirely understood, but several theories have been proposed. These include the inductive acceleration mechanism or one-shot mechanism, where particles are continuously accelerated by an ordered magnetic field [69], and the diffusive acceleration mechanism (Fermi first order), where the particles are accelerated in bursts as they interact with highly magnetized regions [69]. In the latter case, the kinetic energy from the moving magnetized plasma is transferred to individual charged particles linearly with each collision. Fermi first order is currently the most promising theory to explain CR acceleration [70, 64, 71].

Interactions that produce neutrinos

Photohadronic Interaction

When CRs interact with the surrounding radiation, the interaction can lead to a $\Delta^+(1232)$ resonance or Δ^0, which then decays into a neutrino. The reactions involved in this process are;

$$p+\gamma \rightarrow \Delta^{+} \begin{cases} \rightarrow n+\pi^{+} \rightarrow n+\mu^{+}+\nu_{\mu} \rightarrow n+e^{+}+\nu_{e}+\bar{\nu_{\mu}}+\nu_{\mu} \\ \rightarrow p+\pi^{0} \rightarrow p+2\gamma \end{cases} \tag{3.2}$$

Hadronuclear Interaction
The accelerated protons can interact with the gas at the source or in clouds, producing many unstable hadrons. The decay will have a spectrum like the initial proton spectrum, resulting in a neutrino energy spectrum following that of the proton.

$$p+p \begin{cases} \rightarrow X+\pi^{\pm} \rightarrow X+\mu^{\pm}+\nu_{\mu}(\bar{\nu_{\mu}}) \rightarrow X+e^{\pm}+\nu_{e}(\bar{\nu_{e}})+\nu_{\mu}(\bar{\nu_{\mu}}) \\ \rightarrow X+\pi^{0} \rightarrow X+2\gamma \end{cases} \tag{3.3}$$

where X is any secondary heavier than a pion that can decay into pions. The approximate flavor ratio for photohadronic and hadronuclear interactions is $\approx \nu_e : \nu_\mu : \nu_\tau = 1:2:0$ at the source [72]. After neutrino oscillation, this ratio becomes $\approx \nu_e : \nu_\mu : \nu_\tau = 1:1:1$ when observed at Earth [29]. Assuming that 20% of pion's energy is transferred to the proton, the neutrino energy is approximately $E_\nu = 0.05E_p$ [70, 73]. The resulting neutrino spectrum will depend on the proton and photon spectra, and cooling processes will affect the fluence [29].

CSM-ejecta

The progenitor star can undergo significant mass loss during its lifetime, shedding part or even the entire envelope. Most stars are believed to experience mass loss before exploding [65], with more extreme mass loss observed in Type IIn SNe [65]. This pre-explosion mass loss forms what is known as the CSM. While the mechanisms behind this mass loss are not fully understood, several theories have been proposed. These include the star nearing its Eddington luminosity [74], as seen in SN 2005gl, where outbursts were observed years before the explosion, and high-luminosity pre-explosion neutrinos produced during nuclear reactions following carbon burning [74]. The mass loss rate varies by SN type, with common Type II-P supernovae exhibiting rates around $\sim 10^{-6} M_\odot$ yr^{-1}[64], and Type IIn supernovae showing rates of $\gtrsim 10^{-4} M_\odot$ yr^{-1} [64]. In rare extreme cases, such as SN 2006gy, mass loss rates as high as $1 M_\odot$ yr^{-1} have been observed [75]. Such high rates can explain phenomena like superluminous SNe with dense CSM [76] and may even indicate the emergence of new SN classes [77].

The presence of CSM and the corresponding mass loss rate can be inferred from EM light curves [63] and spectra, particularly when SN ejecta interact

with the CSM. This interaction can be detected through X-ray or radio emissions if the CSM is dense [61, 64] or through UV, optical, and NIR emissions [78]. Studying the CSM helps constrain the progenitor's mass [79]. The density of the CSM has been proposed as a factor influencing the timing of the EM shock breakout, with denser CSM causing delays from approximately 1 hour to several days after the explosion [80]. For simplicity, the CSM and ejecta are often assumed to be spherically symmetric [64]. However, this neglects hydrodynamic instabilities like Rayleigh-Taylor, which occur at the shock interface between surfaces of different densities. Efforts to model these instabilities in 2D [75] have shown that interactions of the ejecta with an aspherical CSM can lead to significant variations in the EM light curve. Additionally, the CSM and ejecta can be lumpy, as suggested by the hotspots observed in SN 1987A [64]. Despite many unknowns, the CSM-ejecta interactions are well-established through EM studies [61, 64, 63, 80].

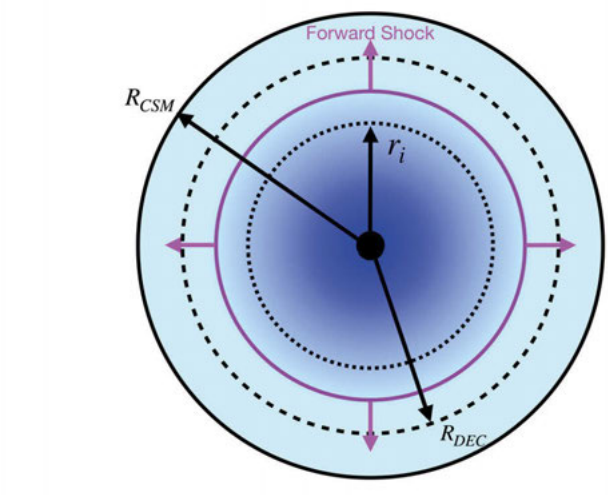

Figure 3.7. Schematic of the CSM-Ejecta interaction. The central compact object (BH or PNS, in black) is surrounded by the ejecta (blue), and the dense CSM is indicated in light blue, where the gradient in color describes the density, darker being the highest density. The dotted black line indicates the breakout radius r_i. The magenta line indicates the forward shock's propagation and the dashed black line indicates the deceleration radius of the ejecta, or R_{DEC}. Adapted from [81]

HE Neutrinos from CSM-Ejecta

When the supernova explodes, the shock propagates through the stellar envelope, traveling out with an ejecta mass M_{ej}, energy ε, and velocity v_{sh}. It then collides into the dense CSM with density ρ_{csm}, which is typically assumed to be near-stationary or stationary relative to the ejecta velocity [82, 81], forming shocks (Fig. 3.7). However, particle acceleration cannot occur until these

shocks cease to be radiation-dominated or until the shock reaches an optically thin region to Thomson scattering [83]. This region is often parametrized as when the optical depth of Thomson scattering reaches $\tau_T \sim \frac{c}{v_{sh}}$, where c is the speed of light, and this point determines the time t_i of the EM SBO, occurring at a radius $r_i \sim v_{sh} t_i$. In the case of a dense CSM, the SBO occurs at a much greater distance than the typical stellar radius [83, 81, 80], meaning acceleration will take place at a radius $r_{acc} \geq r_i$. At this point, the shocks become collisionless, allowing particle acceleration via mechanisms such as first-order Fermi acceleration.

Efficient magnetic field amplification is needed to accelerate CRs to sufficiently high energies via scatterings in the plasma or magnetohydrodynamics. Quasi-parallel shocks, as shown in [64], produce the most significant magnetic field amplification. However, this assumption may only hold for some cases, such as rotating progenitors [64]. Accelerated CRs lose energy through various processes, such as adiabatic losses, photohadronic, and hadronuclear inelastic scatterings. As long as the acceleration timescale is shorter than the combined cooling timescales, CRs can reach their maximum energy [66, 84, 85]. The HE neutrinos produced by CRs follow a spectrum similar to that of the parent $\frac{dN_{CR}}{dp} \propto p^{-s}$ [67, 84, 82], where p is the proton momentum, and N_{CR} is the CR number density. For quasi-parallel shocks, the proton index s is typically 2.0 [82]. Neutrinos produced in the interaction of CSM-ejecta are expected to arrive at Earth with a delay relative to the core bounce, as seen in Fig. 3.8a, where they are expected to arrive at Earth anywhere from 0.1 day to 1 year after, with energies spanning from hundreds of MeV to TeV (see Fig. 3.8b). Type IIn and II-P SNe, which have the largest mass loss and denser CSM, are predicted to produce the highest fluences [84, 82, 86, 87].

Modeling the CSM-ejecta interaction and resulting neutrino fluxes involves a significant parameter space with considerable uncertainties. For example, increasing the proton spectral index s typically reduces neutrino production [84]. The density of the CSM also plays a crucial role; higher densities lead to increased neutrino fluxes [86, 88]. Other important factors include the mass loss rate, shock velocity, wind velocity, and CSM profile [87], as well as the homogeneity of the CSM [67]. These variables highlight the complexity and uncertainty in modeling neutrino production in supernovae.

Choked jets

Another mechanism for producing HE neutrinos in SNe involves the presence of jets. During the collapse, massive jets can form and travel through the stellar envelope, often accompanied by a significant GRB [89]. Unlike CSM interactions, which are common in many CCSNe, identifying progenitors with jets is more challenging due to observational difficulties. For jets to

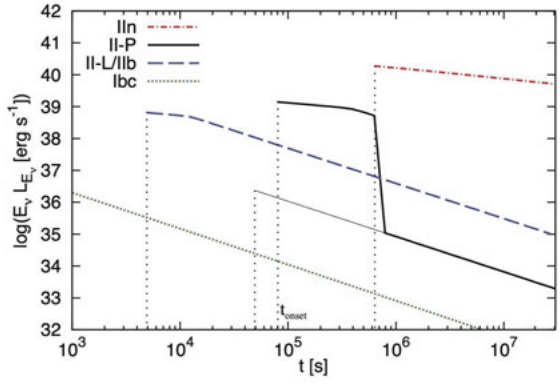

(a)

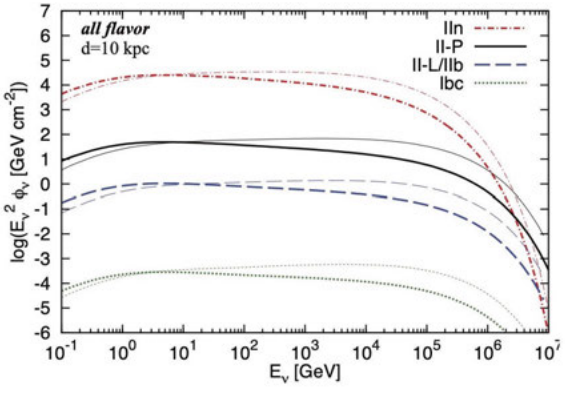

(b)

Figure 3.8. Neutrino predictions for a CSM-ejecta model. (a) Shows the neutrino lightcurves for different SN types. (b) Neutrino fluences for different types of SN, assumed to be at a distance of $d = 10$ kpc, and integrated over different t_{max}, which is the maximum integration time (see [84] for details). Thin curves represent s = 2.0 and thick curves s = 2.2. Reproduced from [84].

form, a central engine such as a BH is necessary [90]. The formation of jets involves the infall of matter into a rapidly rotating core, which then gets ejected through axisymmetric, collimated channels. Progenitors capable of forming such jets are typically massive stars with masses $\gtrsim 25-28M_{\odot}$ [91, 90]. These jet-producing SNe are often associated with Type Ib/Ic [92] and potentially Type IIb [93]. Observational evidence includes SN 2007gr, a Type Ic SN with mildly relativistic radio jets [94], and a Long Gamma-ray burst (LGRB) with emission duration of $\gtrsim 2-10^3$ s [90], such as GRB 171205A associated with SN 2017iuk, a Type Icn SN that exhibited jet signatures [95].

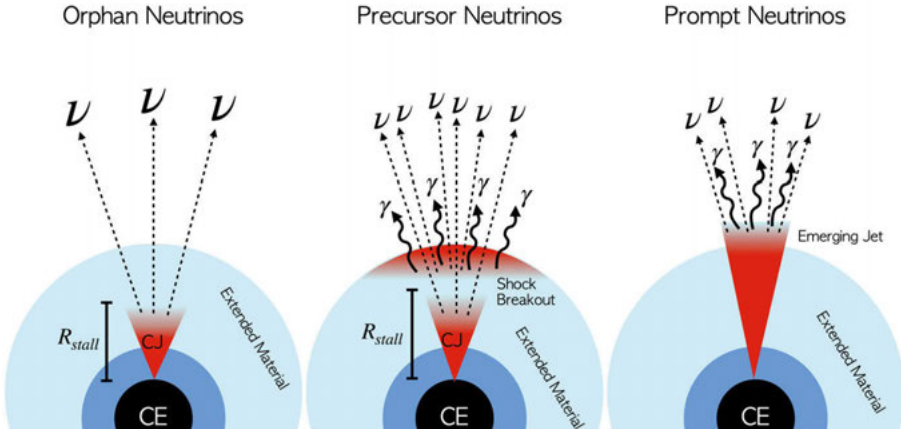

Figure 3.9. The different models of neutrino production in SNe with jets, where CJ stands for choked-jet, R_{stall} is the jet's stalling radius, and CE is the central engine. Left image) Choked-jet model where only orphan neutrinos would be observed. Middle image) Model for low-luminosity GRBs, where the EM emission breaks out of the cocoon, and precursor neutrinos would appear before the EM emission. Right image) Standard GRB, where both the neutrinos and the gamma rays are emitted. Adapted from [89].

We can broadly classify the jets into three categories: GRBs with relativistic jets, which have a Lorentz bulk factor of $\Gamma_b \gtrsim 100$ [90], low luminosity GRBs with mildly-relativistic jets, with $\Gamma_b < 100$ [89] and Choked-Jet (CJ) with $\Gamma_b \approx 3-10$ [96, 97, 98]. For GRBs, since the jet is highly relativistic, they can traverse the stellar envelope, eventually breaking out in a dramatic gamma-ray display and potentially producing HE neutrinos [89] (Fig. 3.9 right model or prompt neutrino model). However, such bright events are rare to observe from Earth because the jet must be pointed directly at us. The occurrence is tied to the jet's beaming angle $\theta_j \sim 1/\Gamma_b$, which means that the probability of the jet pointing towards Earth scales as $\frac{1}{2\Gamma_b^2}$ [97, 90, 99]. For instance, for a jet with $\Gamma_b = 100$, the chance of it pointing at Earth is $\frac{1}{20000}$, making these events relatively infrequent. Alternative scenarios include less collimated jets, such as low-luminosity GRBs. These jets, with a smaller Γ_b, may interact with the stellar envelope without entirely escaping, leading to observable EM emission and some neutrinos [89] (see Fig. 3.9 middle figure). The third model, and the focus here, is the CJ (Fig. 3.9 left or orphan neutrino model), where jets with $\Gamma_b \approx 3-10$ [96, 97, 98] do not break out of the stellar envelope [90, 97, 100, 101]. These types of jets do not produce visible EM signals, except potentially for a faint radio afterglow [97]. However, HE neutrinos produced in the shocks can escape. Since CJ is less collimated, they are more

likely to be pointing at Earth, with estimated probabilities ranging from $\frac{1}{18}$ to $\frac{1}{200}$. As a moderate estimate, this type of jet is thought to occur in 10% of Type Ib/Ic and IIb SNe [97], and potentially up to 4% of all CCSNe [96, 102].

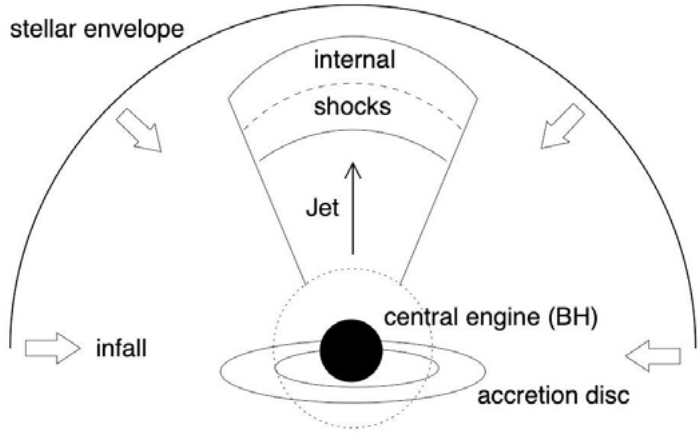

Figure 3.10. Schematic of a choked jet in a collapsing supernova, where the jet fails to burrow through the envelope. We can see how the jet would form from the BH infall. Reproduced from [90].

There are several proposed explanations for how the jets would get choked: a dense CSM, which would obstruct the jet's progress, preventing it from escaping the stellar envelope [103, 89], a short central engine time, where if it has a short-lived activity period, it may not provide with enough time for the jet to break free [104], a too slow jet [90], or a combination of these factors [104]. In all cases, the result is that the jet becomes choked within the envelope, leading to the formation of internal shocks within the jet and at the interface between the jet and the surrounding stellar material (see Fig. 3.10). Through particle acceleration, HE neutrinos with energies reaching the PeV range are produced (Fig. 3.11). These neutrinos are primarily generated through the decay of pions and kaons [90, 96], or in some models, through the decay of charm mesons [101, 100]. The emission timescales of these neutrinos are typically short-lived, lasting on the order of 10-100 seconds [90, 96, 101, 98, 105].

After having established the neutrino production for stellar death, covering both low- and high-energy neutrino production, and knowing that SNe can leave behind BH and PNS, we can transition to what happens next in the system's evolution.

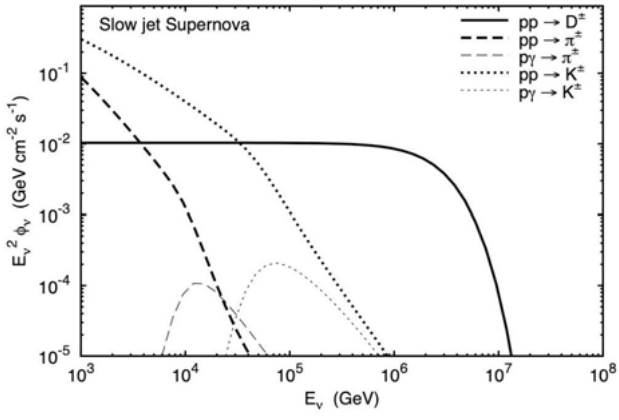

Figure 3.11. The expected neutrino flux for the choked-jet model, for the different interaction channels, at a distance d = 20 Mpc. Reproduced from [101].

3.2 Neutron Star Mergers

A NS is the end-product of intermediate-mass stars once they undergo core collapse. It primarily consists of neutrons, and its degeneracy pressure supports the star [106, 107]. They come in a limited mass range, from $0.5 - 5M_{\odot}$ [106], small radii of 10-12 km [107], and have extreme densities of $\rho > 10^{14} g/cm^3$ [107] and extreme magnetic fields of 10^{13}G [108]. Their existence was first confirmed on November 28, 1967, when Bell and Hewish observed a rapidly varying radio source, CP 1919+21 [106], or a pulsar. NS are also in beta equilibrium, meaning the electron capture and beta decay rates are balanced, keeping the star's composition stable [107, 109].

After a SN, a newly formed PNS is extremely hot, with temperatures around 50 MeV or 10^{11} K [108, 110]. It cools rapidly via neutrino emission and stabilizes, reducing to a core temperature of about $10^9 - 10^{10}$ K (0.5-1 MeV) and a warmer crust [108, 109, 111]. Over 10-100 years, heat from the crust is transported inward, and the NS becomes isothermal [108], with a surface temperature $10^5 - 10^6$ K [108]. Throughout its lifetime, the star emits X-ray photons [108]. Neutrinos are thought to play a key role in cooling the NS, as its matter is optically thick to photons, meaning that only the surface cools via EM emission [108]. Theoretical models are used to understand matter at these extreme densities, as direct measurements are not feasible, and we can only approximate the behavior of matter at this state via extrapolation of laboratory data [109]. While NS serve as valuable astrophysical laboratories for studying such high-density matter, this thesis focuses on the signatures of the NS mergers rather than the NS themselves since the neutrino flux from the cooling is too low and over too long timescales to be observable.

3.2.1 Mergers

NS mergers occur in a binary system with either another NS or a BH. Over time, gravitational waves cause the system's orbit to decay, leading to a Compact Binary Coalescence (CBC). This event is expected to produce a variety of signals, including neutrinos, within a very short timescale (milliseconds to seconds) [112, 113]. Simulating such systems is highly complex, making it difficult to predict precisely how and when these signals will appear. However, GW and EM emissions have been observed from mergers. For instance, GW 170817 was the first observed Binary Neutron Star (BNS) merger detected by LIGO [114], and Fermi-GBM also saw it as a Short Gamma-ray burst (sGRB) of 2 seconds, GRB 170817 [24]. An optical counterpart was identified within the GW error region, confirming the presence of a kilonova [115]. Neutrinos from mergers, however, have not yet been observed, which means that their production and timing remain uncertain. However, research continues, and one of the starting points is the similarity to CCSNe, suggesting that, like CCSNe, mergers should release a substantial amount of gravitational binding energy, O(10^{52}-10^{53} erg), in the form of thermal neutrinos [112]. To better understand the production of low-energy neutrinos during a NS merger, we need to examine what happens during a coalescence, where the violent event heats high-density matter [116], allowing for the production of a burst of neutrinos [117, 112] that would be coincident with a GW signal [117, 118, 119].

Merger Dynamics

Merger dynamics in BNS and Neutron Star - Black Hole (NSBH) systems are driven by the interplay between pressure, gravity, and centrifugal forces, leading to different outcomes depending on which force dominates. If gravity is the strongest, in the case of a BNS, the merger will collapse into a BH [113]; however, if pressure and centrifugal forces can counteract gravity, the merger core bounces back, forming a rapidly rotating Hyper Massive Neutron Star (HMNS) [113]. The HMNS can be short-lived (less than 5 ms) or long-lived (more than 5 ms) [113], depending on the equation of state and the total mass of the binary system. It survives temporarily due to shock-induced thermal pressure [117] but eventually collapses into a BH after losing angular momentum via GWs [113, 117] and potentially neutrinos [117]. Both scenarios lead to the formation of an accretion disk (torus) around the compact object (see Fig. 3.12).

Several sites can produce a burst of thermal neutrinos in these mergers with timescales of milliseconds to seconds: at the contact interface in the merger, where matter can be released in polar jets or isotropic outflows [118]; from matter ejected post-merger either via viscous heating (see Fig. 3.12) or neutrino driven winds; from the hot part of the accretion disk [119, 120]; and during the cooling phase of the merger remnant or HMNS prior to collapse [117, 119].

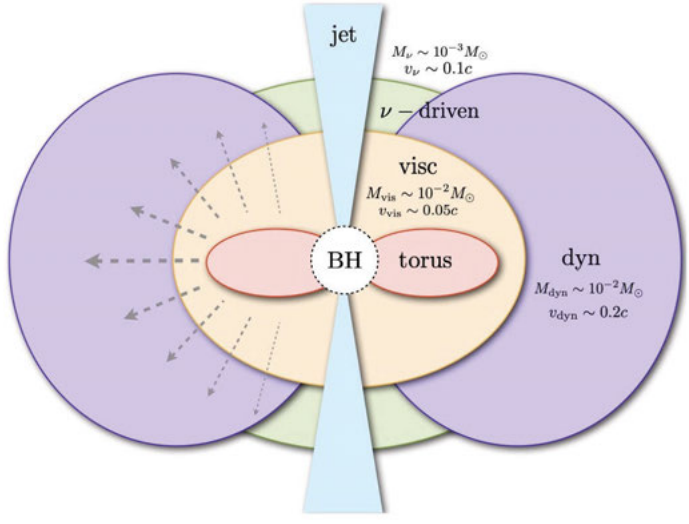

Figure 3.12. Schematic of a merger with a BH that has a torus and jets. Going from the earliest to the latest outflow in time: The dynamical ejecta (violet) is the earliest outflow expected, with the neutrino-driven (green) next and finally the viscous ejecta (orange). Typical values for the outflows are given in the image, where M is the total mass for each respective outflow, and v is the velocity of each outflow. Reproduced from [120].

3.2.2 Low-Energy Neutrinos from Mergers

As we have seen, several sites can produce thermal neutrinos in mergers. However, most simulations do not extend beyond a few milliseconds in their time evolution [119] and rarely simulate all the regions. It is theorized that the compression of dense, neutron-rich matter raises the temperature to levels where URCA processes can occur [119] (see Table 3.1). In all potential sites of thermal neutrino production, the neutron-rich environment favors positron capture on free neutrons over electron capture, making $\bar{\nu}_e$ the dominant emission [112, 121], particularly in the shocked regions of the accretion disk [121]. Electron neutrinos are expected to be less dominant and likely emitted from the polar regions [121], while heavy lepton neutrinos would contribute only about 10% of the total neutrino luminosity [112]. These thermal neutrinos are also believed to play a crucial role in launching jets during mergers through energy deposition at the poles via $\nu - \bar{\nu}$ annihilation [113, 122], and potentially produce a GRB. These estimates depend on each site's density and electron fraction. Neutrino luminosities are expected to range from 10^{52}-10^{53} erg/s [112, 120], with larger masses yielding higher luminosities [112]. Depending on whether the neutrinos are produced quasi-isotropically or at the poles, the observable luminosity could vary by a factor up to 20 [112] (see Fig. 3.13). Our understanding of these objects remains limited, even with the advance-

ments in GW detectors like LIGO-Virgo-KAGRA (LVK). To fully comprehend the dynamics of mergers and the behavior of matter at supra-nuclear densities [123], it is vital to study these events using as many messengers as possible, including neutrinos.

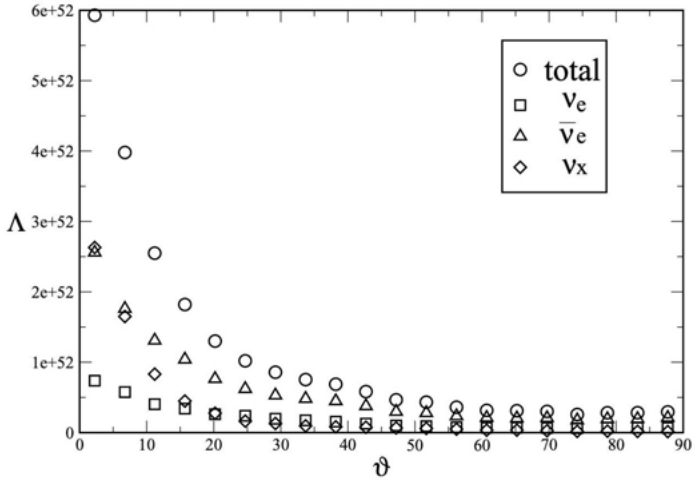

Figure 3.13. The neutrino luminosity as a function of solid angle for different flavors. The y-axis shows the neutrino luminosity as a function of the solid angle ϑ in units of erg/s, and the x-axis shows the solid angle in degrees, where 0 represents 'pole-on' and 90 represents the 'edge-on' view. Reproduced from [112].

3.3 Gamma-Ray Bursts

NS mergers are known to produce GRBs, as evidenced by the sGRB observed immediately following the GW 170817 event [124]. The prevailing theories suggest that GRBs originate from either a merger involving NS (kilonovae) or from collapsars, where massive stars collapse into black holes. Kilonovae are believed to cause sGRB (lasting less than 2 seconds) [125] and collapsars are thought to be responsible for LGRB (lasting more than 2 seconds) [126]. Both scenarios are theorized to involve massive accretion disks and possibly jets of matter, which release enormous amounts of energy in the form of gamma-rays (ranging from $10^{50} - 10^{52}$ erg [127]). This implies a significant energy budget and an efficient mechanism for energy release, where neutrinos could be produced [127].

3.3.1 GRB Lightcurve

When matter falls into a central compact object, conservation of angular momentum causes the formation of an accretion disk around the object [127]. These disks are found in various astrophysical systems, including GRBs. While many models exist to describe them, in systems with low accretion rates, the disk is primarily composed of plasma and are dominated by photon radiation. However, in systems where a large amount of mass is accreted, such as in GRBs, a hypermassive accretion disk can form, in which free baryons become the dominant component, potentially leading to the production of thermal neutrinos [127]. The general anatomy of a gamma ray light curve for a GRB is as follows (see Fig. 3.14):

- **Precursor:** Pre-peak emission, occurring seconds to hundreds of seconds before the main emission [128]. It is estimated that 10% of sGRB and 20% of LGRB have this emission [129].
- **Quiescent period/s:** Little to no emission is observed [129].
- **Prompt:** main emission episode, which is identified as the episode where the highest peak in flux is observed (denoted as *Peak Flux R* in Fig. 3.14). This episode contains about 90 to 100% of the total flux, depending on whether there is a precursor or a post-peak emission.
- **Post-peak:** Finally, some GRBs (about 20% [129]) may have a post-peak emission, which could be tied to afterglows [129].

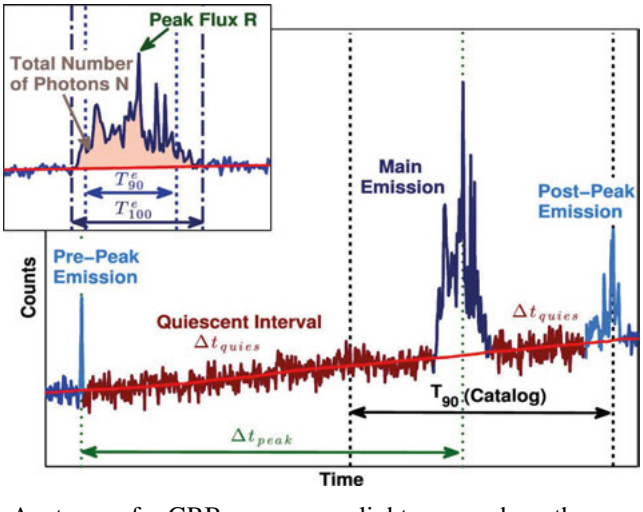

Figure 3.14. Anatomy of a GRB gamma-ray lightcurve, where the y-axis represents the counts and the x-axis represents the time. Reproduced from [129]

3.3.2 Low-Energy Neutrinos from GRBs

It is unknown what powers the central engine of these events. However, neutrinos play a crucial role in many models attempting to explain these events, particularly in the precursor and prompt phases (see Section 3.1.3 and Fig. 3.9). These models often involve components such as accretion disks, jets, and fireball mechanisms to account for the observed phenomena [127, 128].

Neutrino Dominated Accretion Flows

In the hyperaccretion disks of GRBs, the extreme densities and temperatures ($\rho = 10^{10} - 10^{13}\, g/cm^3$ and $T = 10^{10} - 10^{11}$K) lead to conditions where photons become trapped, preventing them from escaping the disk [127]. In this environment, a significant amount of thermal neutrinos is produced, primarily through URCA processes, along with other neutrino reactions (see Table 3.1). These neutrinos are emitted from the disk's surface [128, 130, 131], carrying away energy generated by viscous dissipation–the conversion of gravitational potential energy into thermal energy within the disk [127, 130]. The dominant neutrino flavors emitted are ν_e and $\bar{\nu}_e$ [127, 131], with a slight preference for $\bar{\nu}_e$ due to higher density of neutrons compared to free protons in the disk [131]. These thermal neutrinos then annihilate, producing electron-positron pairs, which are thought to drive the outflows that power the GRB [127, 131]. These disks are called Neutrino Dominated Accretion Flow (NDAF) [127, 128, 130].

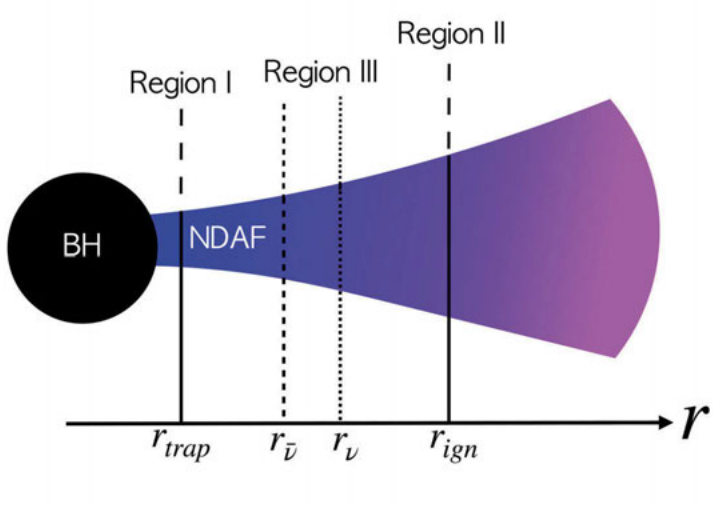

Figure 3.15. Schematic of a NDAF, showing the different regions. The horizontal axis represents the radii for the different regions, and the color scheme represents the composition of the disk, from free baryons (blue) to plasma (magenta). Adapted from [127]

There are three different regions in the NDAF, each characterized by different physical conditions and cooling mechanisms (see Fig. 3.15). The in-

nermost region (Region I) lies at a radius where neutrinos become trapped (r_{trap}), a condition dependent on the accretion rate; the middle region (Region III) is defined by the radii where the disk is opaque to neutrinos ($r_{\bar{\nu}}$, r_{ν}), meaning that neutrinos cannot escape easily. Finally, the outermost region (Region II) is where neutrino cooling dominates, extending to the ignition radius r_{ign}–beyond which other cooling mechanisms, such as photon emission, become significant [127]. In general, the rate of neutrino cooling decreases with increasing radius due to the drop in temperature and density as you move further from the central compact object [131]. The neutrino emission from NDAF is quasi-isotropic, with only mild angle dependency, meaning these neutrinos should be detectable event if the GRB's beam is not pointed directly at Earth [131].

Fireball

In the fireball model, the thermal neutrinos produced in the accretion disk can annihilate above the disk, generating electron-positron pair plasma or a hot fireball that expands relativistically [132, 133]. This fireball then undergoes recombination into photons through the process $e^+ + e^- \rightarrow \gamma + \gamma$. However, due to the fireball's opacity to photons [132, 134], these photons cannot escape. Instead, other processes that produce thermal neutrinos can take place, including electron-positron annihilation ($e- + e^+ \rightarrow \nu + \bar{\nu}$), neutrino pair photoproduction with electrons ($\gamma + e^{+/-} \rightarrow e^{+/-} + \nu + \bar{\nu}$), photon decay ($\gamma \rightarrow \nu + \bar{\nu}$) and two-photon annihilation ($\gamma + \gamma \rightarrow \nu + \bar{\nu}$) [135]. Since the fireball is not opaque to neutrinos, these could promptly escape [132, 134] in a massive burst (millisecond to second) of neutrinos, with fluency at Earth for this model being:

$$\Phi_{\nu} = 1 \times \left(\frac{E_{\nu_{tot}}}{2 \times 10^{53}\,\mathrm{erg}} \right) \left(\frac{65\,\mathrm{MeV}}{E_{\nu}} \right) \left(\frac{4000\,\mathrm{Mpc}}{d} \right)^2 \mathrm{cm}^{-2}, \tag{3.4}$$

where E_{ν} is the neutrino energy, d is the distance to source, and $E_{\nu_{tot}}$ is the total bolometric energy released [132].

BZ Jets

Jets in GRBs are believed to be produced by either a rotating BH or an accretion disk surrounding the BH [128]. These jets, often referred to as Blandford-Znajek jets (BZ) [136], are driven by the rotational energy of a spinning BH in the presence of a magnetic field, along with an NDAF [137]. The jets can go through different phases, such as precursor, shocked, and unshocked jet stages [128]. This variation in jet behavior could explain the different emissions observed in gamma rays and why some GRBs display a precursor phase followed by a prompt phase, with a quiescent period in between (see Figs. 3.9, 3.14 and 3.16). Theories suggest that these jets are formed from the thermal neutrinos produced in the fireball and NDAF [128, 130, 133]. For example,

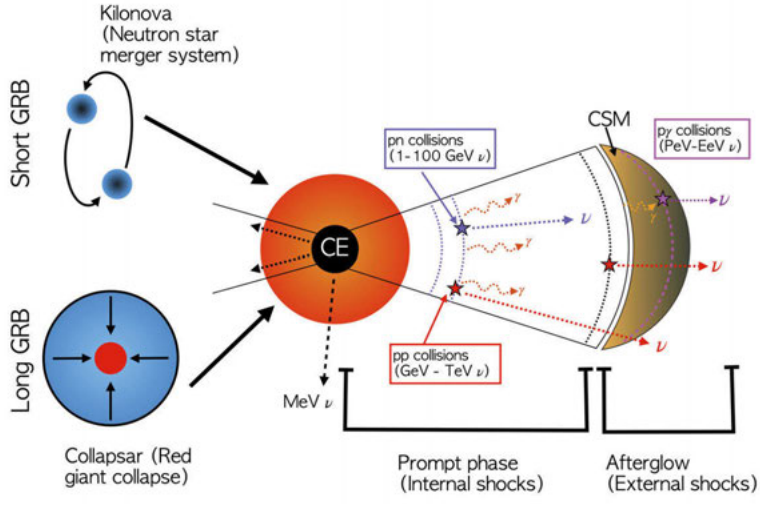

Figure 3.16. Anatomy of a GRB, showing the different progenitors and regions of neutrino and photon emission.

the precursor phase of the jet is formed during a CCSN [128]. Here, the initial shockwave moves outward but lacks the energy to eject all the stellar material, resulting in a precursor that lasts a few seconds [128]. After this phase, a fall-back accretion disk forms during the quiescent stage, leading to the collapse of a PNS into a BH. This process generates an NDAF, which feeds a jet through $\nu + \bar{\nu}$ annihilation [128, 130]. Although these jets do not directly contribute to the production of thermal neutrinos, they are still part of the dynamical system, and understanding when and how they could form can facilitate the search for thermal neutrinos.

The common factor between the NDAF and fireball mechanisms is their reliance on high-density ($\rho = 10^{12} - 10^{14} g/cm^3$) and high-temperature ($T = 10^9 - 10^{11}$ K) conditions. These conditions allow frequent nucleon-nucleon interactions and provide sufficient thermal energy to overcome nucleon-binding energies. While precise mechanisms powering GRBs remain uncertain, studies suggest that neutrino annihilation, particularly in NDAFs, could explain many sGRBs and LGRBs [127], either with or without BZ jets. For more extreme scenarios, such as Ultra-LGRBs, which may last tens of thousands of seconds, magnetars–NS with powerful magnetic field–combined with BZ jets are considered a plausible explanation [127].

The effects of the viewing angle have been examined, showing that gamma-ray emission regions and timelines might appear different due to factors like accretion disk precession around the BH [127]. In contrast, the impact of viewing angle and BH spin on MeV neutrino luminosity is minimal [131]. Thermal neutrino luminosities from GRBs can vary significantly: they may

be up to four orders of magnitude lower than those from CCSNe [131] or, in more exotic scenarios such as magnetized NDAFs or extreme accretion rates, could reach energy releases of 10^{54}erg[138, 127]. The duration of neutrino emissions also varies widely, from milliseconds to seconds for fireballs [132] and under 2 seconds for mergers [131], and hundreds of seconds for collapsars [131]. In the case of collapsars, NDAF neutrino emissions might overlap with the PNS neutrino emissions if the PNS survives for a period before collapsing [131, 139].

4. How to Observe Neutrinos from Transients

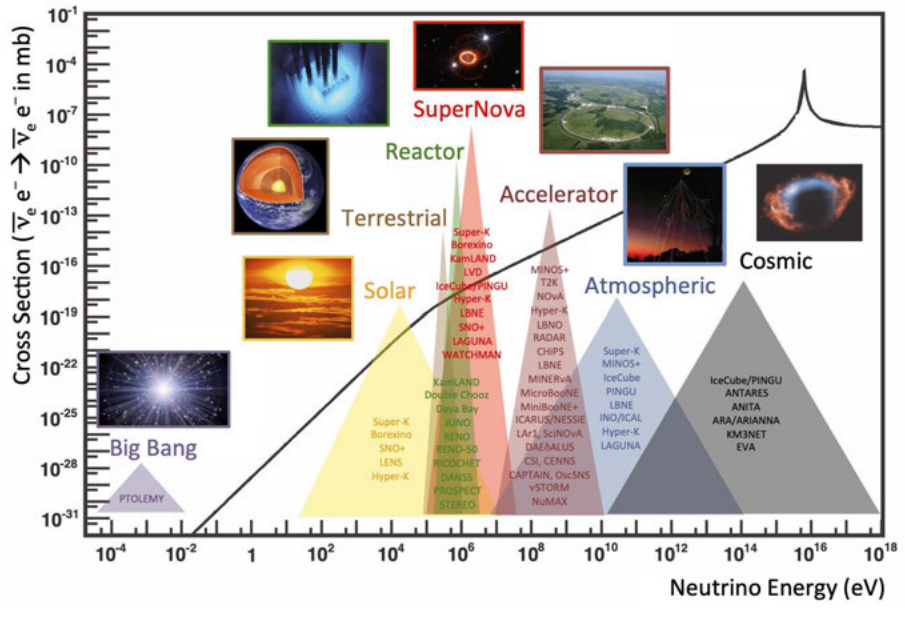

Figure 4.1. Neutrino interaction cross section in millibarn (mb) for a scattering process $\bar{\nu}_e e^- \rightarrow \bar{\nu}_e e^-$ as a function of neutrino energy. We can see the different experiments and which energy regimes they can access, highlighting different sources at different energies. Reproduced from [140].

Neutrinos rarely interact with matter, making them a challenge to observe. The neutrino cross-section, which tells us how likely it is to interact, increases with neutrino energy but remains small. For instance, at an energy of 1 GeV, the cross-section is on the order of 10^{38}cm^2/GeV. The work presented in this thesis focuses on neutrinos from transients that can produce a burst of MeV neutrinos as well as HE neutrinos (O(>GeV)). Therefore, we will cover the main interactions by which we can observe neutrinos in these energy regimes and the relevant detection technologies. Specifically, Cherenkov light detectors will be highlighted, as they can detect low-energy and HE neutrinos from transients, as shown in Fig. 4.1.

Threshold-less processes		
Coherent scattering	$\nu + A \rightarrow \nu + A^*$	NC
Low-energy processes ($\sim 0.1 - 100$ MeV)		
Inverse beta decay	$\bar{\nu}_e + p \rightarrow e^+ + n$	CC
ES with electrons	$(\bar{\nu}, \nu) + e^- \rightarrow (\bar{\nu}, \nu) + e^-$	NC
ES with electrons	$(\bar{\nu}_e, \nu_e) + e^- \rightarrow (\bar{\nu}_e, \nu_e) + e^-$	CC
ν-nucleus interactions	$\nu_e + (N,Z) \rightarrow e^- + (N-1, Z+1)$	CC
ν-nucleus interactions	$\bar{\nu}_e + (N,Z) \rightarrow e^+ + (N+1, Z-1)$	CC
Intermediate energy processes ($\sim 0.1 - 20$ GeV)		
QE with nucleon	$(\bar{\nu}, \nu) + \mathscr{N} \rightarrow \mathscr{N} + l^{\pm}$	CC
ES with nucleon	$(\bar{\nu}, \nu) + \mathscr{N} \rightarrow (\bar{\nu}, \nu) + \mathscr{N}$	NC
Deep inelastic scattering (≥ 20 GeV)		
Charged current DIS	$(\bar{\nu}, \nu) + \mathscr{N} \rightarrow l^{\pm} + X$	CC
Neutral current DIS	$(\bar{\nu}, \nu) + \mathscr{N} \rightarrow (\bar{\nu}, \nu) + X$	NC

Table 4.1. *Important neutrino interactions for observing neutrinos from astrophysical transients [141, 142]. ES stands for elastic scattering, and QE for quasi-elastic scattering. ν denotes neutrinos of any flavor, A denotes the nucleus, N denotes the neutron number in the nucleus, Z denotes the proton number in the nucleus, $\mathscr{N}$ is the nucleon and can be protons or neutrons, X = any final set of hadrons, and l is a lepton of the same flavor as the neutrino.*

Neutrino Interactions with Matter

To observe neutrinos, we can either use atomic electrons or nucleons as targets. Depending on the kinematic energy threshold, different channels will dominate over the others. The energy thresholds at which certain interactions dominate can be roughly separated into four [141]: Threshold-less processes, low-energy for 0.1-100 MeV, intermediate energy for 0.1-20 GeV, and high energy for over 20 GeV to TeV and up, as we can see in Table 4.1.

Interactions Relevant for MeV Regime

This subsection will cover the relevant interactions by which thermal neutrinos from astrophysical transients (see Table 4.1), with mean energies between 10-30 MeV, can be observed. Since CC interactions require energy to produce the partner lepton, in the case of thermal neutrinos, only electron flavors have sufficient energy to produce a partner lepton. For example, for an inverse beta decay process, ν_μ and ν_τ would require a minimum energy of about 116 MeV and 3.4 GeV respectively [1] to produce a muon or a tau lepton.

[1] The kinematic threshold energy for this interaction was obtained by using the formula $E_{min,\nu_l} \geq \frac{(m_p + m_l^+)^2 - m_p^2}{2m_p}$ [142], where m_p is the proton mass, m_l^+ is the lepton mass, and assuming that c=1.

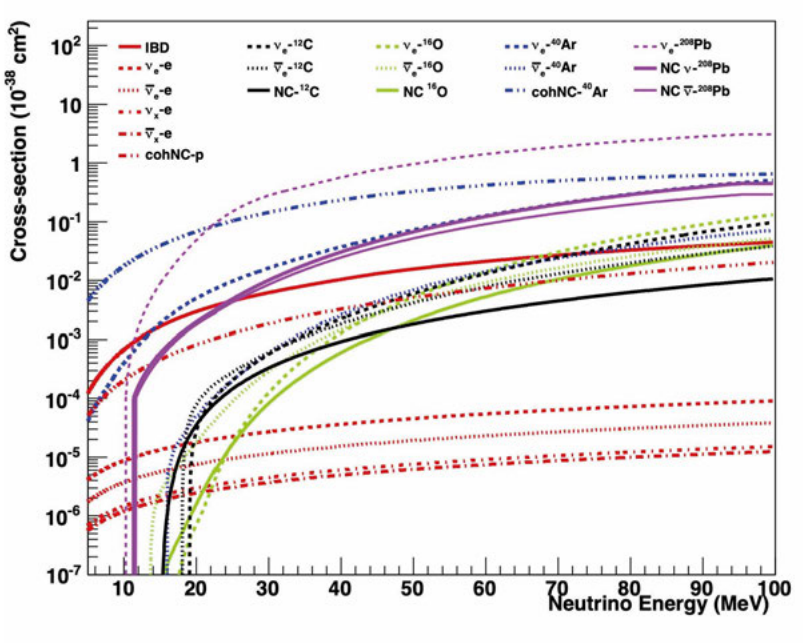

Figure 4.2. Relevant neutrino cross section for low energy electron (anti) neutrinos for different targets. Reproduced from [142].

Coherent Scattering

This is a threshold-less process, where a neutrino of any flavor scatters off a nucleus through NC, where the observable is the recoil energy or energy loss. Although the interaction rate is quite large, with a cross-section that can reach O(10^{-38}cm^2) in the MeV regime, which is several orders of magnitude larger than other interactions at this energies, the recoil energy is too low, in the O(few keV), making it a difficult channel to probe neutrino interactions since it requires a very low background to observe the recoil.

Inverse Beta Decay

Inverse Beta Decay (IBD) has a kinematic threshold of $\sim$ 1.8 MeV for $\bar{\nu}_e$, lower than the expected mean energy from thermal neutrinos. The observable are the secondaries: positrons and neutrons. For large-scale Cherenkov light or scintillation detectors, since the targets are protons, the only observable is the loss of positron energy. In some detection techniques, the neutron can be captured by an isotope, which, when it decays, causes further energy loss in the form of photons, which can be observed.

Elastic Scattering with Electrons

All thermal neutrino flavors can scatter with electrons through NC, and for CC interactions, electron-flavored neutrinos [2]. The elastic scattering is an important interaction for thermal neutrinos since the outgoing electron will retain the directionality of the neutrino, allowing for a good pointing, unlike inverse beta decay secondaries, which have no anisotropy.

Neutrino - Nucleus Interactions

Finally, for thermal neutrinos, we have the neutrino-nucleus interactions, where ν_e and $\bar{\nu}_e$ interact via CC with a nucleus, for example ^{16}O, producing an electron or a positron, and all the other flavor neutrinos can interact via NC, with a final state being an ejected neutron or an excited nucleus that can emit γ's when de-exciting, both which can be observable depending on the experimental technique.

Interactions Relevant for >GeV Regime

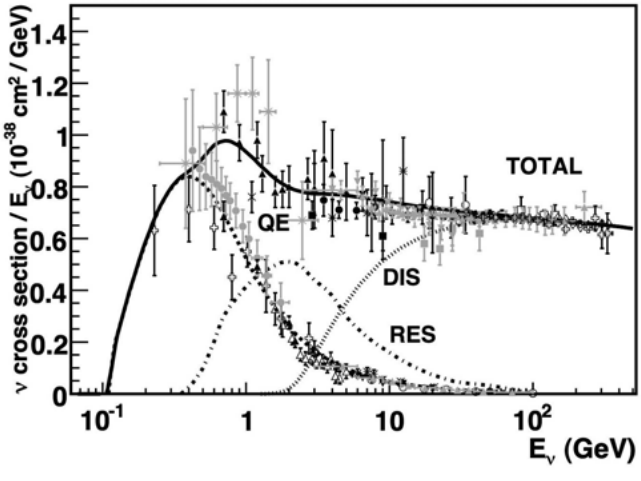

Figure 4.3. Neutrino cross-section for different interaction channels up to $\sim$ 100 GeV. In solid, we can see the total contributions, in dashed the quasi-elastic scattering (QE), in dot-dash the resonant production (RES) and finally in dotted the deep inelastic scattering (DIS). Reproduced from [141].

[2] Although it is important to note that $\bar{\nu}_e$ is helicity suppressed by a factor of 3 compared to ν_e [141].

Elastic Scattering with Nucleon

In the intermediate energy range, we have the CC process of elastic scattering with nucleon called quasi-elastic scattering and the NC process called elastic scattering (see Fig. 4.3). There is also the inelastic scattering with a nucleon called the resonant production, where when a neutrino interacts with a nucleon, a baryon resonance is produced and quickly decays into a pion and a nucleon. However, these interactions are sub-dominant for the high-energy searches relevant to this work. They will not be covered further, except for the Glashow resonance at very high energies.

Deep Inelastic Scattering

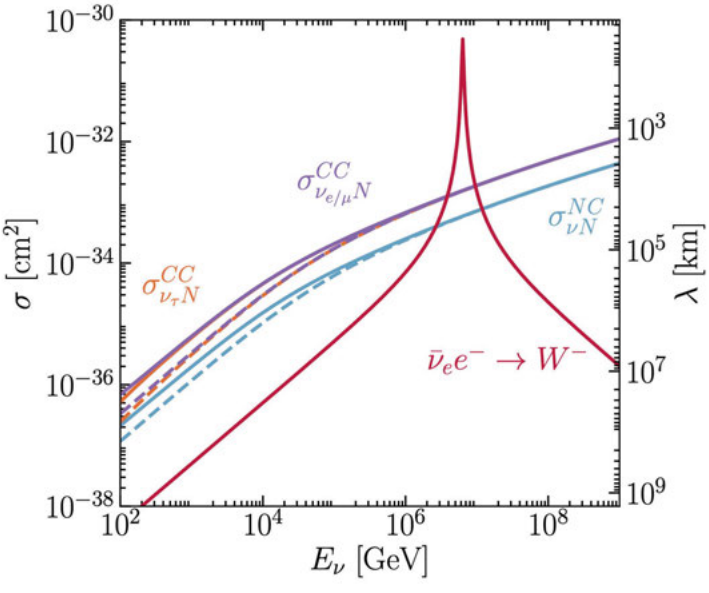

Figure 4.4. High-energy neutrino cross sections, showing the Glashow resonance. The left y-axis represents the cross-section σ, the right y-axis λ the mean free path in water for these reactions, and the x-axis the neutrino energy E_ν. The red curve is for the Glashow Resonance process, and all the other curves are for DIS, where the solid is for the neutrinos and dashed for antineutrinos. Reproduced from [143].

Deep Inelastic Scattering (DIS) is the last interaction channel we will cover, and the crucial interaction channel for HE neutrinos, typically with energies starting around 20 GeV and becoming dominant at 100 geV and above (see Fig. 4.3 and Table 4.1). Unlike interactions at lower energies, which involve the whole atomic structure or composites, DIS occurs at the parton level for HE neutrinos. The cross-sections for CC and NC DIS interactions are similar, but CC interactions are slightly more dominant [141], as we can see in Fig. 4.4. The following equations can approximate the cross-sections:

$$\sigma_{\nu N}^{CC} = (\frac{E_\nu}{1\,GeV})^\alpha \times 5.35 \times 10^{-36}\,cm^2 \tag{4.1}$$

$$\sigma_{\nu N}^{NC} = (\frac{E_\nu}{1\,GeV})^\alpha \times 2.31 \times 10^{-36}\,cm^2, \tag{4.2}$$

where σ represents the cross-section, E_ν is the neutrino energy and $\alpha = 0.363$. In CC interactions, the observable outcomes include both the hadronic shower and the partner lepton. In contrast, for NC interaction, all the event information is contained in the hadronic shower. The inelastic neutrino-electron scattering at high energies is suppressed due to the small target mass, except at very high energies O(PeV). In this instance, when $\bar{\nu}_e$ reaches 6.3 PeV, a Glashow Resonance reaction can occur (see Fig. 4.4):

$$\bar{\nu}_e + e^- \rightarrow W^- \rightarrow X, \tag{4.3}$$

producing a W^- boson, which then decays into various secondary particles, generating the observables. IceCube recently observed this resonance [144].

How are neutrinos observed

As we established earlier, many final state observables exist from different interaction processes. Here, we will cover how these final states can be observed with different detection methods for the different energy regimes.

Cherenkov Light Detectors

As a charged particle moves through a medium at a speed greater than the phase velocity of light in that medium, it excites the medium's atoms. As these atoms return to their ground state, they emit photons. Because the particle moves faster than the phase velocity v_{light} of light in the medium, the emitted photons are coherent and form a cone of light known as Cherenkov radiation. The angle of this cone, which is the angle between the charged particle's direction and the radiation, θ_c, is given by:

$$cos(\theta_c) = \frac{v_{light}}{v}, \tag{4.4}$$

where v is the velocity of the charged particle, and $v_{light} = \frac{c}{n}$ is the phase velocity of light in the medium, with c being the speed of light in a vacuum and n is the refractive index of the medium. This phenomenon is known as Cherenkov radiation, and it is used in various types of particle detectors to identify HE particles. The number of emitted Cherenkov photons can be obtained with the Frank-Tamm equation [145] and is dependent on the particle energy E and the charged particle path length x (Fig. 4.5):

$$\frac{dN_\gamma^2}{dE\,dx} = \frac{2\pi\alpha z^2}{hc}\sin^2(\theta_c) \approx 370\,z^2\sin^2(\theta_c)\,\mathrm{eV}^{-1}\,\mathrm{cm}^{-1} \tag{4.5}$$

where $\alpha \approx \frac{1}{137}$ is the fine structure constant, z is the charge number of the emitting particles, and h is Planck's constant.

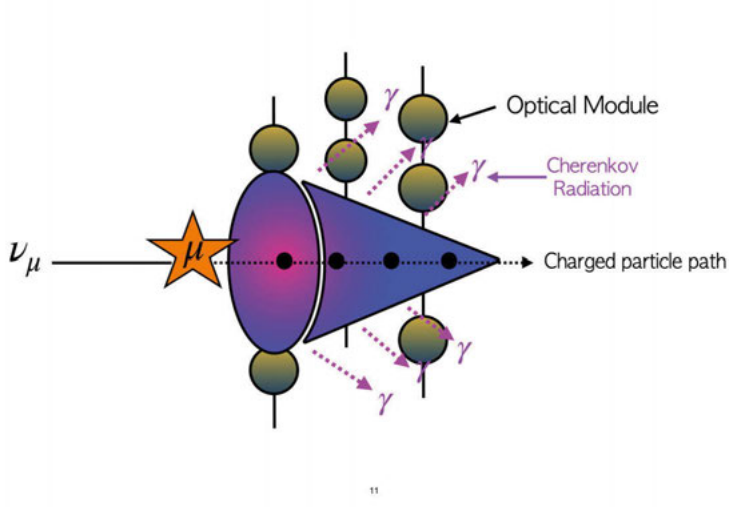

Figure 4.5. The cone of light in the axis of the charged particle's path. Depicted is the topology of the light emission shown as γ's, and how it would be observable for string detectors.

The typical medium for Cherenkov detectors is water or ice due to its high transparency, which allows Cherenkov light to travel considerable distances with minimal absorption and scattering. The energy threshold for particles to produce Cherenkov radiation depends on the medium. For example, in ice, where the refractive index is $n = 1.32$, the energy thresholds are: ≈ 0.78 MeV for electrons and positrons, ≈ 162 MeV for muons and ≈ 2.7 GeV for tauons [3]. As a charged particle passes through the ice, the total number of photons emitted per unit energy and unit length can be approximated using eq. 4.5:

$$\frac{dN_\gamma^2}{dE\,dx} \approx 157\,\mathrm{eV}^{-1}\,\mathrm{cm}^{-1}, \tag{4.6}$$

assuming $z = 1$ for relativistic electrons. However, absorption effects can reduce the number of observable photons, and scattering can alter the photon angle, making it challenging to reconstruct the interaction vertex or accurately estimate the neutrino energy. The transparency of water or ice mitigates these issues, making them ideal mediums for such detectors.

These photons are then detected by Photo-Multiplier Tube (PMT)s, which are often deployed in large arrays to cover significant volumes. Large-scale

[3] Only particles with $\frac{v}{c} > \frac{1}{n}$ can be detected. The energy threshold can be derived using the Lorentz factor $\gamma = \frac{1}{\sqrt{1-\frac{1}{n^2}}}$, and using the lepton's rest mass m_0c^2, leading to $E_{min} = \gamma m_0 c^2$

detectors, such as ANTARES/KM3Net in the Mediterranean Sea [9], Baikal-GVD in Lake Baikal [146], and IceCube at the South Pole, use strings of PMTs spaced out to monitor vast volumes of water or ice. Other detectors, like Super-Kamiokande (Super-K) [11], use a smaller but more densely instrumented volume to capture the Cherenkov light.

When using Cherenkov detectors to observe MeV neutrinos, the IBD interaction is the dominant detection channel due to the abundance of protons in water. In this interaction, a positron is produced, which generates Cherenkov radiation. However, no directionality can be extracted since the resulting positron does not travel in the neutrino's direction. On the other hand, elastic scattering of neutrinos with electrons, though a less frequent interaction [142, 10], does allow for some reconstruction of the neutrino's direction. Detectors like Super-Kamiokande, equipped with closely spaced PMTs, can reconstruct these events to provide directional information [142]. However, large-scale Cherenkov detectors like IceCube, with their more sparsely placed PMTs, cannot reconstruct individual events from the elastic scattering at these energies.

Nevertheless, thanks to the enormous photon statistics from IBD interactions, such detectors can provide a very good reconstruction of the burst timing. For HE neutrinos, DIS is the dominant interaction channel. This interaction, particularly involving muon neutrinos, allows for good directional resolution. Since the resulting muon can travel long distances, more sparsely placed PMTs with large instrumented volumes increase the possibility of observing these events.

Scintillation Detectors

Scintillation detectors utilize PMTs surrounded by a liquid scintillator, typically composed of hydrocarbons [147], significantly increasing the number of photons produced per unit of deposited energy. Due to these detectors' high abundance of free protons, MeV neutrinos are primarily detected via IBD or NC elastic scattering. The observables in these interactions include the energy loss from the charged particle, gamma rays from the annihilation of positrons, neutron capture, or the de-excitation of nucleons. Notable examples of detectors using scintillation technology include SNO+ [148], BOREXINO [149], JUNO [150], and NoνA [151], the latter of which employs both tracking calorimeters and scintillators.

Other Detector Types

In addition to scintillation detectors, other types of detectors are also effective for observing MeV neutrinos from SNe or other transient events. One such type is the liquid argon time projection chamber, which utilizes electric and magnetic fields within a gas or liquid chamber. As charged particles traverse the detector's volume, they ionize the medium, leaving trails of ionization

electrons. These electrons are then drifted to one side of the detector by an electric field, allowing for the event detection. This technology is particularly sensitive to electron neutrinos and antineutrinos via neutrino-nucleus quasi-elastic scatterings. An example detector employing this method is the Deep Underground Neutrino Experiment (DUNE) [152].

Another type of detector technology is those employing heavy nuclei, such as the HALO detector [153], which employs lead as a target material. In HALO, the neutron excess in lead blocks certain nuclear transitions, making the detector predominantly sensitive to electron neutrinos through the reaction $\nu_e + n \rightarrow e^- + p$. Lastly, low-threshold dark matter detectors can detect MeV neutrinos through coherent scattering interactions. In these detectors, when a neutrino scatters off a nucleon, such as argon or xenon, the recoil energy of the nucleon generates an ionization signal. This method is flavor-blind, allowing for some spectral information to be extracted from transients like CCSNe [142, 154].

5. The IceCube Observatory

The IceCube Neutrino Observatory (Fig. 5.1) is a cubic kilometer-sized neutrino detector located at the South Pole. The detector has a broad physics program, including measuring the characteristics of high-energy astrophysical neutrinos and searching for bursts of MeV neutrinos from supernovae. In this chapter, we will explore how IceCube observes neutrinos in the two energy ranges of interest: the tens of MeV range and the >100 GeV range. We will discuss the detector's design, data acquisition methods, event topologies, background management, and data processing techniques.

IceCube Detector

The detector consists of 86 strings of PMTs buried deep in the Antarctic ice in a hexagonal arrangement. Each string has 60 Digital Optical Modules (DOM) for a total of 5160 light sensors. The distance between each DOM varies depending on the location, with standard spacing between most strings being 125 m and 17 m between each DOM [156]. The exception is for 8 strings deployed deep in the ice called DeepCore (see Fig. 5.1), which are more closely spaced at 70 m between strings and 7 m between DOMs. Additionally, the observatory includes IceTop, a surface array consisting of 81 stations, each with two frozen water tanks. IceTop primarily studies CR air showers and helps in background discrimination. The Antarctic ice, where IceCube is situated, is exceptionally clear, with photon absorption lengths over 100 m. This clarity allows a single DOM to monitor several hundred cubic meters of ice. However, there are some impurities at certain depths, most notably a dust layer at around 2000 m (see Fig. 5.1). This layer increases optical scattering and photon absorption, complicating the reconstruction of events occurring in this region.

5.1 Digital Optical Modules (DOMs)

The DOM (Fig. 5.2) consists of a PMT and a mainboard that controls and handles the data output. These components are encased in a pressure housing, a 13 mm thick glass sphere capable of withstanding sufficient pressure to survive refreezing during deployment in the drill hole. This housing also has a silicon base gel to couple the PMT to the glass sphere optically. Each DOM is

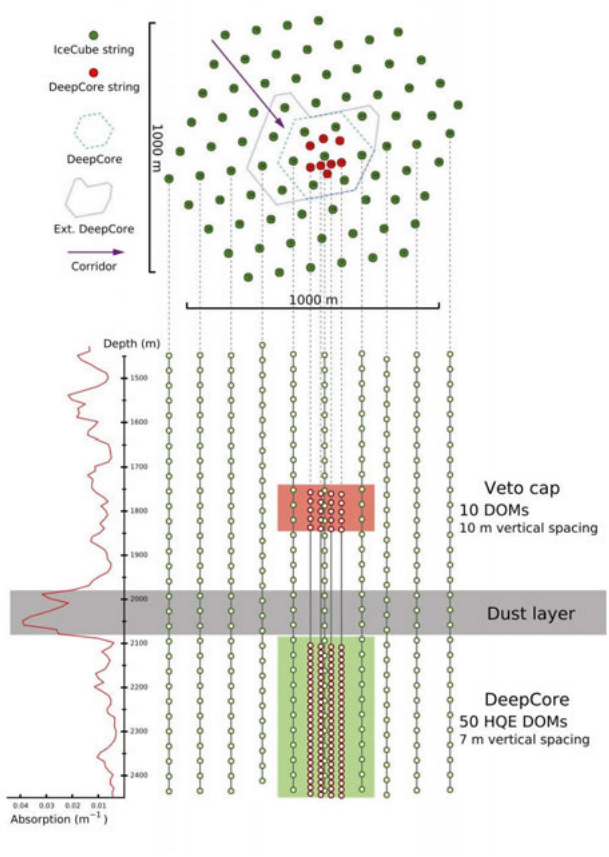

Figure 5.1. Upper plot shows the string placement in the detector, highlighting the different components. Lower plot shows the photon absorption as a function of depth, with the dust layer and the DeepCore array highlighted. Reproduced from [155].

connected to a penetrator, which handles the power and communication with neighboring DOMs and the surface and has a flasher board consisting of 12 LEDs for calibration and ice characterization, which can be individually selected to emit short-duration light pulses. When a photon arrives at a PMT, it is first absorbed by the photocathode, which releases an electron. This electron is then accelerated through a series of dynodes that amplify the signal. This amplification process results in a photoelectron (PE) gain of $\sim 10^7$, enabling the detection of even single photons. The amplified signal is converted into a voltage change at the anode, with a detection threshold set at 0.25 PE, which corresponds to the detection of one or two photons. The resulting electrical signal is then transmitted to the DOM mainboard, which undergoes waveform digitization with nanosecond resolution on pulse widths [156]. The PMT is sensitive to photons in the 300-650 nm range (UV to visible light) and has

a dark noise rate of $\sim$ 250 Hz, predominantly from radioactive decay in the glass sphere [156].

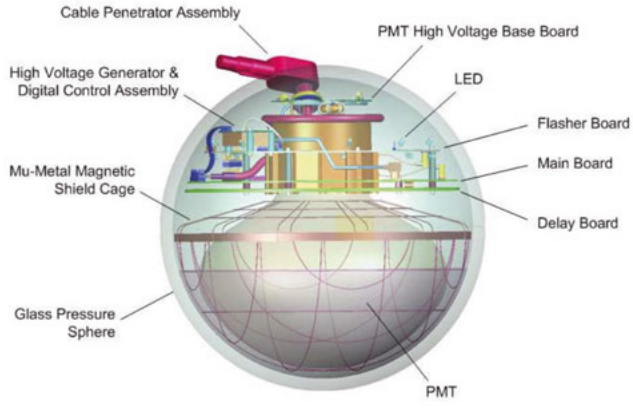

Figure 5.2. Schematic view of the digital optical module, highlighting the different components. Reproduced from [157].

5.2 From Neutrino Interaction to Detection

When a HE neutrino interacts near or at the detector volume, it does so primarily via the deep inelastic process (as established in Chapter 4). Depending on the final state, different signatures will be observed. CC interactions of ν_μ produce a muon that can travel long distances before losing its energy through radiative losses like ionization or Bremsstrahlung [158]. ν_e produces an electron that results in a local electromagnetic shower. ν_τ produce a tau, which has a short lifetime ($\tau_\tau : \tau_\mu \approx 10^{-13} : 10^{-6}$ s). NC interactions are observed as hadronic showers. We will briefly review the types of signatures observed by IceCube before discussing the trigger and data acquisition.

Neutrino Event Signatures

Tracks

Tracks are created through ν_μ CC interactions with nuclei. At TeV energies, it is observed as an elongated arm topology (see Fig. 5.3, and Fig. 5.4). The muon maintains the directionality of the incoming neutrino with a resolution of $\Delta\Psi \approx 0.7^\circ(\frac{E_\nu}{TeV})^{-0.7}$, where E_ν is the neutrino energy, providing excellent pointing. Although it can be challenging to estimate the neutrino energy since the interaction can occur outside of the detector volume, it also allows for sensitivity to an even larger flux of neutrinos by observing the outgoing muon of interactions that occurred outside the instrumented volume.

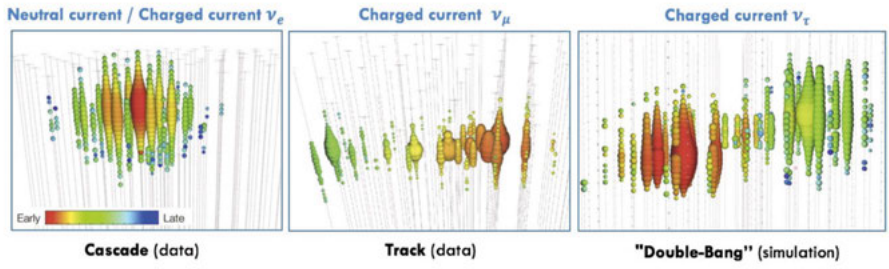

Figure 5.3. Event views are visual representations of the registered events for different topologies, such as cascade (left), track (middle), and double-bang (right). The color represents the observation of photon time, where red is the earliest and blue is the latest. Reproduced from [159].

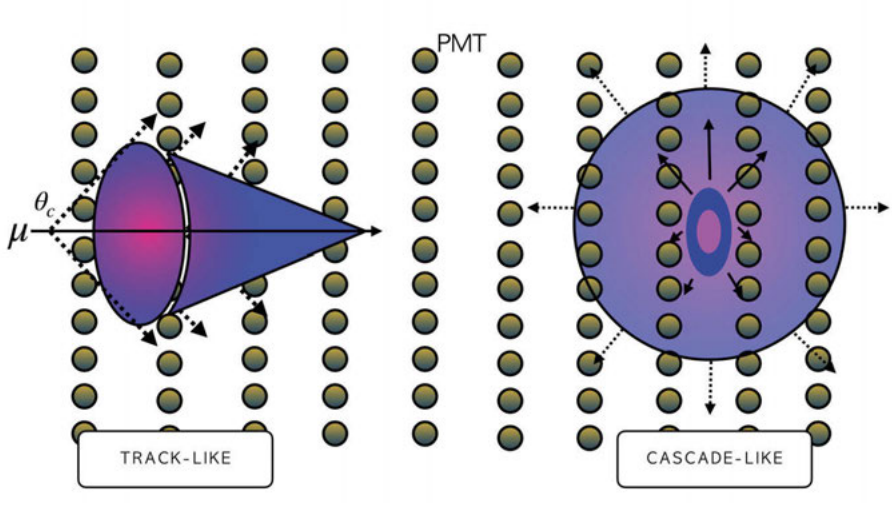

Figure 5.4. Cherenkov light patterns for track-like and cascade-like.

Cascades

These can be created through CC of ν_e and ν_τ or all flavor NC interactions. The observed Cherenkov light signal is from the hadronic or electromagnetic showers produced, with a point-like vertex, which spreads out over short distances of a few meters, with the length increasing with $log(E)$ [160]. The length scale in which these particles lose energy is below the DOM spacing; resolving individual particles is challenging, leading to a spherical topology. Since the total amount of light is proportional to the total cascade energy, if the event is contained within the instrumented volume, it will be ideal for energy reconstruction. However, the angular resolution is not as good as for tracks, with $\Delta\Psi \sim 5^\circ - 15^\circ$ [161].

Double Bangs

This is exclusive to ν_τ CC interaction since a τ can travel approximately 50 m per PeV before decaying [162]. The resulting signature is an initial cascade caused by the particle shower in the first interaction, followed by a second cascade as the tauon decays. If the ν_τ is below PeV, it will travel only shortly before decaying, and it could end up indistinguishable from a cascade because of the DOM spacing.

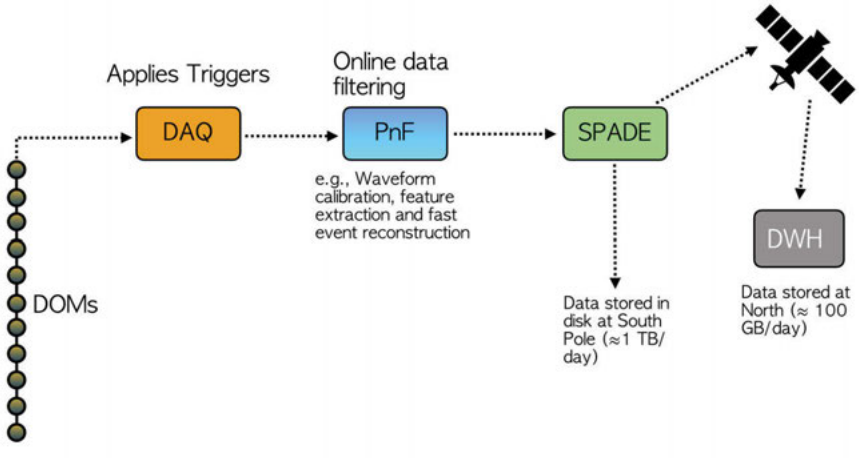

Figure 5.5. A high-level view of the data flow in IceCube; from the DOMs to the Data Acquisition (DAQ), to the Processing and Filtering (PnF), to the South Pole Archival and Data Exchange (SPADE), to the satellite transfer to the Data Warehouse (DWH).

Digitization of Signal

Cherenkov photons are produced from neutrino interaction, which is observed by the PMT, initializing the waveform digitization. After this, there are several stages before the photons observed can be analyzed, as shown in the high-level depiction in Fig. 5.5. From the DOMs, the signal goes to the data acquisition (DAQ) software running in the DOMHubs, which are computers connected to the strings at the IceCube lab (ICL). The DAQ handles data reduction, applies triggers, and gives as output an *event*. From the DAQ, these events are passed on to the Processing and Filtering (PnF), where additional filters are applied to identify interesting events that meet certain physics stream criteria and to reduce the data volume from $\approx$ 1 TB/day to $\approx$ 100 GB/day[1] [156] to fit the satellite bandwidth. This subsection will cover waveform digitization to data transmission to the North.

[1] It is important to note that the 1 TB of data is saved to disk for future usage.

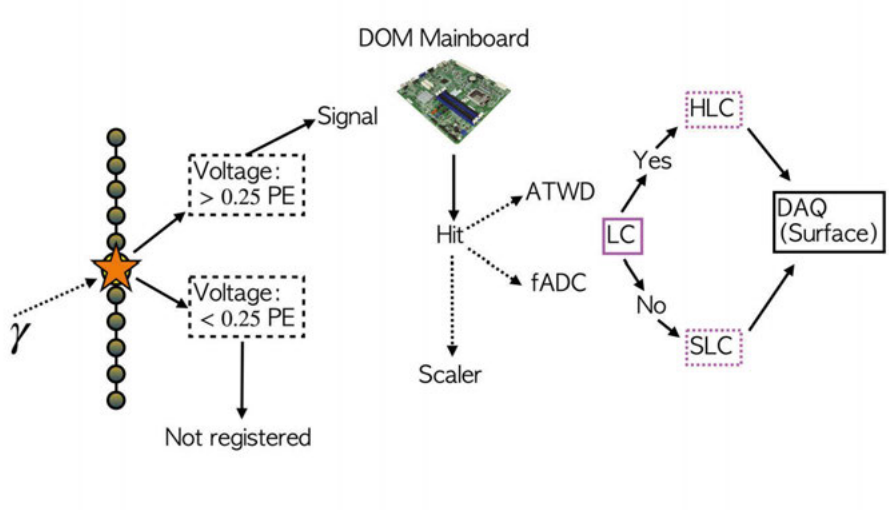

Figure 5.6. Schematic of the signal digitization to be transmitted to the surface, with the different conditions for trigger and the different streams through which the signal can be processed. When a photon is observed, depending on photoelectrons (PE), it can be registered as a signal in the digital optical module (DOM) mainboard as a hit. It can then be readout in different modes, such as the Scaler stream, analog transient waveform digitizer (ATWD), and a fast analog-digital converter (fADC). A local coincidence (LC) is searched for for the two latter ones. Depending on whether the neighboring DOMs observed an LC, either the hard local coincidence (HLC) or soft local coincidence (SLC) is satisfied. Finally, the signal goes to the data acquisition (DAQ).

To estimate the initial properties of the neutrino that interacted with the nuclei in ice, the event is reconstructed from the photons observed in the DOMs. If the anode voltage exceeds 0.25 PE, the signal is passed to the DOM mainboard, where it will be processed as a DOMLaunch or a *hit* (Fig. 5.6). It can then be processed to a signal in three streams: an analog transient waveform digitizer (ATWD), a fast analog-digital converter (fADC), and a scaler. We will cover ATWD and fADC below, with the scaler stream covered in Section 5.4.

Readout mode	Condition	Resolution	Sampling rate	Capture
ATWD	HLC	3 ns	290 MHz	128 samples
fADC	Above threshold	25 ns	40 Hz	256 samples
Scaler	Continuous sampling	1.64 ms	–	–

Table 5.1. *The different streams of signal digitization.*

ATWD
When waveform digitization is initialized, a local coincidence (LC) signal is sent to the next-to-next DOMs (Fig. 5.8). If the DOMs have observed a signal within the coincidence time window of $\pm 1\,\mu$s, the hard local coincidence (HCL) condition is satisfied and full data readout is done, with digitization done by the ATWD chip. The ATWD records a high-resolution waveform in bin width of 3.3 ns with 128 samples, for a total of ~ 420 ns[2]. This chip has a deadtime of about $\sim 30\mu$s during readout, which will be unavailable for data taking. After about 420 ns, the digitization is done by the fADC chip, and the data is sent to the DAQ. If the neighboring DOMs observed no LC, it is classified as a soft local coincidence (SLC), and the waveform is terminated at the end of the LC time window of $2.45\,\mu$s to prevent sending unnecessary data to the surface.

fADC
The fADC records a more coarse version of the waveform in 25 ns bins with 256 samples, for a total of $6.4\,\mu$s. It scans the waveform continuously without any deadtime. However, the fADC is tied to the ATWD, needing correspondence with an ATWD readout; if a HLC is met, both the ATWD and fADC full sample lengths are sent to the surface; however, if it is an SLC, only the fADC sample is sent.

Surface Data Aquisition

When the hits arrive at the DAQ in the *DOMHub*, the second step in data reduction occurs. The hits from each DOM are read out by *StringHub*, responsible for reading and passing the data to the *HitSpool* stream, which saves the hits locally on disk. The HitSpool stream will be covered in more detail in Section 5.4. *StringHub* consists of a front-end called Omicron, which controls all of the DOMs connected to the hub, forwarding all of the data, from hits, monitoring, and calibration stream, to a back-end called Sender, which takes care of saving the hits locally in a stream called HitSpool and forwards a compact form to the local triggers that run in parallel. The triggers look for clusters of HLC hits [156], indicating that a particle interacted in the detector instead of dark noise. This search for multiplicity is temporal and spatial, where the spatial component could involve a geometry centered around the hit. There are five triggers that the hits go through: Simple Multiplicity Trigger (SMT), volume trigger, string trigger, slow-particle trigger, and fixed-rate trigger. For most physics cases, the first three are commonly used.

SMT This is the most commonly used trigger algorithm in IceCube. The requirement is a minimum number N of HLC hits (see Fig. 5.8) in the detector within a time frame window several μs depending on the N, with the time

[2]This is sufficient time to reconstruct light that was produced tens of meters away [156]

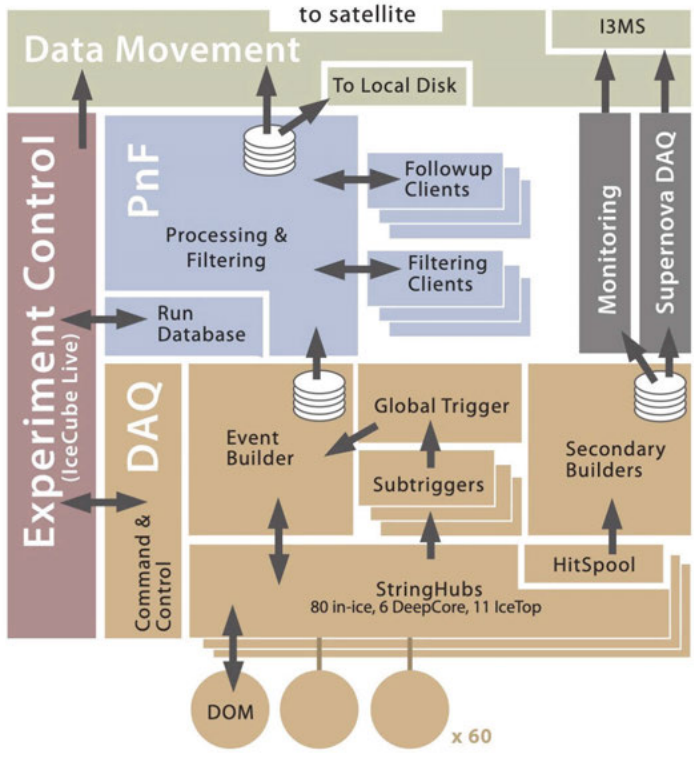

Figure 5.7. Schematic showcasing the different streams and steps of surface data flow. Reproduced from [156].

window sliding further out as long as the multiplicity condition is met. The time window and multiplicity utilized in triggers is related to the time of photon propagation with respect to the spacing between DOMs, which differs for DeepCore or regular in-ice array. SMT8 is the standard trigger, which looks for a multiplicity of 8 [156, 163] within a time window of 5 μs.

Volume Trigger The volume trigger looks in a cylindrical volume around the hit DOM for other HLC hits, looking for a specific N of multiplicity, helping to identify low energy events that do not meet the SMT criteria (see Fig. 5.8).

String Trigger The string trigger uses a locality condition like the volume trigger, but searches within the same string for a multiplicity (see Fig. 5.8) .

Since many events will meet the condition for several triggers, which run in parallel, a *global Trigger* is applied to merge the triggers in the same readout window to avoid the same hits contributing to different events. Then the *event builder* receives the requests from the global triggers (Fig. 5.7), extracts the individual readout time windows, and then sends a request to StringHub,

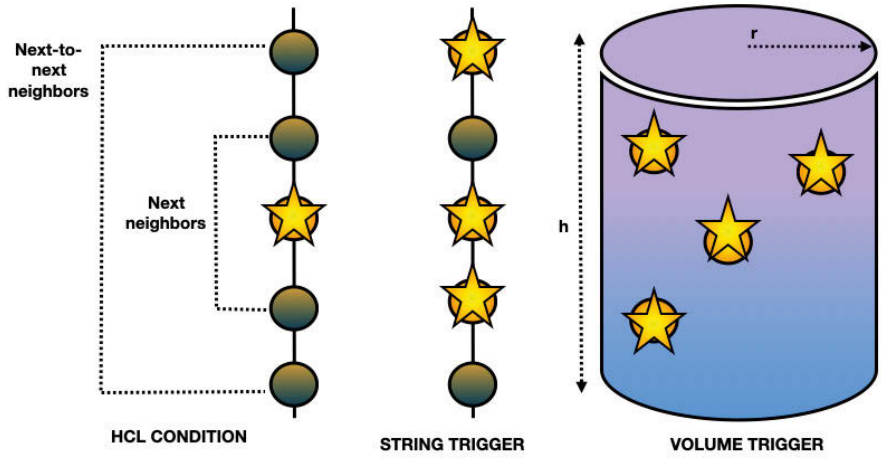

Figure 5.8. The three widely used triggers; HCL condition which the simple multiplicity trigger (SMT) makes use of, the string trigger which uses a locality condition and the volume trigger which searches within a volume for hits.

responding with a list of hits (or payloads) within the time window. These payloads [3] are assembled into events with the trigger data and written to disk in chunks, waiting for retrieval by the PnF system.

Data Filtering and Event Reconstruction

After the DAQ system, events are forwarded to the Processing and Filtering (PnF) stage, where they undergo further data reduction. This stage includes calibrating and monitoring, generating real-time alerts for interesting astrophysical events, performing initial event selection to create subsets for specific physics analyses, and producing long-term archival data files, such as the compact Data Storage and Transfer (DST) format, which logs event details like time, triggered DOMs, and hits participating in the event [164, 156]. During this phase, multiple reconstruction filters are applied to determine the vertex position, direction, energy, and goodness of fit, matching events to hypotheses like cascades or tracks. Among these, five core filters are central to IceCube's physics analyses [156]:

Muon Track Filter
This filter looks for high-quality track events from all directions. For upgoing events, all triggered energies are selected. In contrast, only high-energy events are selected for down-going events to reduce the background from atmospheric muons.

[3] Payload is a minimum data packet

Shower Event Filter
This filter looks for large energy deposition at or near the instrumented volume.

High Charge Filter
This filter searches for high-energy deposition with a recorded charge of 1000 PE or above, targeting the highest-energy neutrino events.

CR Filter
These look for extended air shower events in IceTop, providing inputs for analyses that target flux, spectrum, and composition of CRs.

DeepCore Contained Event Filter
This filter looks for contained low energy (10-100 GeV) events in the DeepCore sub-array. It is used for neutrino oscillation effects and indirect signatures.

5.3 IceCube and High-Energy Neutrinos

Challenges with Detection of High-Energy Neutrinos

High-energy neutrinos are a double-edged sword; as the energy increases, so does the probability of interacting with matter, which is good for observing them, but they may not arrive at the detector as they cross through Earth. Depending on the angle of arrival, the probability of absorption by Earth increases, as we can see in Fig. 5.9, where, for example, for a neutrino arriving at a zenith angle of 180°, it would cross the entire core-mantle. For the highest energies O(>PeV), it would result in a transmission probability near 0%, effectively making Earth opaque to neutrinos. In addition to the challenge with absorption, the astrophysical flux of neutrinos goes down with increasing energy, with many orders of magnitude smaller than CRs. In this section, we will cover the background affecting HE astrophysical neutrino searches and how they are suppressed.

Cosmic Rays - Our Largest Background

The majority of events that IceCube observes are atmospheric muons produced by CR interactions in the atmosphere, at a rate of 2.5-2.9 kHz [156], and atmospheric neutrinos, also caused by the CR interactions in the atmosphere, although at a factor of 10^{-6} less frequent than the muons [167]. These atmospheric muons and neutrinos constitute our largest background source, as they can mimic the signal.

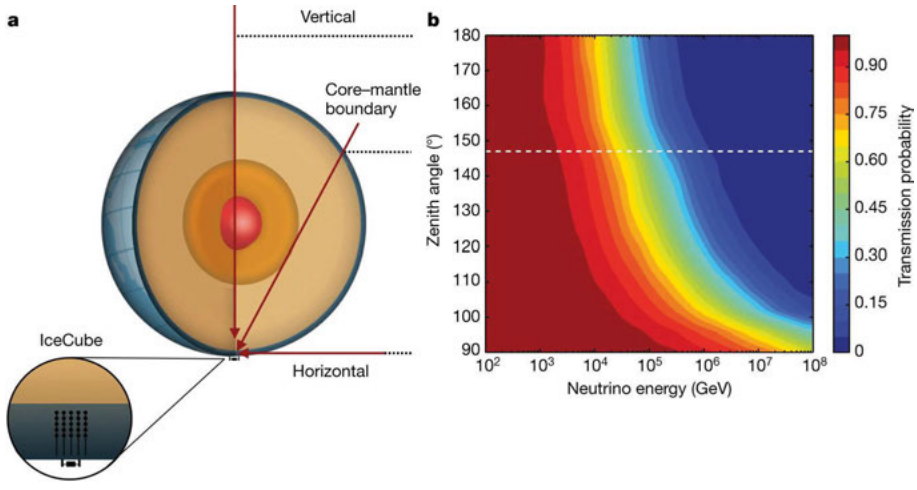

Figure 5.9. Neutrino transmission as a function of arrival angle and energy. a) Depicts Earth and the arrival angle of the neutrino. b) The transmission probability as a function of the zenith angle and the neutrino energy. The white dashed line represents a neutrino trajectory that passes through the core-mantle boundary. Reproduced from [165].

Atmospheric Muons and Neutrinos

Atmospheric muons are produced when CR, which have an isotropic flux and energies ranging from GeV to 100 EeV (see Fig. 5.10), interact with nuclei in the atmosphere. Since the CR composition is predominantly protons [168], a hadronic shower will be produced, with unstable particles like pions π and kaons K and D mesons, which then decay to muons and neutrinos:

$$\pi^{\pm} \rightarrow \mu^{\pm} + \overset{(-)}{\nu}_{\mu} \tag{5.1}$$

$$K^{\pm} \rightarrow \mu^{\pm} + \overset{(-)}{\nu}_{\mu}. \tag{5.2}$$

Most of these unstable particles never make it to the ground since they decay in the upper part of the atmosphere; however, a small portion, namely muons and neutrinos, travel through all the way, reaching the detector. There are two different contributions to the atmospheric neutrino background; conventional and prompt.

Conventional

In the conventional scenario, as CRs interact with nuclei, $\pi^{\pm}$, and $K^{\pm}$ are created, where they decay as outlined in eq. 5.1 and 5.2. However, these particles are relatively long-lived, $\pi^{\pm} \approx 10^{-8}$ s, having sufficient time to undergo energy losses through collisions and reducing the final neutrino energy. Due to the energy losses of the mesons, the resulting spectrum is softer with $E^{-3.7}$ vs.

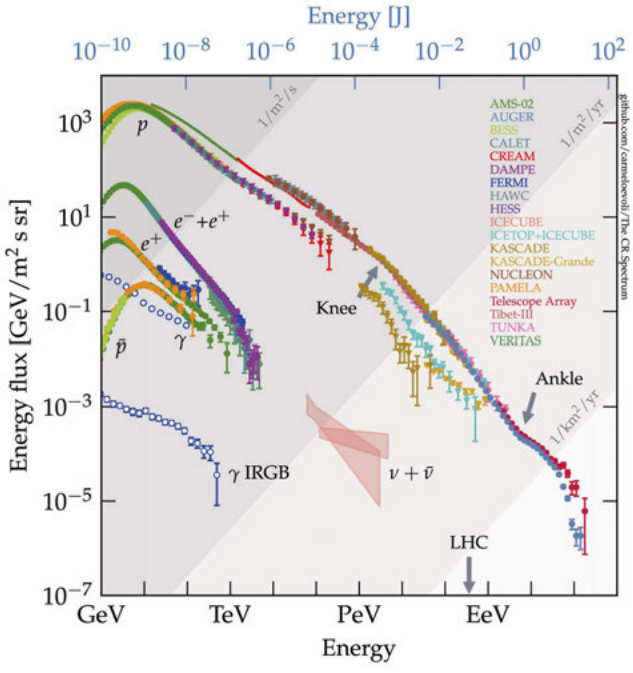

Figure 5.10. All particle cosmic ray spectrum as measured by different experiments. Antiprotons and positrons are included in the plot, but these are typically from secondaries that form when primaries collide with the interstellar medium [70]. Reproduced from [166].

$E^{-2.7}$ of the CR. The resulting flux is the conventional atmospheric neutrino flux, the dominant contribution to the atmospheric neutrino background [169].

Prompt

Heavier mesons can also be produced when a CR interacts with nuclei in the atmosphere, namely D-mesons, which are very short-lived O(10^{-13} s) and decay before undergoing energy losses [170]. The resulting neutrinos produced through the decay of charm mesons, named the prompt atmospheric neutrino flux, will have a spectrum following that of the CR ($E^{-2.7}$), with a flux that is smaller by several orders of magnitude than that of the conventional.

Background Suppression

Atmospheric Muon Suppression

Several methods can be employed to suppress atmospheric muons and neutrinos. In this subsection, we will outline how these are handled.

The detector is split into two regions: an up-going region (*Northern sky*), where events originate from below the detector, and a down-going (*Southern*

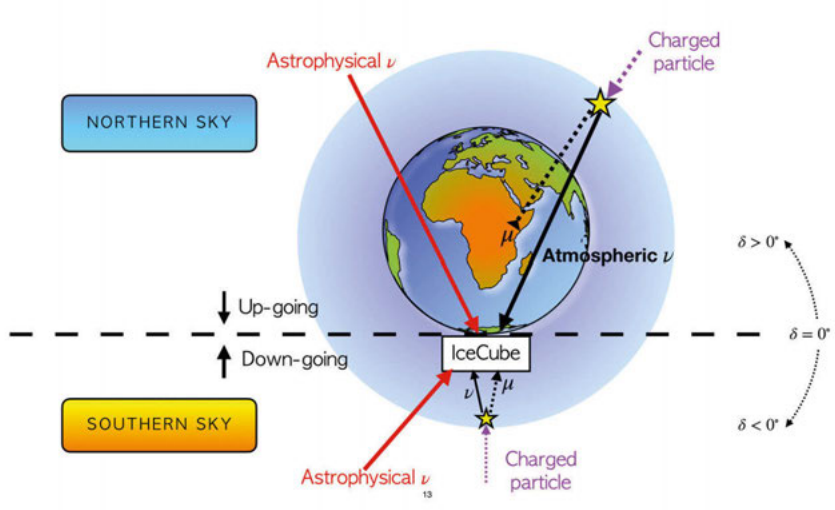

Figure 5.11. Orientation of events in IceCube, depicting the up-going as events coming from the northern hemisphere and the down-going as events coming from the southern hemisphere, along with the declination coordinate, where events from the Southern sky are those with $\delta < 0^\circ$ and those from Northern sky are $\delta > 0^\circ$.

sky) region, where events originate from above the horizon (Fig. 5.11). In order to suppress the atmospheric muons, two strategies can be used: looking only at events originating from the Northern sky (directional cut) or using contained events, which involve the interaction vertex.

Directional Cut: Even with the highest energy atmospheric muons, although they can travel far distances, they cannot travel hundreds and hundreds of kilometers without getting absorbed by Earth; therefore, up-going muons or muons originating from the Northern sky are assumed to be of astrophysical origin, since the probability of an atmospheric muon traveling through all of the Earth and making it to the detector is very low. Therefore, Earth acts as a natural filter for atmospheric muons, and this can be seen in the angular distribution of atmospheric muons in Fig. 5.12, where the muon flux drops significantly by over six orders of magnitude as we move towards crossing some Earth ($cos(\Theta_z) \approx 0$). However, this strategy would limit us to only using events originating from the Northern sky.

Interaction Vertex: If we want to be able to use the Southern sky, we can make use of events that are contained within the instrumented volume by applying an interaction vertex condition, where only events that have the interaction vertex within the instrumented volume are accepted. This can be done by employing veto layers since atmospheric muons passing through the detector will be first seen in the outer layers, whereas neutrinos can pass through the outer layers before interacting (see Fig. 5.13).

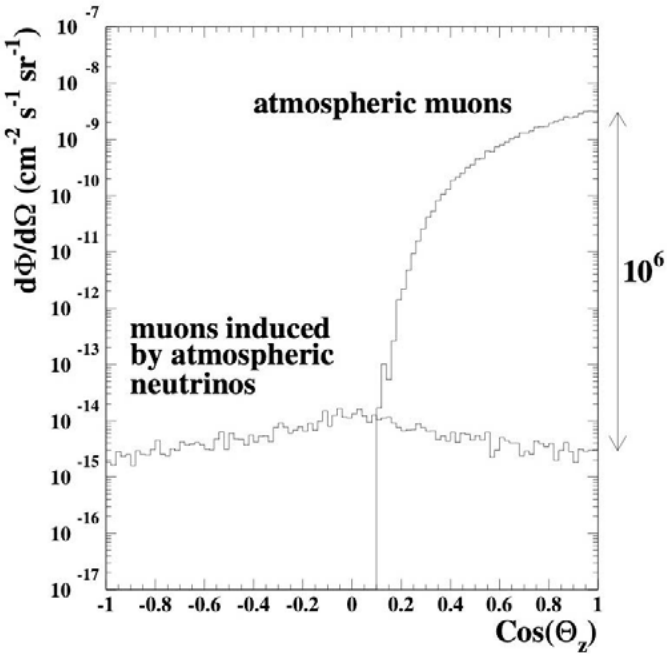

Figure 5.12. Angular distribution of atmospheric muons (> 1 TeV) and neutrinos. The y-axis denotes the flux and the x-axis denotes the zenith angle in the sky, where $-1 < cos(\Theta_z) < 0$ represent the Northern sky or up-going events, and $0 < cos(\Theta_z) < 1$ represent the Southern sky, or down-going event.s Reproduced from [171].

Atmospheric Neutrino Suppression

Finally, to handle the atmospheric neutrino background, we can make cuts in the energy requirement of events, since atmospheric neutrinos follow a softer spectrum than that of astrophysical neutrinos (see Fig. 5.14), with about $E^{-3.7}$ for atmospheric neutrinos vs E^{-2} for astrophysical neutrinos.

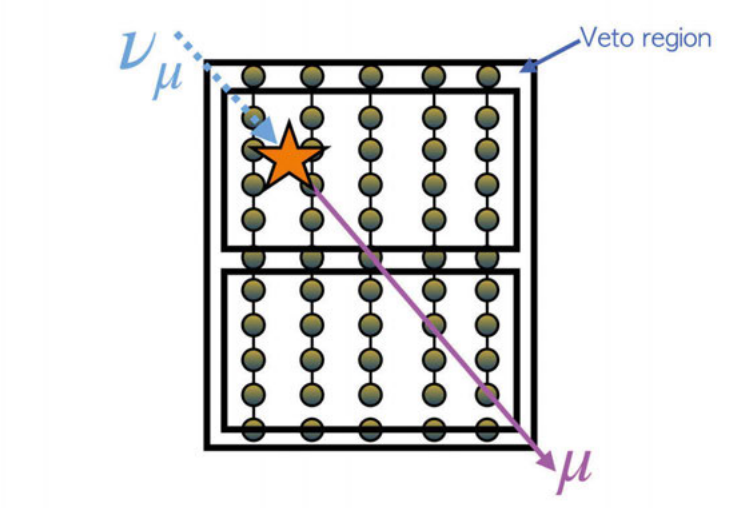

Figure 5.13. Application of detector veto layers, where events that have the interaction vertex in the veto layer are discarded. In the illustration, a muon neutrino with interaction vertex within the detector volume is shown.

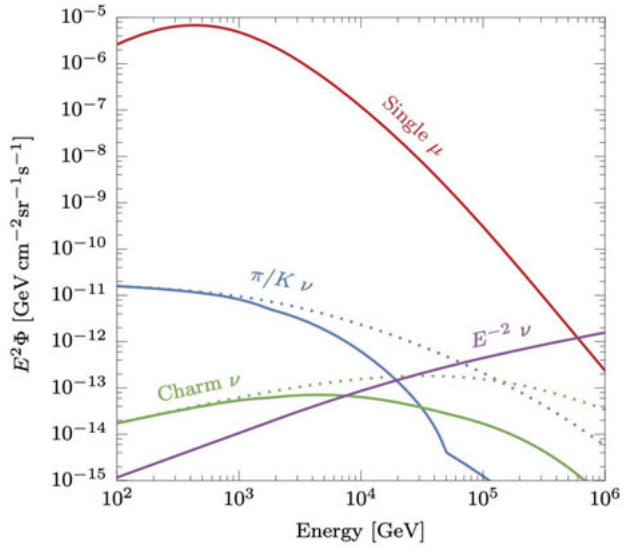

Figure 5.14. Fluxes for atmospheric neutrinos, muons, and astrophysical neutrinos observable by IceCube for down-going events. The red curve is for atmospheric muons, the blue curve for conventional atmospheric neutrinos, the green curve for prompt atmospheric neutrinos, and the purple for the astrophysical neutrinos, where the dotted lines represent the total interacting flux of all flavors and the solid lines represent the flux that arrives at the detector without accompanying muons. Reproduced from [167].

5.4 IceCube and Low-Energy Neutrinos

In addition to HE neutrinos (O(>100 GeV)), IceCube can also observe low-energy neutrinos from CCSNe and other transients, which are in the order of 10s of MeV. These low-energy neutrinos are primarily observed via IBD, with minimal contributions from other neutrino flavors. Due to the short track length of the positron–about $0.5\,cm\,\frac{E_\nu}{\mathrm{MeV}}$ [10]–a neutrino with an average energy of approximately 10 MeV will produce a track length roughly 5 cm. The number of Cherenkov photons radiated by this positron is around $N_\gamma \approx 178 \cdot E_{e^+}$ [172, 10]. This short track length, combined with the large spacing between PMTs and strings, typically results in only single photon hits being detectable, as shown in Fig. 5.15. Observing MeV neutrinos differs from observing high-energy ones; in this case, the detector is considered a counting experiment, with all in-ice DOMs functioning as independent detectors. Consequently, the signal is identified by a collective rise in single hits across the detector. The remainder of this section will discuss IceCube's methods for detecting MeV neutrinos from transients like CCSNe, the main background sources in this energy regime, and the strategies used to handle them.

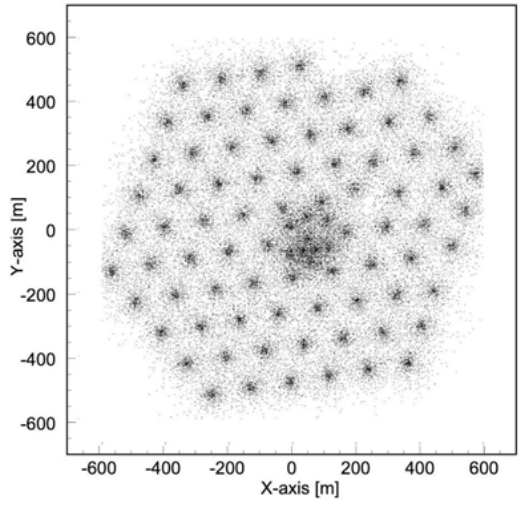

Figure 5.15. Simulation of detected IBD photons in the detector. Reproduced from [10].

Low-Energy Data Stream

In Section 5.2, we discussed the various data streams, including the fADC and ATWD. There is also a third stream specifically for supernova analysis and other MeV transients: the *scaler* stream (see Fig. 5.7). The DAQ system's

StringHub continuously requests data from the DOMs for tasks such as calibration and monitoring. Among these requests is the scaler data, which acts as a basic hit counter within a pre-defined time bin (see Fig. 5.19). This scaler stream is independent of the hit data stream.

Scalers

The DOMs constantly measure the untriggered hit rate in pre-defined bins of 1.6384 ms [10][4]. To the pre-defined bin, a dead time of 250 μs is applied, which helps to reduce the noise rate. Then a timestamp is assigned, constituting the scalers, which are merged, synchronized, and binned in 2 ms, becoming the supernova payload for SNDAQ real-time rate analysis. Due to the limited bandwidth of the satellite, the payload is further re-binned in 0.5 s and then further binned in 1.5 s, 4 s, and 10 s for different physics motivations [173, 174], allowing the data to be transferred quickly to the North if there is an excess in the hit rate[5]. This payload is then stored in a 0.5 s bin format and transferred to the North for archival and future analyses.

Real-time Analysis

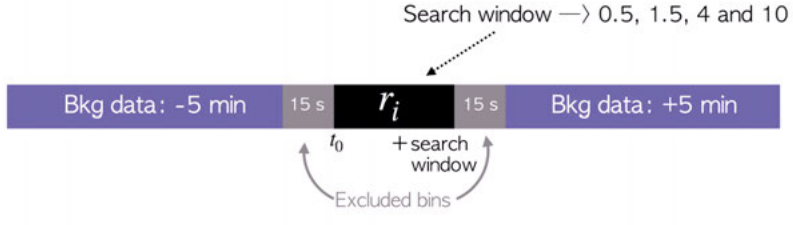

Figure 5.16. Schematic of SNDAQ Analysis, where the black region denotes the search bin r_i, with a start time t_0 with respective search window size, in grey denotes the excluded bins, and in purple the background bins used for the computation of the mean and standard deviation.

SNDAQ is a system that monitors the detector rate and searches for nearby CCSNe or MeV transients by monitoring for a collective deviation in the hit

[4]The bin size does not have a specific physics case but is based on a firmware that adds up all the asynchronous PMT hits in a pre-defined interval length given by the internal clock cycle.
[5]In order to have 24 hr coverage, a dedicated satellite is used for real-time alerts.

rate across the detector. The rate increase on top of the DOM noise can be quantified as:

$$R_i(t) = \varepsilon_{deadT} n_{ice} \int_0^\infty dE_\nu \Phi_\nu^{detector}(E_\nu, t) \int_0^\infty dE_e \frac{d\sigma}{dE_e}(E_\nu, E_e) V_{eff}^{e^\pm}(E_e) \quad (5.3)$$

where ε_{deadT} is the deadtime or efficiency factor of the DOM, n_{ice} is the density of targets in ice, E_e is the lepton energy, $\frac{d\sigma}{dE_e}(E_\nu, E_e)$ is the differential cross-section for the interaction of interest, $V_{eff}^{e^\pm}(E_e)$ is the effective volume for a single photon in the detector and

$$\Phi_\nu^{detector}(E_\nu, t) = \frac{\Phi_\nu(E_\nu, t)}{4\pi d^2} = \frac{L_\nu(t)}{4\pi d^2 \langle E_\nu \rangle(t)} \cdot f(E_\nu, \langle E_\nu \rangle(t), \alpha(t)) \quad (5.4)$$

is the differential neutrino flux for a given neutrino energy at the detector, where $\Phi_\nu(E_\nu, t)$ is the transient flux at source and d is the distance from source, $L_\nu(t)$ is the time and energy-dependent luminosity at source, $\langle E_\nu \rangle(t)$ is the mean energy and $f(E_\nu, \langle E_\nu \rangle(t), \alpha(t))$ is the normalized neutrino energy distribution or energy pdf, where α is the pinch parameter which determines width of the neutrino energy spectrum:

$$f(E_\nu, \langle E_\nu \rangle(t), \alpha(t)) = \left(\frac{1 + \alpha_\nu(t)}{\langle E_\nu \rangle(t)} \right)^{1+\alpha_\nu(t)} \cdot \frac{E_\nu^{\alpha_\nu(t)} exp(-(1+\alpha_\nu(t)) E_\nu / \langle E_\nu \rangle)}{\Gamma(1+\alpha_\nu(t))} \quad (5.5)$$

SNDAQ analyzes the 500 ms rate in real-time, defining a background region of 10 minutes; ± 5 min centered around the sliding search window r_i, excluding ± 15 s around the search bin to prevent long signals affecting the background window (see Fig. 5.16). The methodology for this search is to use a one-dimensional Gaussian likelihood to maximize the collective noise rate from all DOMs $\Delta\mu$, where each DOM contributes to the individual rate $r_i = \frac{N_i}{\Delta t}$, where N_i are the observed hits per i DOM and Δt is the time interval under investigation (for example, 0.5 s). The search is performed assuming that there is no DOM-to-DOM noise correlation. With a sufficiently large time interval, the expectation value for the DOM noise rate $\langle r_i \rangle$ and standard deviation $\langle \sigma_i \rangle$ follow a log-normal distribution approximated to a Gaussian [173]. The most likely collective noise rate deviation, which gives the statistical excess above individual DOM rates, can be obtained by maximizing the log-likelihood of

$$L(\Delta\mu) = \prod_{i=1}^{N_{\mathrm{DOM}}} \frac{1}{\sqrt{2\pi}\langle \sigma_i \rangle} \exp\left(-\frac{(r_i - (\langle r_i \rangle + \varepsilon_i \cdot \Delta\mu))^2}{2\langle \sigma_i \rangle^2} \right) \quad (5.6)$$

where N_{DOM} is the number of DOMs in the detector and ε_i is the photon detection efficiency[6]. By log-maximizing equation 4.2, we can obtain the collective noise deviation rate and its approximate uncertainty;

$$\Delta\mu = \sigma^2_{\Delta\mu} \sum_{i=1}^{N_{\text{DOM}}} \frac{\varepsilon_i(r_i - \langle r_i \rangle)}{\langle \sigma_i \rangle^2} \quad \text{and} \quad \sigma^2_{\Delta\mu} = \left(\sum_{i=1}^{N_{\text{DOM}}} \frac{\varepsilon_i^2}{\langle \sigma_i \rangle^2} \right)^{-1} \tag{5.7}$$

where $\langle \sigma_{\Delta_\mu} \rangle^2$ is the variance of Δ_μ. From there, the significance ξ of the event is computed through

$$\xi = \frac{\Delta\mu}{\sigma_{\Delta\mu}}. \tag{5.8}$$

The nature of this analysis is to assume that each DOM is independent and described by a pure Poissonian noise with $\mu = 0$ and $\sigma = 1$. However, this is not the case due to background sources, with atmospheric muons increasing the spread by $\sigma \approx 1.45$ [172, 175]. We will cover this next and how it is handled in the online real-time system.

Background

The average noise rate for the DOMs is about ≈ 540 Hz, with variations due to temperature, which is depth dependent [173]. Since the dominant background is other sources that produce single hits on the DOMs, the signal will be mixed in with the noise. The noise contribution to the hit rate can be broadly categorized into single-DOM correlations and DOM-to-DOM correlations [176, 177].

Single-DOM Correlations

These refer to correlations within one DOM, caused mainly by two components: thermal noise from electronics/PMT and radioactive decay-induced scintillation from the PMT and glass sphere [178]. These are the largest noise sources, with a 300-500 Hz rate, depending on the depth [178]. These noise sources have a duration in the O(100 μs) and can be suppressed by adding an artificial dead time, as discussed in the scaler stream above. The artificial deadtime of about 250 μs is applied to every hit in the DOM, which reduces the noise rate from 540 Hz to 285 ± 26 Hz [173], at the cost of 13% efficiency of the signal [10].

[6]This is a correction factor for the i*th* DOM. Each DOM has a module-specific quantum efficiency, whereas normal DOMs have an $\varepsilon_i \approx 1$, and high-quantum efficiency have about $\varepsilon_i \approx 1.35$ [175].

DOM-to-DOM Correlations

These inter-DOM correlations are mainly due to atmospheric muons. Although they are not a significant contribution to individual optical modules–at about 3% of the total count rate [179]–since these hits are correlated, they cause a broadening in the significance ξ distribution (see Fig. 5.17). As mentioned in the previous section on background sources for HE neutrino searches, CRs are a significant source of background for any IceCube analysis, as they can easily mimic signals. Atmospheric muons are also a source of background for the low-energy supernova data stream analysis since the time-integration of the analysis is in the $O(10^3 - 10^7)$ longer than the crossing time of the muon of a few μs [177].

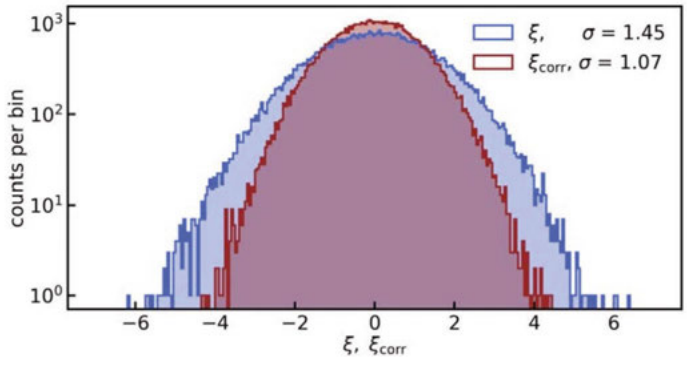

Figure 5.17. Distribution of uncorrected significances ξ in blue and muon-corrected significances ξ_{corr} in red, where we can see the reduction in the spread of the distribution. Reproduced from [180].

At high energies (primaries >1 PeV), CR can produce muons that reach the in-ice detector in bundles of 20-10000 muons, which trigger many optical modules, with a large majority triggering an SMT8. IceCube observes these atmospheric muons at an average rate of 16 Hz per DOM [176], with a seasonal variation of about ±8-10% [164, 181], where the modulation is related to the temperature variation, as we can see in Fig. 5.18.

This temperature dependence of the atmospheric muon rate R_μ can be explained via this simple linear relationship:

$$\frac{\Delta R_\mu}{\langle R_\mu \rangle} = \alpha_T \frac{\Delta T_{eff}}{\langle T_{eff} \rangle} \tag{5.9}$$

where T_{eff} is the effective atmospheric temperature, ΔT_{eff} and ΔR_μ are the deviation from mean, $\langle R_\mu \rangle$ and $\langle T_{eff} \rangle$ are the respective averages and α_T is the effective temperature coefficient [173], or the $\frac{K}{\pi}$ production ratio [182]. As the temperature increases, the average atmospheric density decreases, increasing the mean free path of the kaons and pions, resulting in a lower probability

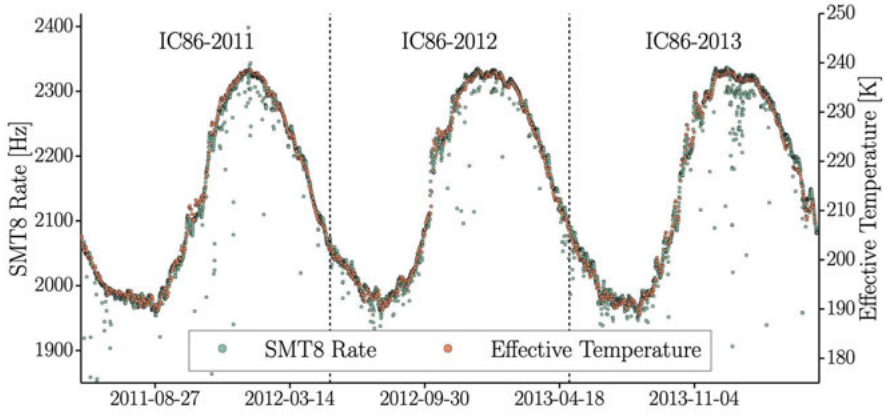

Figure 5.18. SMT8 trigger rate as a function of the effective atmospheric temperature for 2011-2013. We can see the clear correlation between both quantities. Reproduced from [177].

of interacting with air molecules. This lower probability of interaction has the effect that the kaons and pions decay more frequently, increasing muon production [181].

The temperature variability and intrinsic variations in air showers, coupled with the large time-integration of the MeV analysis, means that the atmospheric muons can mimic the MeV transient signal, resulting in more false positive alerts. If we take as an average the rate of 16 Hz per DOM for atmospheric muons, we can see that for the large time windows of the analysis, anywhere from O(10^5-10^7) muons will pass through the detector in that time frame, highlighting how this would produce a high background floor. Roughly half of the hits in the detector produced by atmospheric muons can be subtracted from the total noise rate by identifying triggering muons in the standard data stream [176].

Muon-Correction

Since we know that these muons produce DOM-to-DOM correlations, we could correct for this using DOM correlation coefficients. However, this task is computationally impossible, as one must compute a 5160x5160 matrix in real-time [179]. Therefore, an alternative method is needed, which is much faster and more efficient. Since we know that most HE muons will produce an SMT8 trigger and that they widen the significance distribution (see Fig. 5.17), we can fit a linear function between the estimate of the muon hit rate and the significance ξ, to produce a muon-corrected test statistic. In this subsection, we will cover how this correction is done online.

Online Muon-Correction

SNDAQ queries the pDAQ system for the muon hit rate proxy, which is the time-integrated HLC hits within an SMT8 trigger window [179, 177, 175], which we will call R_μ. The SMT8 rate can be affected by dropped DOMs or removed strings in a run [7] or instabilities in the DOMs [175]. In order to increase the robustness of the method and handle outliers that can occur, such as too low SMT8 rate, an SMT8 rate limit $R_{\mu_{threshold}}$ is introduced:

$$R_{\mu_{threshold}} = median(R_\mu) - 3 \cdot mad(R_\mu) \tag{5.10}$$

where the absolute median derivative is:

$$mad(R_\mu) = median(|R_{\mu_i} - median(R_\mu|) \tag{5.11}$$

where R_μ are all the rates obtained for a given run, and R_{μ_i} is the individual rate. The median and median absolute derivative (MAD) are used instead of an arithmetic mean and σ since they are less sensitive to outliers and heavy tails [175]. In addition to this, SNDAQ has a cut on $\xi \leq -10$ to prevent these extreme negative values from entering the calculation [175].

This SMT8 rate R_μ is time-integrated at the same t_0 as the running analysis window, producing an R_μ for each time-window. Then, a linear fit is made for ξ and R_μ for each time window, producing the coefficients needed for a decorrelation:

$$\xi_{corr_i} = \xi_i - b \cdot R_{\mu_i} - a \quad \text{for} \quad i \in I_{\text{valid}} \tag{5.12}$$

where

$$I_{\text{valid}} = \{i \mid \xi_i > R_{\mu_{threshold}} \text{ and } R_{\mu_i} > R_{\mu_{threshold}}\} \tag{5.13}$$

and a and b are the offset and slope obtained from the linear fit. For more details on how this is done, refer to [174]. Although this muon-correction will produce a significance distribution that is close to a Poissonian expectation of $\sigma = 1$, it will not reach unity, as the SMT8 has an energy threshold of about 550 GeV [177], there are still afterpulses and undetected lower energy atmospheric muons that produce SLC hits, affecting the width by several percent [179, 177]. Multiple studies were performed on alternative triggers for muon-rate proxies, such as lowering the SMT multiplicity and volume trigger. However, this did not improve the online muon correction [177].

Offline, however, we can utilize a different data stream to circumvent this issue and access smaller bin sizes. Since SNDAQ can only access 2ms bins, it can restrict the potential physics that can be extracted from the light curve. To

[7] Run, in this context, refers to how data is handled and processed at the pole, with typical runs being 8 hrs long

access a finer time bin resolution, if a candidate supernova event surpasses a pre-determined significance threshold, a HitSpool request is issued, where the raw hits can be accessed for further analysis.

HitSpool for CCSNe

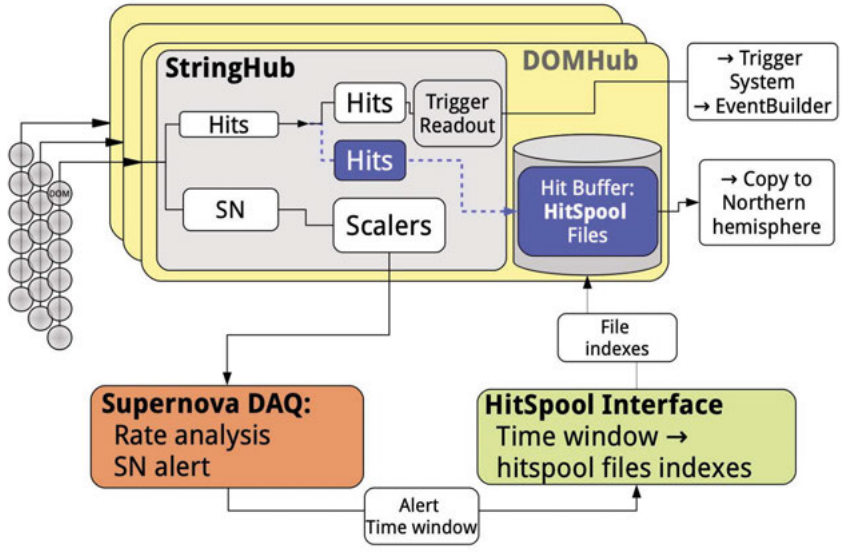

Figure 5.19. The data flow for the supernova analysis stream in IceCube. Reproduced from [172].

The data stream introduced in Section 5.2 relies on triggers with coincidence searches and filters applied to the payload to reduce the data size to be transferred to the North. However, the complete detector information, DOM hit payloads, is buffered locally on disk for up to two weeks, constituting the HitSpool data stream. This data stream provides an invaluable tool since we can have access to the unfiltered waveforms for each hit for each DOM to perform physics analyses that benefit from not applying the online filters and triggers, such as sub-threshold event searches like low-energy neutrino searches. On average, this stream accumulates around 70 MB/s compressed or over 200 MB/s uncompressed. This data stream is used for calibration, monitoring, and analysis streams such as supernova detection. In the context of MeV neutrinos, this raw hit stream is exploited so that the supernova stream can gain as much information as possible in the event of a CCSN. If SNDAQ computes an event significance of $\xi \geq 8.40$ or $\xi \geq 4.00$ and $\xi' \geq 5.80$ [8], the system issues a HitSpool request, pulling data with $t_{min} = 30$ s and $t_{max} = 60$ s around the

[8]These have been set in order to minimize the false triggers due to seasonal variation

trigger time t_0, where $t_{min,max}$ are the safety margins before and after trigger to not miss any critical signal [172]. If the significance exceeds $\xi \geq 10$, a data request of $t_{min} = 250$ s and $t_{min} = 250$ s is issued. This requested data is then sent to North for offline analysis.

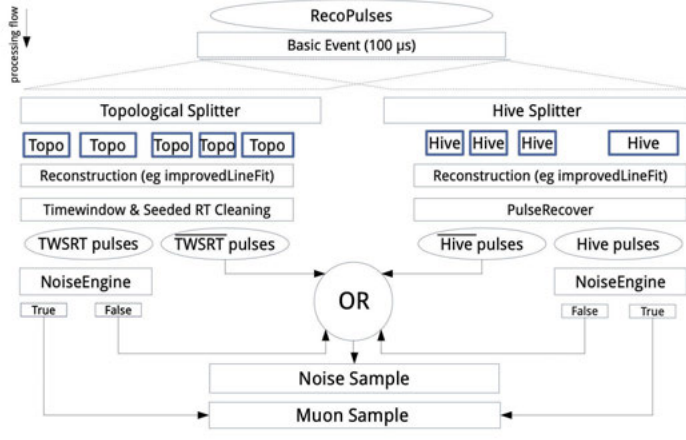

Figure 5.20. The different filters to identify low-energy muons for the supernova HitSpool offline analysis, starting the flow from the top to bottom. Reproduced from [172].

The raw hits are first converted into events of pre-determined bin size since these are un-triggered, unlike the other data streams. From there, the events are fed into two filters, *TopologicalSplitter*, and *HiveSplitter* (fig. 5.20), which aim to identify low-energy muons (subthreshold muons) that contribute to the noise and cannot be removed with the usual muon-correction, with a nanosecond resolution. The result is a dataset with all hits corresponding to the Poissonian part of the noise on the detector. Then, these are converted to a scaler data format. However, a 1 ms resolution is now used to re-bin in 2 ms, 500 ms, 1.5 s, 4 s, and 10 s for the different physics motivations, with the corresponding significances and light curves computed. The result is a cleaner dataset with a 3% decrease in the distribution width [172] and a finer lightcurve bin. Although this data can enable better resolution and cleaner detector hits, due to the bandwidth limitations and extreme computational resources needed to perform an analysis, it is limited to a handful of SNDAQ alerts per year.

ASTERIA

Although IceCube has yet to observe CCSNe or any other transient that can produce an MeV burst, the expected signal can be obtained with A Supernova Test Routine for IceCube Analysis (ASTERIA) [184]. ASTERIA is a fast Monte Carlo (MC) neutrino simulation designed to model the detector response for IceCube. IceCube's sensitivity can then be characterized using this

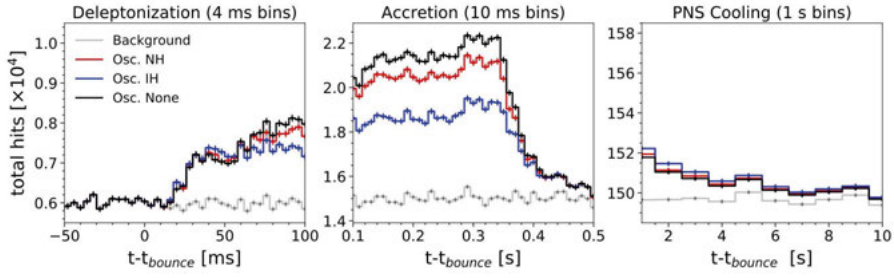

Figure 5.21. Simulated signal observable by IceCube using the scaler stream, for a 13 $M_\odot$ star at a distance of 10 kpc. Left panel shows the post-bounce burst, the middle panel shows the shock stagnation and heating and the right panel shows the PNS cooling. Reproduced from [183].

simulation chain, providing sensitivities to any MeV neutrino transients, such as CCSNe or GRBs. This simulation chain has produced signal expectations like in [180]. In Fig. 5.21 and 5.22, we can see what the resulting signal and sensitivity would look like in IceCube. To have access to shorter timescale phenomena such as standing accretion shock instabilities, the HitSpool stream could be utilized since its only limiting factor is the DOM internal time resolution of 0.1 ns [172]. Although Icecube is not sensitive to ν_e, it has one of the best sensitivities to the $\bar{\nu}_e$ neutrino burst with excellent timing information for a Galactic CCSN, with a detection horizon of MeV bursts at approximately 50 kpc (or LMC) for 5.7σ, or to the SMC with 3σ (see Fig. 5.22) [10].

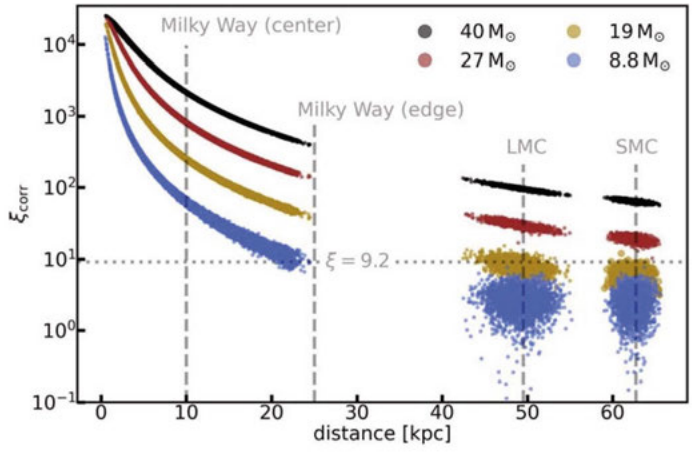

Figure 5.22. IceCube MeV CCSNe detection horizon for 4 different star masses. The y-axis represents the muon-corrected significance, and on the x-axis the distance. Reproduced from [180]

6. Search Strategies for MeV and GeV-TeV Neutrinos

> The cosmos is also within us, we're made of star-stuff. We are a way for the cosmos to know itself.
>
> *Carl Sagan in Cosmos, 1980*

After covering the background necessary to understand the analyses, including neutrino production in the death of stars in Chapter 3 and how we can observe these neutrinos in IceCube in Chapter 5, we can discuss the analyses. In this chapter, we will cover the different analyses done to search for neutrinos from GRBs, neutron star mergers, and CCSNe, employing different strategies for the lowest energies (MeV) and high-energies (>GeV).

For analyses 6.1-6.4, which are IceCube analyses, we have to follow the *blindness* concept, which requires developing the analysis on background data and simulations. This procedure ensures that there is no intentional or unintentional enhancement of the signal by different selection criteria or methodologies. In these analyses, we split the data into off-time and on-time. Off-time represents any time we would not expect a signal from the source we base our analysis around, and on-time represents when we would expect the signal. The background is taken from off-time data, and different tests and checks are done on that sample to ensure the analysis is working as expected. The on-time sample is analyzed once these tests and checks have been performed and the analysis is mature. These analyses are based on a frequentist approach, where pseudo-experiments (background trials or TS distributions) on off-time data are used to determine the test statistic distributions that are used to determine the statistical significance of the on-time analysis. Therefore, these analyses use a data-driven approach, using the data to describe our background, which means we can remove some uncertainties from mismodeling the detector. The analysis in section 6.5 was performed using published IceCube data; therefore, the concept of blindness does not apply.

6.1 GRB 221009A: Search for MeV Neutrinos

On the 9th of October 2022 at t_0 =13:16:59 UTC, Fermi-LAT observed an extremely bright GRB at a distance of about 740 Mpc ($z = 0.151$) [185, 186].

Figure 6.1. Afterglow from GRB 220109A as captured by NASA/ESA Hubble Space Telescope, circled in red. *Image credit: NASA, ESA, CSA, STScI, A. Levan (Radboud University); Image Processing: Gladys Kober*

This emission had a precursor emission starting at t_0 with a duration of about 17 s, followed by a main long-duration episode starting at about $t_0 + 175s$ and lasting ≈460 s (see Fig. 6.2). Following this, several other gamma-ray detectors confirmed the observation, such as Swift Observatory [187] and Large High Altitude Air Shower Observatory (LHAASO) observing TeV gamma-rays [188]. The multitude of gamma-ray observations at the highest energies ever recorded for a GRB earned the nickname for this source as the brightest of all time (BOAT) [189]. In addition to gamma-rays, optical observations revealed a potential emerging supernova spectrum in the afterglow, potentially classified as a Type Ic [185] SN. In addition to EM observations, an IceCube analysis searching for neutrinos from this GRB, spanning from MeV to PeV energies, was performed for this source. In this section, we will describe the search of MeV neutrinos for GRB 221009A.

6.1.1 Motivation

As covered in Section 3.3, there are several theories regarding the origin of a GRB, which also affects when we expect to observe a MeV neutrino signal relative to the gamma-ray light curve. For example, if a fallback collapsar is the origin of the GRB, we may have a PNS soft jet breaking out before it collapses into a BH. After the collapse, ultra-relativistic jets and a large accretion disk (NDAF) form. In this instance, the soft jet would produce a precursor emission followed by the prompt emission due to the ultra-relativistic jets [127, 128]. Even though the jet system might inject constant properties, there can be a dead time between the different phases due to viewing angle effects. This dead time arises due to the jet having different phases in its evolution,

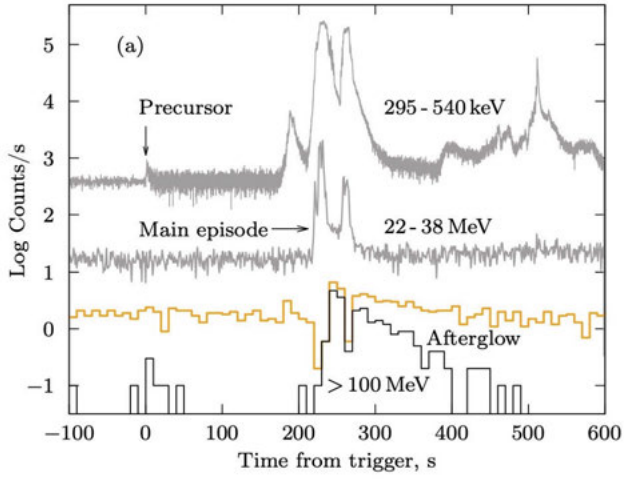

Figure 6.2. Lightcurve for GRB 221009A in different energy ranges, with upper and middle curves for GBM photons, with the orange curve for all LAT photons and the lowest curve for LAT photons circled around 8°. Note that the dip is around 200 s due to the detector saturation. Reproduced from [190]

where some phases can have larger opening angles than others, for example, the precursor phase, where the jet does not fully pierce through the star but pushes the cocoon of material, released as a wide-angle outflow, followed by a more collimated shocked-jet outflow, with opening angle increasing slowly with time [191].

In addition to this, if the progenitor was a CCSNe, the SBO photons (UV-to-soft X-ray) could get boosted to hard X-ray or gamma-rays by scattering in the ejecta or shocked plasma, or in the dense, thick wind [192], or in the jets [193], which can affect the energy of photon emission [192, 194, 195], resulting in some of the SBO component to be visible as hard x-ray to gamma-ray [139, 196, 192]. Therefore, there are significant uncertainties on when to expect these MeV neutrinos, and they could arrive anywhere from before the precursor emission if the progenitor was a CCSNe to the end of the prompt emission.

6.1.2 Analysis Methodology

We first defined our six search windows, as can be seen in Fig. 6.3 and in Table. 6.1 covering different physics motivations.

Since this analysis is designed to search for MeV neutrinos, we used the 500 ms data produced by SNDAQ. This data consists of the hit rates in each DOM. We summed all the DOM rates for one bin i to obtain:

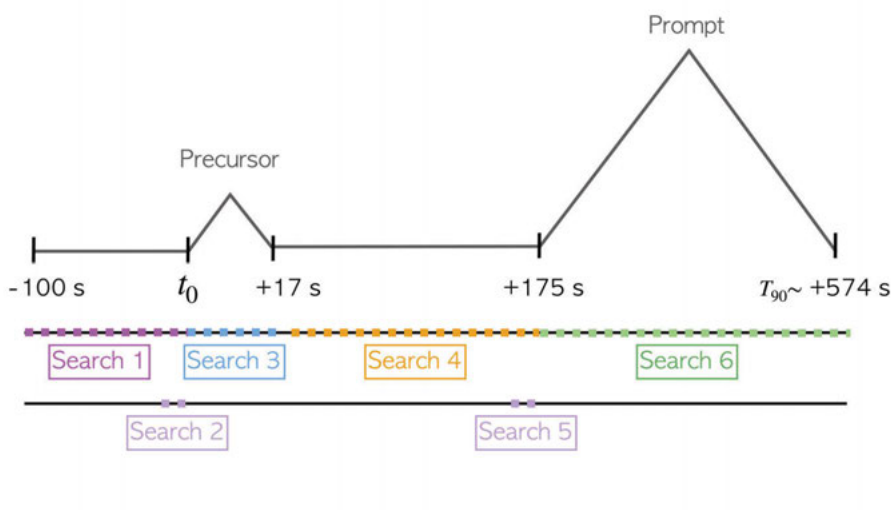

Figure 6.3. A schematic of the gamma-ray lightcurve shown in grey, with the different search windows.

Search	Search Window	Bin Size	Total Duration
1	[t_0-100s, t_0]	1 s	100 s
2	[t_0-1s, t_0]	0.5 s	1 s
3	[t_0, t_0+17s]	1 s	17 s
4	[t_0+18s, t_0+174s]	1 s	156 s
5	[t_0+174s, t_0+175 s]	0.5 s	1 s
6	[t_0+175s, t_0+547s]	1 s	372 s

Table 6.1. *The different search windows for the MeV neutrino analysis of GRB 221009A.*

$$R_{tot}(i) = \sum_{i=0}^{N_{DOMs}} R(i) \tag{6.1}$$

We then use a sliding sum over either one bin (for 0.5 s searches) or two bins (for 1 s searches), scanning through the total duration of the search (e.g., 100s), and we pick the largest sum $R_{\rm tot}^{\rm max}$:

$$R_{\rm tot}^{\rm max} = \max_{0\leq i\leq L-k} \left(\sum_{j=0}^{k-1} R_{\rm tot}(i+j) \right) \tag{6.2}$$

where k is the number of bins (1 or 2), and L is the number of bins in the search window. The largest rate $R_{\rm tot}^{\rm max}$ is then our test statistics (TS).

Background Trials

We then characterize the background through trials on off-time data. We selected ± 7 days worth of SN data, for a total of 14 days, centered around t_0, but excluding the day of the GRB observation. We performed many realizations of our TS for each search window on this off-time data. We produced $10^4 - 10^5$ trials for the search windows with bin size of 1 s and 10^6 trials for the search windows with bin size 0.5 s. An example of what these look like can be seen in Fig. 6.4.

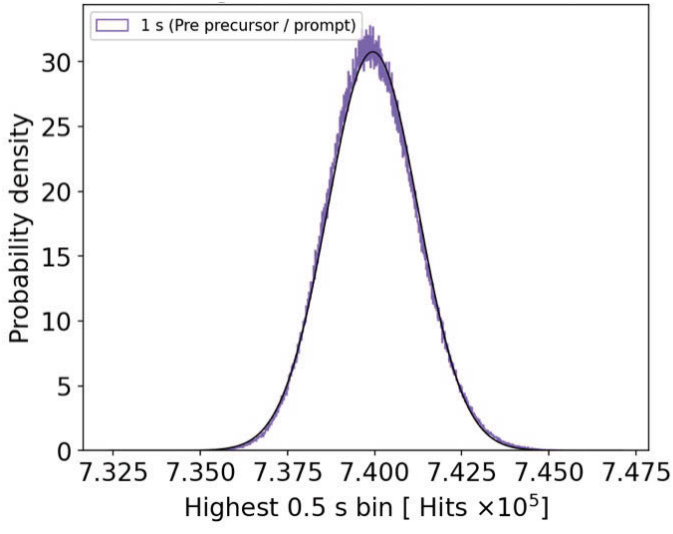

Figure 6.4. TS Distributions for GRB 221009A analysis for the 1 s search windows. The y-axis represents the density and the x-axis represents the $R_{\text{tot}}^{\text{max}}$. A Gaussian fit is overlaid on top of the distribution, highlighting the distributions' near-Gaussian shape.

On-Time Observation

We performed the search on on-time data, obtaining one $R_{\text{tot}}^{\text{max}}$ for each search. To determine the significance, we used the TS distributions. As shown in Fig. 6.5 for the 1 s bin size searches and in Fig. 6.6 for the 0.5 s bin size, the observation is consistent with the background expectation, with p-values > 0.3.

Upper Limit Calculation

The upper limit (U.L.) on the observed hits is obtained using the Feldman-Cousins (F.C.) method [197] for a 90% confidence level (C.L.). The total 90% C.L. U.L. excess of hits in the search bin is $R_{exc}^{90} = \mu_{90} - \mu$, where μ is the mean from the distribution and μ^{90} is the F.C. upper limit given an observation $R_{\text{tot}}^{\text{max}}$. In order to determine the U.L. on the luminosity, we can start with eq. 5.3, summing over all DOMs and integrating in time, and using the U.L. on the excess of hits to obtain the total U.L. on luminosity:

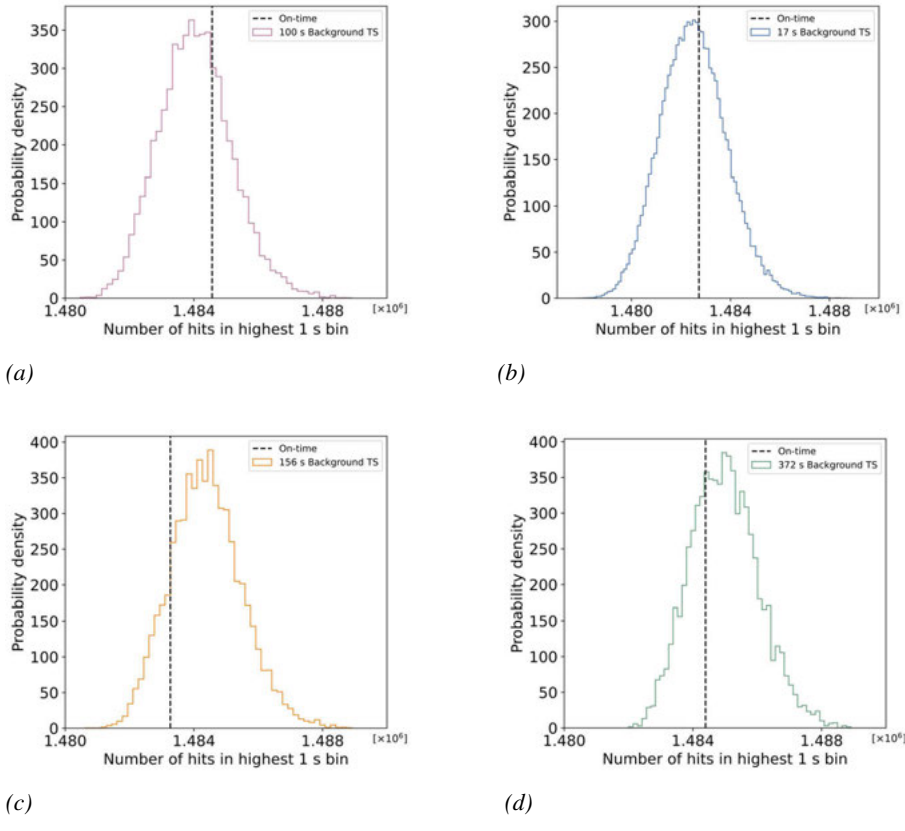

Figure 6.5. Results for the search for MeV Neutrinos from GRB 221009A for the search windows with a bin size of 1 s, with the y-axis representing the density and the x-axis representing the maximum summed hits in the sliding window search or $R_{\text{tot}}^{\text{max}}$ for the 1 s bin size. The black dashed line represents the $R_{\text{tot}}^{\text{max}}$ during the on-time observation.

$$L_{\bar{\nu}_e}^{90} = \frac{R_{exc}^{90}}{\varepsilon_{deadT} n_{ice} \int_0^\infty dE_e \frac{d\sigma}{dE_e}(E_\nu, E_e) V_{eff}^{e^\pm}(E_e)} \cdot \frac{4\pi d^2 \langle E_\nu \rangle}{\int_0^\infty dE_\nu f(E_\nu, \langle E_\nu \rangle, \alpha)} [MeV], \tag{6.3}$$

where ε_{deadT} is the efficiency factor of the DOM, n_{ice} is the density of targets in ice, E_e is the lepton energy, $\frac{d\sigma}{dE_e}(E_\nu, E_e)$ is the differential cross-section for the interaction of interest, $V_{eff}^{e^\pm}(E_e)$ is the effective volume for a single photon in the detector, d is the distance from source, $\langle E_\nu \rangle(t)$ is the mean energy and $f(E_\nu, \langle E_\nu \rangle(t), \alpha(t))$ is the energy pdf, where α is the pinch parameter which determines width of the neutrino energy spectrum. In the case of this analysis, we assumed the generic blackbody spectrum that follows a Gamma distribution with $E_{\bar{\nu}_e}^- = 15$ MeV and $E^{rms} = 17.32$ MeV and $\alpha = 2$. To find the luminosity U.L. (eq. 6.3), we make use of the fast open-source ASTE-

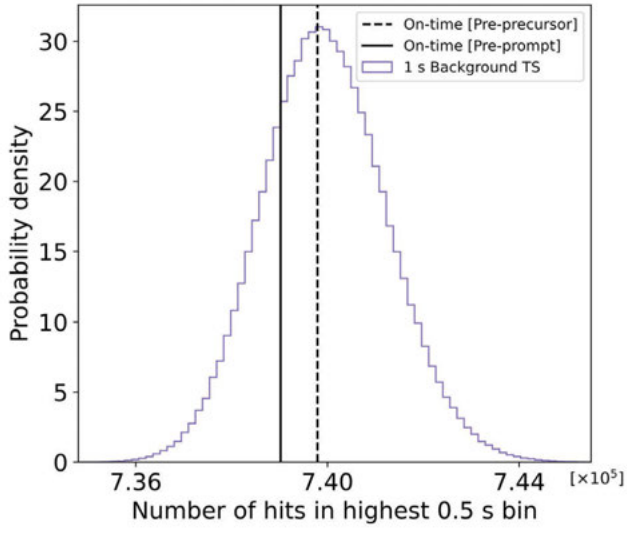

Figure 6.6. Results for the search for MeV Neutrinos from GRB 221009A for the search windows with a bin size of 0.5 s, with the y-axis representing the density and the x-axis representing the maximum summed hits in the sliding window search or $R_{\text{tot}}^{\text{max}}$ for the 0.5 s bin size. The black dashed line represents the $R_{\text{tot}}^{\text{max}}$ during the on-time observation for search window.

RIA code (as mentioned in Section 5.4), which is a Monte Carlo code that estimates the total count rate in all DOMs, weighted by the DOM efficiency ε_i, and then the simulated signal counts are injected on top of background simulation. In this simulation chain, we can select the neutrino fluence with parameters such as time, total luminosity, neutrino flavor, E_{rms}, and α. It then produces with those quantities a neutrino flux and energy pdf, which is convoluted with detector parametrizations and interactions, to produce a signal hit rate that matches R_{exc}^{90}. To obtain the U.L. on neutrino flux, we can then use the luminosity that produced our R_{exc}^{90}, or eq. 6.3:

$$\Phi_{\bar{\nu}_e}^{90} \approx \frac{L_{\bar{\nu}_e}^{90}}{\langle E_{\nu_e} \rangle 4\pi d^2}. \tag{6.4}$$

6.1.3 Discussion

We have presented the motivation and methodology for the work shown in **Paper I**. Since the results were consistent with background expectation, we placed U.L. on the individual search windows (See Fig. 6.7 for the $\bar{\nu}_e$ neutrino flux and bolometric luminosity (See Table.6.2). Neutrinos from GRBs, specifically NDAF [138, 127], can be detected at various stages, from before the prompt up until the prompt phase. The diverse processes that give rise to these neutrinos make them an exciting messenger for probing GRBs' deeper

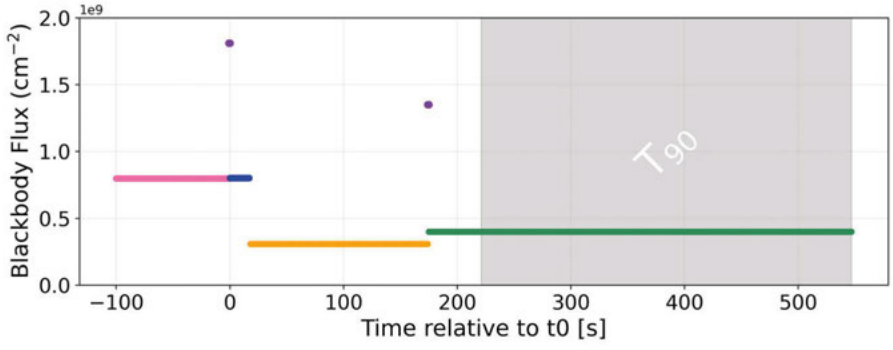

Figure 6.7. MeV U.L. on an electron antineutrino blackbody flux $F(E) \approx E_\nu^2 exp(-3E_\nu / < E_\nu >)$ [198] as a function of time window. Because this analysis focuses on much shorter timescales than many other analyses, a linear x-axis is needed here. The T90 for the GRB is highlighted with the grey band. Because the MeV analysis has large background rates, the value does not scale simply with a time window. In pink, we see the limit for search 1, in purple for searches 2 and 5, in blue for search 3, in orange for each 4, and in green for search 6.

and denser regions [131, 127]. Unlike HE neutrinos or EM emissions, thermal neutrinos would allow us to look into the inner regions of a GRB, allowing us to explore interesting parameters such as the accretion rate or the black hole spin [131].

As we can see from Table. 6.2, the total luminosity required for us to observe it from a distance of 740 Mpc is 5-7 orders of magnitude more than what current simulations predict (See Section 3.3). The non-observation of MeV neutrinos could be due to this particular GRB not producing sufficient thermal neutrinos to be detectable or due to the distance to the source. However, although we did not observe neutrinos, this was the first search for MeV neutrinos from a GRB spanning this large energy range in IceCube. The advantage of using the IceCube data is the extremely high duty cycle of the detector, with an SN data live time exceeding 99.7% per year and excellent stability. The result is that IceCube is likely to be very stable during most astrophysical transients of interest.

6.2 Model-Independent MeV Neutrino Upper Limits

6.2.1 Motivation

Using the assumption of a generic blackbody spectrum with a Gamma distribution with $E_{\bar{\nu}_e} = 15$ MeV and $E^{rms} = 17.32$ and $\alpha = 2$ is a good first approximation to set U.L. and it had been previously used by another IceCube analysis, that of the search of MeV neutrinos from Fast Radio Bursts (FRBs)

Time window	$\Phi^{90}_{\bar{\nu}_e}$ [neutrinos/m^2]	$L^{90}_{\bar{\nu}_e}$[erg]
1	$7.98 \cdot 10^{12}$	$6.95 \cdot 10^{59}$
2	$1.81 \cdot 10^{13}$	$1.57 \cdot 10^{60}$
3	$8.00 \cdot 10^{12}$	$6.97 \cdot 10^{59}$
4	$3.08 \cdot 10^{12}$	$2.68 \cdot 10^{59}$
5	$1.35 \cdot 10^{13}$	$1.17 \cdot 10^{60}$
6	$4.00 \cdot 10^{12}$	$3.49 \cdot 10^{59}$

Table 6.2. *The upper limits for each search window for GRB 221009A, showing two quantities: the time integrated flux and the total luminosity.*

[199, 200]. However, this approach does carry the limitation that it assumes a thermal spectrum with certain parameters, which can be restrictive. Since there are many neutrino emission models from GRBs, an alternate method for producing U.L. was needed.

6.2.2 Analysis Methodology

We can adopt a model-independent approach for this methodology as described in [201, 202]. This approach allows the broader scientific community to test and validate theoretical models using IceCube data. Instead of using the average mean energy and a pinch factor to inform our neutrino energy distribution, we can use a Dirac-delta function, where all the luminosity and neutrinos are assumed to be of a single energy. Starting from the energy pdf, we can replace it with Green's function $\delta(E_\nu - E'_\nu)$, which means that the function is zero everywhere else but at E'_ν, we first begin by approximating our energy function:

$$f(E_\nu, \langle E_\nu \rangle, \alpha) = \delta(E_\nu - \langle E_\nu \rangle) \tag{6.5}$$

which then can be substituted into eq. 6.3, and expressing for the appropriate energy, we obtain the Green's function time-integrated U.L. neutrino flux, that is expressed as a function of a single energy:

$$\Phi^{90}_{\bar{\nu}_e}(\langle E_\nu \rangle) = \frac{R^{90}_{exc}}{\varepsilon_{deadT} n_{ice} \int_0^\infty dE_e \frac{d\sigma}{dE_e}(\langle E_\nu \rangle, E_e) V^{e^\pm}_{eff}(E_e) \int_0^\infty d\langle E_\nu \rangle \delta(E_\nu - \langle E_\nu \rangle)} \tag{6.6}$$

We use the same methodology as in section 6.1, where we input the mono-energetic luminosity into ASTERIA to obtain the final U.L. on the flux for $E_{\bar{\nu}_e}$ energies between 1 and 100 MeV, in steps of 1 MeV.

6.2.3 Discussion

We have presented the motivation and methodology for the work shown in **Paper II**. With this methodology, we can obtain model-independent MeV neutrino U.L. and sensitivities for IceCube. We obtained the model-independent U.L. on the $E_{\bar{\nu}_e}$ flux for each of the six search windows for GRB 221009A. Even at the highest energies, with a U.L. of O($10^{11} m^{-2}$), the corresponding bolometric luminosity would be around 10^{58} erg, which is significantly higher than what is expected for this sources. However, with this method, depending on the neutrino energy, we can improve the U.L. by up to 1 order of magnitude.

6.3 Fast Response Analysis: MeV Neutrinos Correlated with GW Alerts

6.3.1 Motivation

When the GCN circular [1] for GRB 221009A was sent, and IceCube could perform a fast-response follow-up analysis using high-energy neutrinos. However, in the MeV range, there was no such feature. This lack of capability to access the real-time stream in MeV posed a problem since an offline analysis typically relies on data arriving at North, which can have a latency of 8-24 hrs. For interesting and critical astronomical events, it is imperative to be able to perform a fast follow-up of the external alert. As covered in Section 5.4, SNDAQ is the system that monitors the detector rate in real-time to search for bursts of MeV neutrinos, predominantly from CCSNe. However, this system currently does not allow real-time searches using information from an external alert, missing the opportunity to follow up on interesting astrophysical events. This feature would be necessary not only in case of events like GRBs but also for potential CCSNe detected with GW, such as the alert sent on 2020-01-14 02:12:26 UTC by LIGO/Virgo named S200114f [203], which was classified as an *unmodeled burst* [2]. CCSNe could produce complex short GW signals, lasting O(1 s) [204] that can be mistaken as glitches, which is why LVK has a separate filter that looks for these unmodeled bursts. At the time of this event, it was impossible to respond using real-time data despite IceCube having the dedicated supernova monitoring system SNDAQ.

The goal of this project was to create functionality for SNDAQ that allows triggering analysis in real-time at the South Pole, using external information, such as a GCN circular, and reporting back to the North with the analysis results, such as the muon-corrected significance and the lightcurve. The scientific advantage of this fast response is that it allows access to live SN data.

[1] A GCN circular is a rapid astronomical bulletin used by the community worldwide to alert of important discoveries or results. `https://gcn.nasa.gov/circulars`

[2] It was retracted at a later time.

The first deployment instance will respond to alerts from LVK O4 run [3]. This run started on May 2023 and is expected to continue until June 2025, and currently only LIGO and Virgo detectors are functioning, with an uptime of about $\sim 75\%$ [205]. As we saw in Section 3.2, many models predict the emission of thermal MeV neutrinos from sources that also produce gravitational waves, from neutron star mergers like BNS and NSBH to CCSNe, with these thermal neutrinos appearing approximately at the same time as the GW. The expected burst of electron antineutrino would have a duration of a few milliseconds to several seconds. The luminosity from electron antineutrino would be $O(10^{52} - 10^{54})$ erg/s (see Fig. 6.8), with mean energies from 10-30 MeV depending on the model.

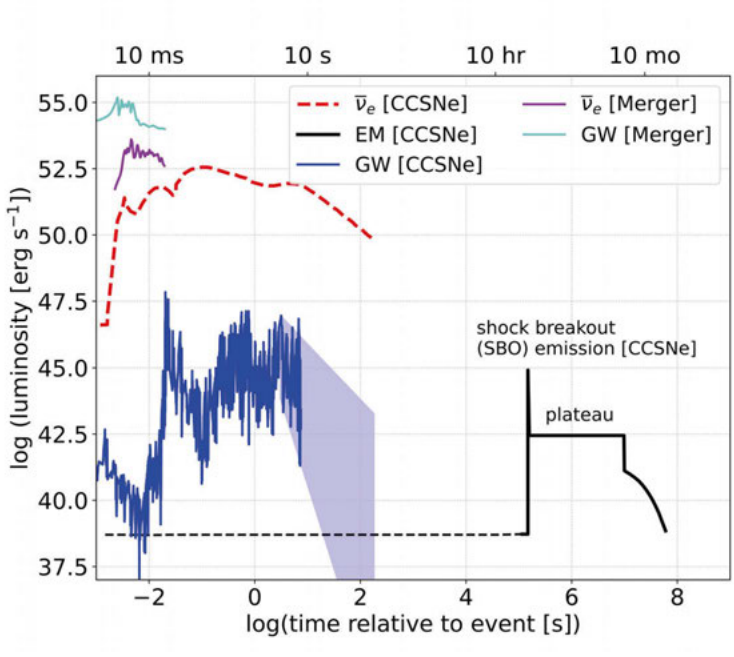

Figure 6.8. Expected log luminosities (y-axis) for gravitational waves (solid blue and turquoise), for $\bar{\nu}_e$ (dashed red, solid magenta) and EM emission from CCSNe (black solid). The x-axis shows the time relative to the event, which is the core bounce for CCSNe and the merger time for the NS merger. Adapted from [119, 48].

Gravitational Wave Alerts

Since we are interested in following-up sources that could potentially produce MeV neutrinos, we set the criteria to follow up alerts that either could potentially be a CCSN, or *Burst* in the GW alert type, and BNS/NSBH from the *CBC* pipeline (See Fig. 6.9). However, the CBC also contains Binary

[3] In the context of LVK, run denotes an observation period during which the detector is taking data.

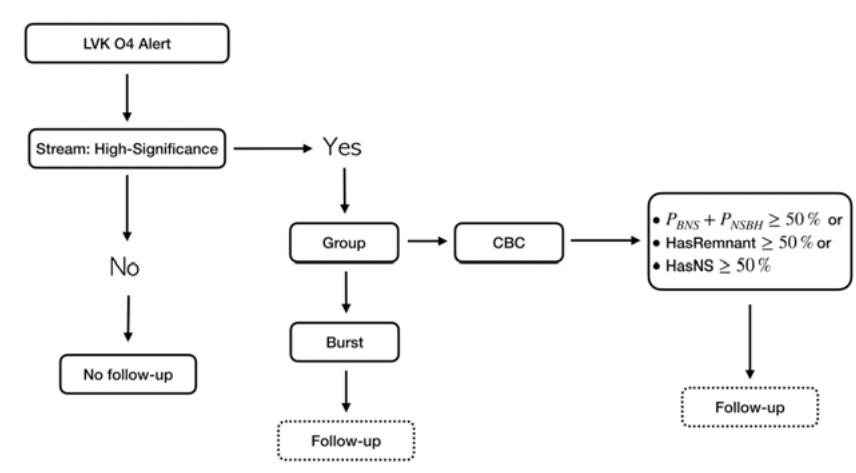

Figure 6.9. Schematic of the MeV neutrino follow-up for LVK O4 run. Where P_{BNS} is the probability of the alert being a BNS, P_{NSBH} is the probability of the alert being a NSBH, HasRemnant is the probability that the system ejected a non-zero amount of NS matter and HasNS is the probability that one of the compact objects was a NS.

Black Hole (BBH), which we are not interested in following up, we select only the CBC alerts that have a probability of containing a neutron star. For both CBC and Burst, we only select those marked as high-significance, which have a false alarm rate of about $3.9 \cdot 10^{-7}$ Hz for CBC's (< 1 per month) and $3.2 \cdot 10^{-8}$ Hz for Bursts (< 1 per year) [206] [4].

6.3.2 Analysis Methodology

SNDAQ searches for MeV neutrinos in real-time, without any connection to external alerts, and currently, without the possibility of triggering it with an external alert. Therefore, a new implementation of SNDAQ had to be developed called PySNDAQ Fast Response (PySNDAQ FR) to be deployed parallel to SNDAQ at the pole. This new implementation of PySNDAQ would allow real-time data analysis using triggering information such as a t_0 and a search window. In addition to this PySNDAQ implementation, software that interfaced between the external messaging system, such as for GW alerts, PySNDAQ, and the analysis product had to be developed called MeV Fast Response Analysis Suite (MeVFRAS). Finally, a new API [5] that interfaced between PySNDAQ and this analysis was developed.

[4] This considerably reduces the follow-up to noise, where the rate for CBC's is about 8 per day and 4 per day for Bursts.

[5] API stands for Application Programming Interface or the component that helps to communicate with software.

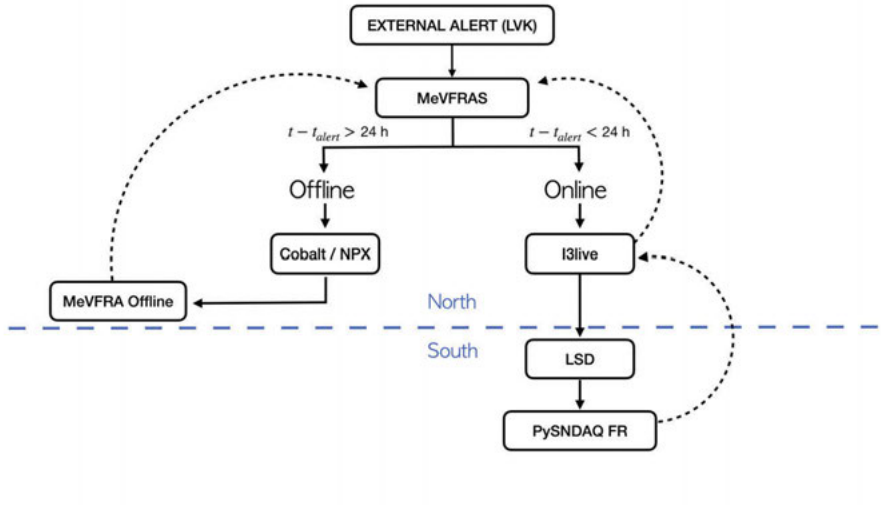

Figure 6.10. Technical schematic of the MeV Fast Response Analysis for the online and offline components. Note that the offline component is a future implementation that would allow follow-up alerts that might be sent out outside the 24-hour data buffer window at the South Pole. Cobalt/NPX are the computing resources at the University of Wisconsin-Madison used for IceCube analyses at North.

Pipeline	$p_{NS} \geq 0.5$	Search Windows
CBC	Yes	$[t_0, t_0$+0.5s$]$, $[t_0, t0$+1.5s$]$
Burst	-	$[t_0, t_0$+0.5s$]$, $[t_0, t0$+1.5s$]$

Table 6.3. *GW follow-up search windows for the different pipelines, where $p_{NS} \geq 0.5$ is the probability of the alert containing a neutron star, as given in the LVK alert.*

When MeVFRAS picks up an incoming GW alert (see Fig. 6.10), and if the criteria are met, a trigger timestamp, as well as the source class (*NS merger* for CBC's alerts or *CCSNe* for Burst alerts), is forwarded to PySNDAQ FR via the i3live system' [6] API. This i3live API forwards the message to the pole via satellite, which is then received by a listener and forwarded to PySNDAQ FR. From there, PySNDAQ FR will retrieve the necessary data that is buffered short term ($\sim$ 24 hrs). It will then perform the analysis described in Chapter 5.4 for different search windows. This analysis uses two search windows: 0.5 s and 1.5 s (see Table. 6.3), sufficient for the short emission windows predicted for BNS/NSBH.

TS Distributions

To determine the significance of the alert that we follow up on, we obtain the TS distributions for 1.5 s (see Fig. 6.11). Since we know that the width of the

[6] i3live is part of the system that is responsible for controlling, monitoring and data movement of the experiment. See Section 5.2

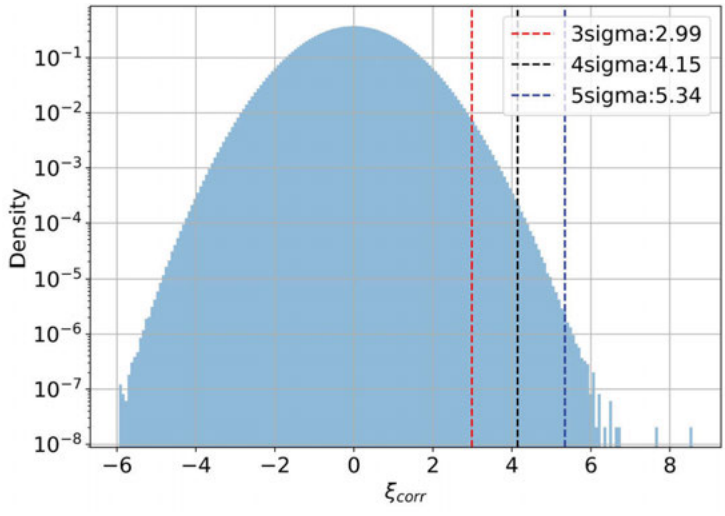

Figure 6.11. ξ_{corr} TS distribution obtained offline, obtained by running SNDAQ-type analysis on 12 years of archival SN data and DST data for the muon rate proxy, with the difference significances highlighted in the dashed lines. From [180].

distribution increases as the search window increases (see Fig. 6.12), to not overestimate our significance, we chose to limit the search windows to 0.5 s and 1.5 s. The difference in the muon-corrected width between 0.5 s and 1.5 s is not drastic, with an expected width of about 1.08σ for the 0.5 s and the 1.1σ for the 1.5 s, resulting in about 3-4% difference underestimate for the 0.5 s search. The final output of this analysis for each search window is the test statistics ξ and ξ_{corr}, the light curves, and the p-values. A planned GCN follow-up report might be sent for BNS/NSBH if the p-value $\leq 1\%$ or if the GW alert was a burst. The latency of the online MeV FRA chain is in the O(≤ 10) min, a notable improvement from waiting until SN data is shipped to North (8-24 hrs) or even performing an analysis using HitSpool, which can take from query to final analysis 72 hrs.

6.3.3 Discussion

We have presented the new MeV neutrino follow-up pipeline for IceCube, as shown in **Paper III**. Although the IceCube collaboration has approved this analysis, there has been a delay in deploying PySNDAQ FR at the South Pole at the time of writing this thesis. However, it is expected that the deployment will take place very soon. Since there is still close to a year left of the LVK O4 run at the time of writing this thesis, we are hopeful that we will be able to follow up on some interesting alerts.

6.4 Catalog Search of MeV Neutrinos Correlated with Gravitational Waves

6.4.1 Motivation

Following the online analysis of GW alerts from LVK O4, a complementary search using past LVK alerts was performed. The advantage of performing an offline search compared to the online MeV FRA is the possibility of properly characterizing the background with large statistics, better background treatment, and population studies, such as a binomial test, where we can test if there is a sub-population in the catalog that are neutrino emitters.

6.4.2 Analysis Methodology

Since this analysis searches for MeV neutrinos, we used the 500 ms Supernova data (SN data) produced by SNDAQ and archived it at North for analysis. We define the start time of the search as t_0 and search in four time windows: 0.5 s, 1.5 s, 4 s, and 10 s.

LVK Catalogs

For our GW catalog, we used the GWTC-1 catalog for the O1 and O2 runs [207], GWTC-2.1 for the O3a [208] run, and GWTC-3 for the O3b run [209]. These catalogs have sources with a final $p_{astro} > 0.5$, which is the probability of the GW event being astrophysical in origin. There are 11 events in O1+O2 (2015-2017) and 79 in O3a+O3b (2019-2020). For the combined catalog of runs O1+O2+O3, there are 84 binary black hole mergers (BBH), 4 NSBH, and 2 BNS.

Background Trials

We define the off-time background as data corresponding to one day before the on-time alert and one day after, excluding any overlapping alerts, for 48 hours' worth of data. We then run the analysis on this data (eq. 5.6-5.8) for each search window, sliding r_i by $\Delta t = 500$ ms and computing a new ξ until the end of the run. We perform these background trials for each GW alert in the catalog for 344 distributions. The total statistics for each TS distribution is of $\sim 10^5$ samples. This background distribution can be seen in Fig. 6.12 for each of the four search windows for GW 170104. To ensure proper data quality both for our on-time and off-time data, we set the criteria of the runs[7] to use as:

- Detector status flagged as good.
- If detector status was flagged as failed, exclude those runs, and those after the run was restarted.
- Exclude runs that are too short (less than 2 hrs).

[7] Run is defined as a data taking period.

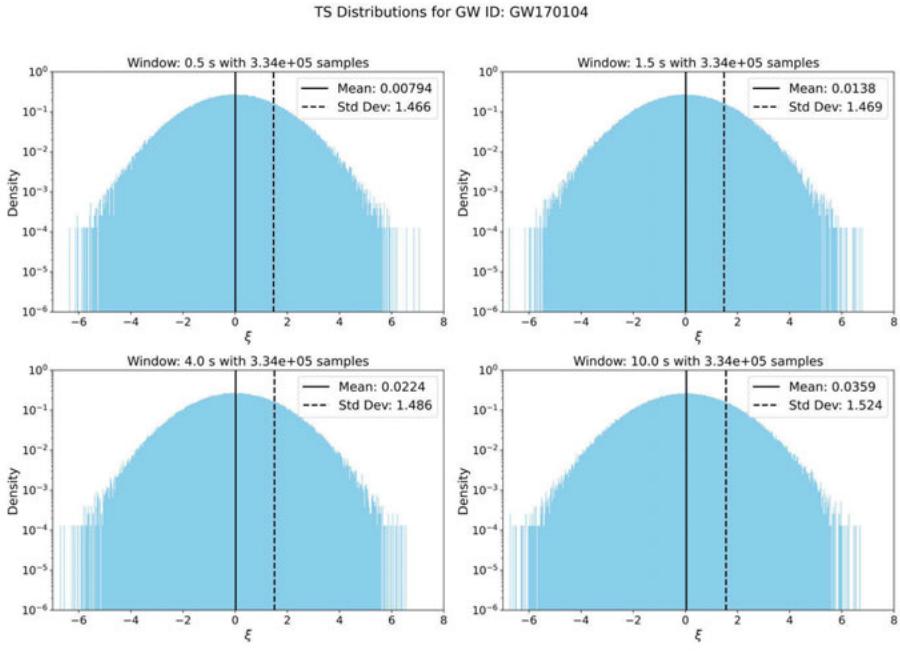

Figure 6.12. TS distribution of uncorrected significance ξ for GW alert GW170104 for each search window. The x-axis shows the log(density), the y-axis shows the uncorrected significance, and the solid/dashed line shows the μ_ξ and σ_ξ, respectively.

- SNDAQ monitoring quantities marked as good.
- No deviation in trigger rate greater than 10% than previous or subsequent runs.
- No other known issue in the data acquisition.

Based on that criteria, we exclude 4 GW alerts since their corresponding on-time run was flagged as bad, resulting in a final catalog of 80 BBH, 4 NSBH, and 2 BNS. The excluded GW alerts are, along with their event time t_{event}:

- GW170818 | t_{event} = 2017-08-18 02:25:09
- GW190527 | t_{event} = 2019-05-27 09:20:55
- GW190630 | t_{event} = 2019-06-30 18:52:05
- GW191216 | t_{event} = 2019-12-16 21:33:38

Offline Muon-Correction

From Fig. 6.12, we can see that although the distribution of ξ is close to a Gaussian with $\mu_\xi \approx 0$, the spread of the distribution is not close to unity, with $\sigma_\xi \approx 1.4$. In order to correct the widening of the distribution due to correlations caused by muons, we can apply an offline muon correction to the TS ξ as outlined in Section 5.4. The muon correction is done using DST data sent to

the North. This data records the results of a fast reconstruction implemented at the pole in the filtering scheme and collects muon track reconstruction results for each event, along with interesting observables like the number of hit DOMs, the even time, and some trigger information. We are interested in the SMT8 trigger rate at a certain time for muon correction since that can be used as a proxy for the muon rate. This method is a similar proxy to what SNDAQ obtains via the pDAQ [175, 177, 210], and was previously used in several IceCube analyses [180, 200].

Once we obtain our uncorrected TS values for each run, we can obtain the proxy for muon the muon rate binned in the same size as our TS $[t_\xi, t_\xi + \Delta t]$, where t_ξ is the start time of our TS and Δt is the search window where the analysis is performed. We have four (0.5, 1.5, 4, and 10 s) search windows in this case. This muon-rate estimate R_μ for each TS can be obtained by summing over all the DOMs in each event i, or $NChannel(i)$ that have had a trigger approximating SMT8:

$$R_\mu(\xi) = \sum_{i=t_\xi}^{t_\xi+\Delta t} NChannel(i). \tag{6.7}$$

We can then apply a linear regression on ξ and R_μ for the 48 hrs of background TS, as described in Section 5.4, to obtain the slope and offset. Then we perform the correction to each ξ

$$\xi_{corr} = \xi - (a * R_\mu + b), \tag{6.8}$$

The result is a distribution that is closer to a Gaussian, with $\mu_{\xi_{corr}} = 0$ and $\sigma_{\xi_{corr}} \approx 1.1$ (see Fig. 6.13). As mentioned in Section 5.4, it is not possible to entirely remove these correlations, as there are also low-energy muons passing through that are not triggering SMT8. In addition to this, due to the condensed nature of DST data, where it does not contain all muon-hits, especially those at the upper part of the detector, it will affect how well we can perform this correction [210].

Binomial Test

In addition to performing a search for the GW alerts, we can also apply a binomial test to identify if there is a sub-population that is a neutrino emitter or, in our case, that would produce an excess in the total detector rate. The result of this test is to obtain the number of sources that, when combined, produce the most significant statistical deviation from background. We begin by defining two sub-populations: one that does not have a NS (BBH) and one that does have a NS (BNS+NSBH). Taking the best p-values p_k for each individual GW source (k), we order them in ascending values. We can then calculate the binomial probability as follows:

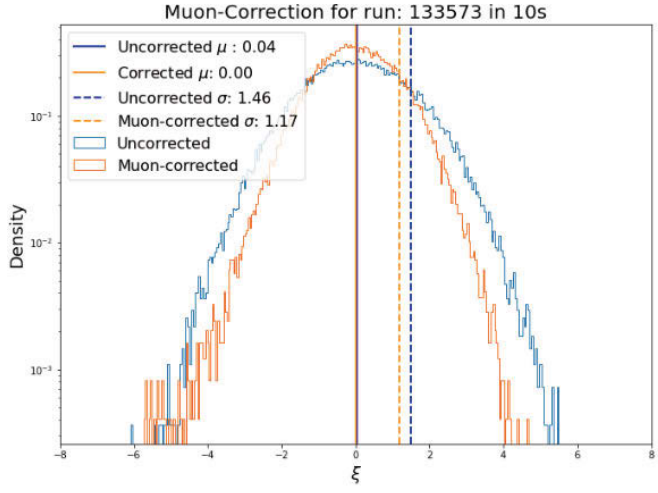

Figure 6.13. TS distribution of uncorrected significance ξ (blue) and muon-corrected significance ξ_{corr} (orange) for a 10 s search bin. In the solid/dashed line, we can see the μ_ξ and σ_ξ for each TS, respectively.

$$P(k) = \sum_{m=1}^{N} \frac{N!}{(N-m)m!} p_{k_{min}}^{m} (1 - p_{k_{min}})^{(N-m)}, \tag{6.9}$$

where N is the number of GW sources in our sub-population, scanning from m=1 to N sources. The result is N binomial p-values, interpreted as the probability that the first k-th sources are compatible with the background-only hypothesis. We then pick the best $P(k)$ or $P_{binom_{data}}$. Since we are selecting the lowest p_k from each time window for each GW source, and we are selecting the lowest $P(k)$ or $P_{binom_{data}}$, we are biasing our analysis. In order to take into account that bias, we repeat the same procedure on off-time background data, scrambling in time and picking from the same scrambled time the lowest p-value from all four search windows, performing the binomial test and obtaining a $P(k)$ (see Fig. 6.14 for an example). This process is repeated many times, obtaining a binomial background distribution P_{binom} for each sub-population (see Fig. 6.15 for an example). We can then use this distribution to correct for the bias and to obtain a final p-value:

$$p_{binom} = Prob(P_{binom} \geq P_{binom_{data}}). \tag{6.10}$$

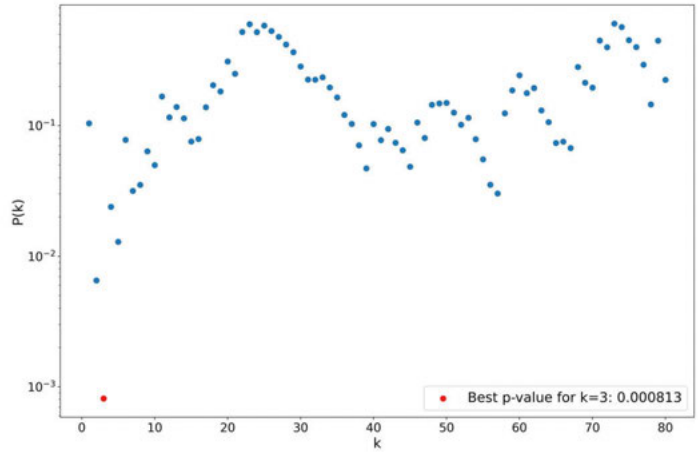

Figure 6.14. Single binomial trial for N=80 obtained using simulated p-values between 0 and 1 using a uniform normal distribution. The y-axis shows the $P(k)$, and the x-axis shows the k value. Highlighted in red is the best p-value for k-value or P_{binom}.

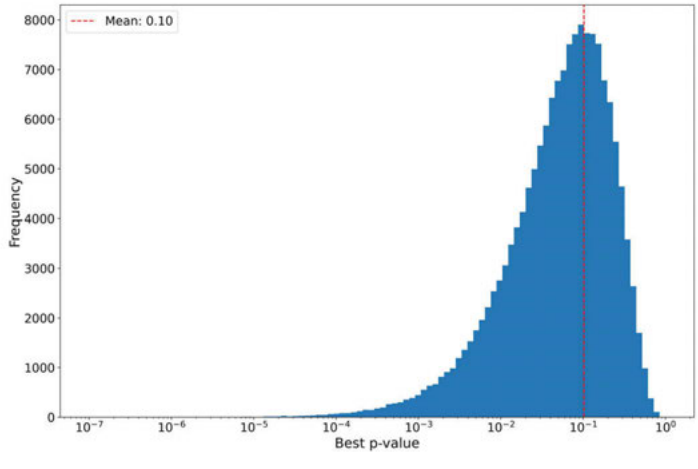

Figure 6.15. Distribution of best binomial p-values for N=80 obtained using simulated p-values between 0 and 1 using a uniform normal distribution. The x-axis shows the $P_{binom}(k)$ for $1.5 \cdot 10^5$ trials and in red dashed line showing the mean of the distribution.

6.4.3 Discussion

This section outlines the motivation and methodology for searching for MeV neutrino bursts from transients that produce GWs and bursts of thermal neutrinos, as detailed in **Paper IV**. This analysis marks the first search for MeV neutrinos correlated with GWs within IceCube. However, Due to the blindness policy governing IceCube analyses, this search was not yet unblinded at the time of writing. Once approval is granted, the methodology will be applied to on-time data to reveal the results.

6.5 High-Energy Neutrinos from CCSNe

6.5.1 Motivation

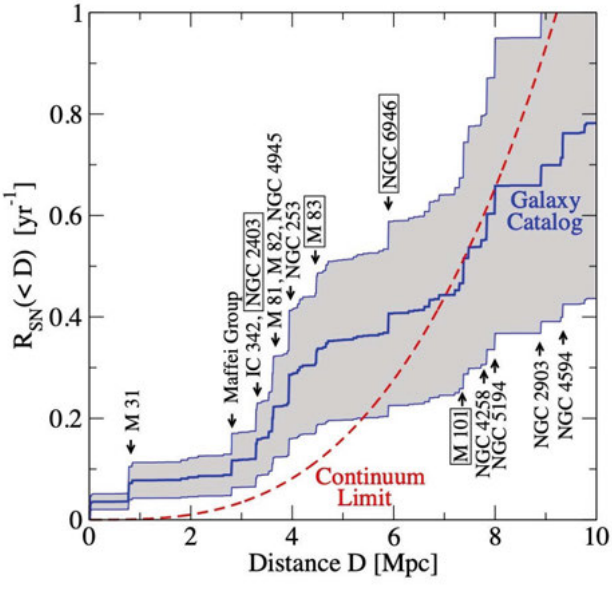

Figure 6.16. Yearly CCSNe rate as a function of distance. On the y-axis, we have the yearly CCSNe rate, and on the x-axis, the distance. The red dashed line represents the continuum in star formation rate, and the blue curve represents the CCSNe rate, including uncertainties. Reproduced from [14].

As we have seen in Section 5.4, due to the nature of IceCube's MeV analysis, the sensitivity for transients that produce an electron antineutrino luminosity of $O(10^{52} - 10^{53}$ erg/s) is in the O(10's) kpc (see Fig. 5.22) or to the Magellanic Clouds. With this reach, we are limited to 1-2 CCSNe per century in the Milky Way [13], and similarly for the LMC and SMC (see Fig. 6.16). In addition, some CCSNe EM emission might be obscured by dust, especially in starburst sites, where the photon emission can be so heavily reprocessed that it

becomes reddened to the IR [211] or even completely obscured [212, 213]. As shown in Fig. 6.16, the probability of observing a CCSNe increases with distance. Motivated by the increase in CCSNe with $\sim D^3$ [142] and the potential EM obscuration of CCSNe, we wanted to investigate IceCube's detection horizon for HE neutrinos from CCSNe. We investigated CSM-ejecta and choked jets using two HE neutrino flux models.

6.5.2 Analysis Methodology

Number of Neutrinos Observable by IceCube

To determine how many HE neutrinos IceCube can observe as a function of distance averaged over direction, we can use the following convolution;

$$N_\nu = \frac{1}{(d/d_{ref})^2} \int_{t_{min}}^{t_{max}} \int_{E_{min}}^{E_{max}} \phi_\nu(E_\nu, t) A_{eff}(E_\nu) dt dE_\nu \tag{6.11}$$

where d is the distance to source, d_{ref} is the distance at which the model flux is provided, t_{min} and t_{max} are the minimum and maximum observation time, E_ν is the neutrino energy, $\phi_\nu(E_\nu, t)$ is the model flux, and $A_{eff}(E_\nu)$ is the effective area, which is the neutrino detection sensitivity for the detector.

Data Samples

For this work, we used two different public data samples from IceCube to obtain the A_{eff}, motivated by the energy distribution of the flux (Fig. 6.17 and Fig. 6.18) from few GeV to few PeV, with peak flux around 10 TeV to few PeV depending on the model. As mentioned earlier, the effective area encodes the detector response as a function of neutrino energy, and different data samples have different efficiencies, primarily due to the efficiency of the background cuts; for the northern sky, the typical selection is of events originating below the horizon (up-going events), resulting in a sensitivity to only ν_μ-induced tracks. This selection allows the detector volume to be larger than the geometrical volume. However, this selection cannot be extended efficiently past 5° above the horizon (see Fig. 5.11 for IceCube's horizon) without considerably diminishing the effective detector volume. This is because strict cuts have to be placed to filter the atmospheric muon background, allowing for only very high-energy events with high-quality reconstruction to be accepted. An alternative for below the horizon, or the Southern sky, is *starting events* (contained events). These can be used to observe as many events as possible in the Southern sky at lower energies O(>GeV). In order to determine which IceCube sample was optimal for our analysis, we compared the model fluences with the effective area for the data samples.

CSM-ejecta model

In Fig. 6.17, we compared the fluence for the CSM-ejecta model at a maximal integration time of $t_{max} = 10^{5.8}$ s for Type II-P SN, and $t_{max} = 10^{7.5}$ s for Type IIn [8], against the angle-averaged effective areas. The CSM-ejecta model has a flux that starts at the low GeV and terminates at the low PeV, with the bulk of the flux between GeV-TeV. Therefore, for the northern sky, the track sample performs the best in the energy range of interest. For the southern sky, the MESE sample performs the best, especially considering that all flavors of neutrinos can be observable.

Choked-jets model

We also checked the optimal data samples for the choked-jet model, plotting the fluence against the effective areas as seen in Fig. 6.18. Although they are shown as individual components, we can see that the fluence has an energy range of TeV to PeV, with a higher flux component between 1 TeV and a few PeV. For the northern sky, the most neutrinos were observable with the Tracks sample, whereas in the south, it was with the MESE sample.

10 Year Point Source Sample - Tracks

This dataset consists of events between April 6, 2008, and July 8, 2018 [214] and consists of only muon tracks. It includes events from the seasons prior to the completion of the detector (IC40, IC 59, and IC79) and the seasons after detector completion, which are named IC86[9]. This dataset consists of high-quality, high-energy muon tracks that pass through the detector. For the southern sky, this data sample applied an energy cut of $E_{min} \approx 10$ TeV to reduce atmospheric muons (see Fig. 6.17b), in addition to vetos.

Medium Energy Starting Events 2 Year Sample - MESE

This dataset consists of events that started within the instrumented volume between May 2010 and May 2012 [167]. The typical strategy for starting event analyses is selecting events that have the interaction vertex within the detector volume with the outer layer acting as the veto to help reject atmospheric muons, with an additional energy cut of about $\approx$ 10's TeV [215] to ensure that no lower energy muons pass through. In order to increase the energy sensitivity to lower energy neutrinos, different vetos are required. For the MESE sample, they employed the whole detector as veto, where isolated photons detected could be used to veto an event depending on where and when it is detected with respect to the interaction vertex of an event. The result is a sample of events that started within the detector volume with a minimum energy of 1 TeV.

[8] These maximal times refer to the longest period during which neutrinos can be efficiently produced, ending when the shock radius matches the radius of the CSM [84]

[9] IC standing for IceCube and the following number being the number of available strings.

Averaging effect to the Effective Area

For this work, we used a declination-averaged effective area to inform the total number of observable neutrinos. We found that averaging the effective area did not affect considerably the number of neutrinos observable at the energies that we were interested in, with the extremes being $\sim +7\%/-19\%$ for northern sky tracks and $\sim +5\%/-3\%$ for the southern sky MESE, as shown in Fig. 6.19.

CCSNe Rate of Nearby Galaxies

In order to determine if we could reach interesting galaxies with HE neutrinos from CCSNe, we took two approaches to infer the CCSNe rate: Inferred rates for nearby galaxies and direct observation for more distant galaxies. For nearby distances O(few Mpc), since there have been no observed CCSNe [10], we used a catalog of inferred CCSNe rate computed by measuring H_α lines, which is an indicator of star formation activity [48]. For further distances, O(10's Mpc), we obtained a CCSNe rate from direct optical observations of CCSNe, computed using the Zwicky Transient Facility (ZTF)[11] [216] catalog for the northern hemisphere, and the All-Sky Automated Survey for Supernovae (ASAS-SN)[12] [217], for the southern hemisphere. Because these longer reaches were limited to the CJ model, we obtained the CCSNe rate for that model using observations of Type Ib, Ic, and IIb SNe and scaled it to a yearly number to obtain R_{SN}. We chose ZTF for the northern sky due to the great sky coverage, surveying the whole northern sky every two days, and a high rate of annual visits per source [218]. For the southern sky, we selected ASAS-SN for its capability of monitoring the whole sky every 2-3 days [219], although it has fewer annual visits per source compared to ZTF [218].

6.5.3 Discussion

We have presented the motivation and methodology to the work from **Paper V**. We obtained IceCube's detection horizon for HE neutrinos from CCSNe for both CSM-ejecta and CJ models, covering a population of 87% of CCSNe. We demonstrated that the detection horizon can be extended to a few Mpc with the CSM-ejecta model and close to 100 Mpc with the CJ model. We demonstrated that we can expect one CCSNe harboring CJ to be observable via neutrinos in 10 years of IceCube data, assuming a neutrino singlet, or in 15 years of IceCube data, assuming a neutrino doublet. In this work, we considered two specific models that make a moderate prediction of neutrinos expected, as well

[10] Except SN 1987A.

[11] `https://sites.astro.caltech.edu/ztf/bts/explorer.php?f=s&subsample=ccsn&ztflink=lasair&format=table&reverse=y`

[12] `https://www.wis-tns.org`

as assuming a moderate prediction for the CCSNe sub-population that could have jets. Although our work covered a small parameter space, it contributes to the much-needed prospects on the CCSNe detection horizon. The neutrino flux is dependent on many parameters, such as the assumed spectral index of the CR [82, 84], the CR energy [88], the shock velocity [88] and even the collimation of the jets [220, 104]. Therefore, the neutrino flux from CSM-ejecta mechanisms of CJ mechanisms likely lies in a distribution, with all possible parameter spaces affecting it. Therefore, making any definitive statement on the models is challenging.

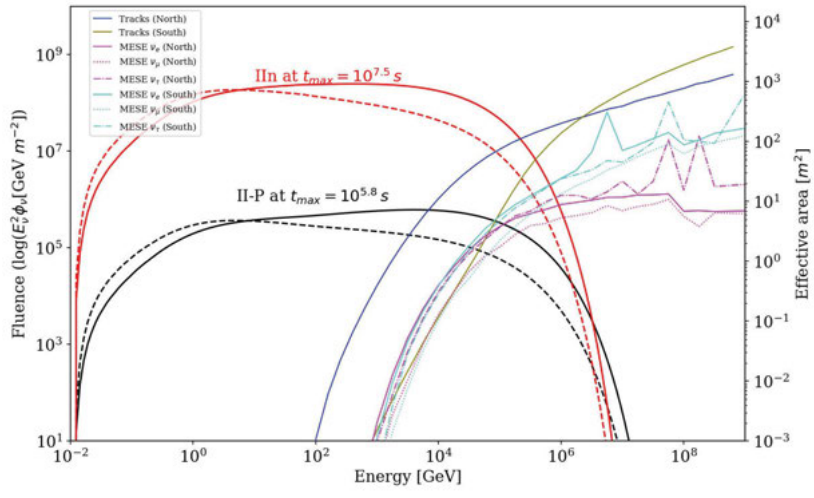

(a)

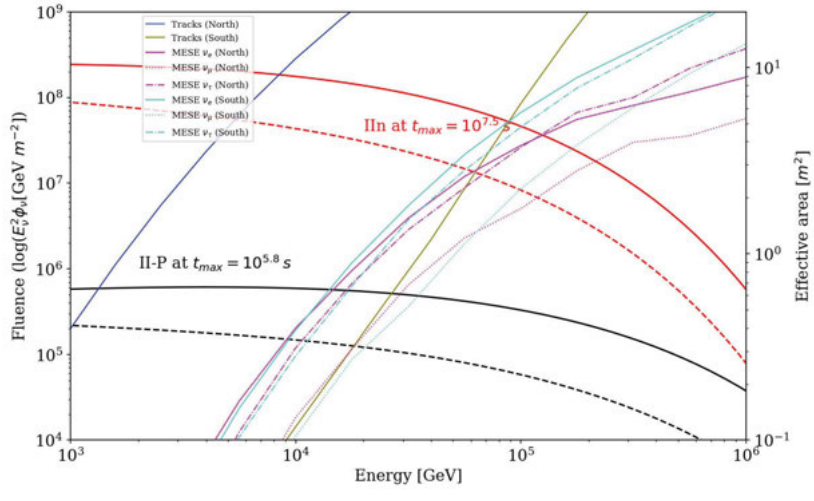

(b)

Figure 6.17. CSM-Ejecta model fluence with the two different effective areas used in this study. The x-axis represents the energy, the left y-axis represents the neutrino energy fluence, and the right axis represents the effective area. a) The plot shows the two different fluences used in this study, where the red curve is for type IIn and the black curve is for type II-P. The solid curve represents the fluence with a proton spectral index of s=2.0, and the dashed curve represents s=2.2, evaluated at d = 10 kpc and $t_{max} = 10^{5.8}$ s for type II-P and $t_{max} = 10^{7.5}$ s for type IIn. All the other curves represent the effective area; the blue curve represents the northern sky track's effective area, and the olive curve represents the southern sky track. The turquoise curves are for the northern sky Medium Energy Starting Event (MESE) effective area for different flavors, and the magenta curves are for the southern sky, where solid is for ν_e, the dotted line is for ν_μ, and the dash-dot is for ν_τ. b) Zoomed-in version of plot a).

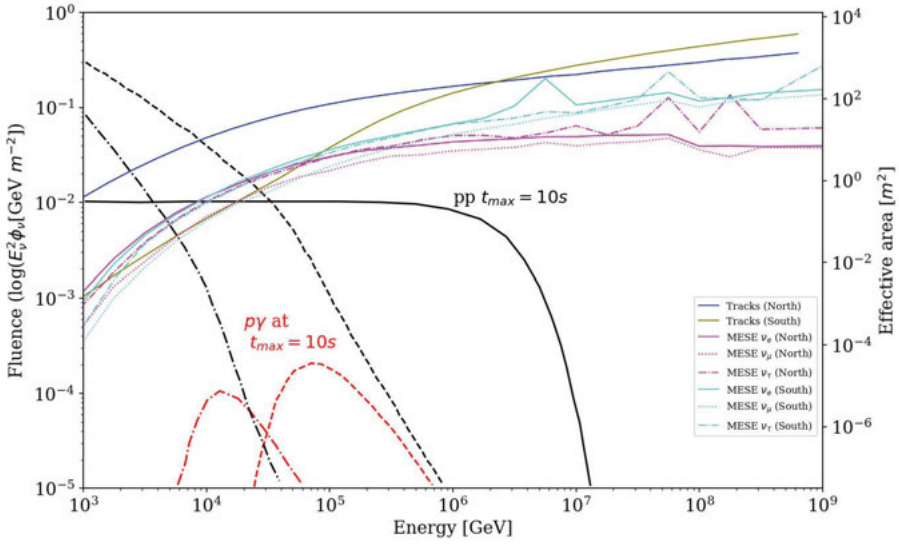

Figure 6.18. CJ model fluences against the different effective areas. The x-axis represents the energy, the left y-axis represents the neutrino energy fluence, and the right axis represents the effective area. The black and red curves are the different channels contributing to the neutrino fluence. All the other curves represent the effective area; the blue curve represents the northern sky track's effective area, and the olive curve represents the southern sky track. The turquoise curves are for the northern sky Medium Energy Starting Event (MESE) effective area for different flavors, and the magenta curves are for the southern sky, where solid is for ν_e, the dotted line is for ν_μ, and the dash-dot is for ν_τ.

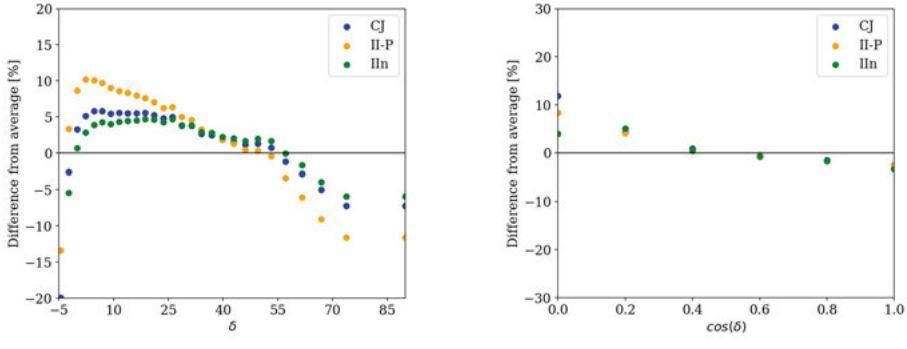

(a) *(b)*

Figure 6.19. Effect of averaging the declination. a) The neutrino detection horizon variability of the northern sky track sample as a function of the declination. The y-axis shows the difference from the average effective area, and the x-axis shows the declination in degrees. As we can see, the variability in the detection horizon depending on the declination is $\approx 10\%$.b) The neutrino detection horizon variability of the southern sky MESE sample, depending on the direction of arrival, as we can see, is $\lesssim 10\%$.

7. Summary and Conclusions

This thesis explored neutrinos from transient sources associated with the death of stars, ranging from low-energy (MeV) to high-energy (>GeV) events like CCSNe, GRBs, and NS mergers. While low-energy neutrinos were detected from a CCSN in 1987, the other sources remain undetected via neutrinos. The main aim of the analyses presented was to expand our prospects to observe these sources through neutrinos and to develop new tools and techniques for future research. For MeV neutrino searches, due to the high background floor, we use other messengers such as photons and gravitational waves to inform our search in hopes of discovering neutrinos from these incredible cosmic laboratories. To search for these neutrinos, we made use of data from the cubic km neutrino telescope located at the South Pole, the IceCube Neutrino Observatory, which boasts of an incredible detection sensitivity from MeV to over PeV and an observation up-time of over 95%.

In **Paper I**, we searched for MeV neutrinos from one of the brightest GRBs of all time, the GRB 221009A. We searched for neutrinos using six different time windows, informed by the gamma-ray light curve and the different models that predict thermal neutrinos, for example, from NDAFs. Since we did not observe an excess, we placed 90% C.L. U.L. on the neutrino flux and luminosity, assuming a blackbody spectrum with a mean energy of 15 MeV. In **Paper II**, we demonstrated a new method to set U.L. that does not make assumptions on the spectral shape but rather assumes that all of the flux or luminosity is emitted in a single energy bin, and we produced this mono-energetic 90% C.L. U.L. for GRB 221009A. In **Paper III**, we demonstrated a new analysis stream to search for MeV neutrinos, allowing IceCube to respond in real time to external alerts using the MeV data stream. Its first planned application is the follow-up of LVK O4 alerts. In **Paper IV**, we demonstrated the methodology for searching for MeV neutrinos correlated with gravitational waves. We used the binomial test to find if a sub-population of the LVK O1, O2, and O3 catalog are neutrino emitters. IceCube analyses are subject to blindness, where the analysis has to be developed and tested before looking at data to reveal the result. At the time of writing this thesis, the analysis from **Paper IV** is pending approval from the IceCube collaboration to unblind. Although the analysis in **Paper III** has received approval for unblinding, there has been a delay in deploying the South Pole component PySNDAQ. Finally, in **Paper V**, we investigated HE neutrinos from CCSNe, exploring how IceCube's detection horizon can be extended to distances where optical observations of CCSNe have been made.

The MeV neutrino search from GRB 221009A and the LVK O1+O2+O3 catalogs represent novel implementations of the potential capabilities with the IceCube SN data stream. The GRB analysis was the first to search for MeV neutrinos from GRBs in IceCube and the first to search for neutrinos from a GRB with a large energy range in IceCube. This analysis set the framework for low-energy neutrino searches, such as the MeV neutrino search with GWs. It also provided the motivation for developing the methodology to set model-independent limits on MeV neutrinos in IceCube and the development of the MeV Fast Response Analysis tool. These advancements allow IceCube to follow up external alerts from the astronomical community with SN data, expanding its fast response pipeline energy sensitivity from MeV to PeV. This expansion will not only aid in the quest to find neutrinos from transient sources but also help our understanding of these sources by combining more messengers that we can observe and covering a larger energy range. When looking at HE neutrinos from CCSNe, we demonstrated that it is possible to extend the detection horizon past the LMC, close to 100 Mpc, or over three orders of magnitude more, significantly expanding our detection horizon for CCSNe, and we demonstrated that one of such source should be observable in 10 years of IceCube data.

This work contributes to the growing body of work in the astroparticle community trying to understand the cataclysmic events that stem from the death of stars. Looking ahead, future improvements in detector size and technology, such as the planned IceCube-Gen2 [221], could significantly increase the detection horizon for HE neutrinos from CCSNe and enhance the sensitivity for bursts of thermal neutrinos from transients. Moreover, anticipated improvements in the reconstruction of higher-energy events O($>$ 100 MeV) and improvements in the characterization of the atmospheric muon background for low-energy neutrino searches could lead to substantial improvements in sensitivity.

8. Swedish Summary - Svensk Sammanfattning

Avhandligens titel: *Att Söka efter IceCube-neutriner från stjärndöd och framåt: Från MeV- till PeV-energi*

Denna avhandling syftade till att söka efter neutriner inom olika energiområden från astrofysikaliska källor som härrör från stjärndöd, vilket kallas en supernova. Dessa källor är en klass av transienta källor, som är astrofysikaliska händelser som inträffar på korta tidsskalor i kosmos utveckling. Forskningen genomfördes med hjälp av IceCube-data och projektet utfördes vid Uppsala universitet inom ramen för IceCube-samarbetet, som består av över 350 aktiva forskare inkusive över 15 forskare vid Uppsala och Stockholms universitet.

Stjärndöd och framåt

Stjärndöden, eller supernovan, är en av universums mest fantastiska händelser och frigör enorm energi i ett utbrott som sprider livsviktiga element över kosmos. När en stjärna har förbrukat sitt kärnbränsle, kollapsar dess kärna under gravitationen vilket leder till en massiv explosion som kastar stjärnans yttre lager ut i rymden. Denna explosion är så ljus att den kan överglänsa hela galaxer under en kort tid. Explosioner som dessa spelar en viktig roll i universum genom att sprida tunga element som är avgörande för att bilda nya stjärnor och planeter. Under explosionsprocessen, för en typ av supernova som kallas kärnkollaps-supernova, består upp till 99% av den frigjorda energin består av ett utbrott av lågenergineutriner, vilket resulterar i triljoner av neutriner inom några sekunder, som kommer från djupt inne i stjärnans kärna. För att ge en uppfattning, kan en supernova i bara några sekunder frigöra fler neutriner än antalet fotoner som solen sänder ut under sin hela livstid!

Även om dessa neutriner kallas lågenergi- är de fortfarande otroligt energiska med energier i megaelektronvolt (MeV), vilket är över en miljon gånger mer energiskt än en foton av synligt ljus. Men denna explosion är inte slutet på historien. En neutronstjärna eller ett svart hål kan bli kvar efteråt. Före explosionen kan stjärnan genomgå en förlust av materia under hela sin livslängd. Denna materia färdas bort från stjärnan under åren och bildar nästan det vi kan kalla ett 'moln' av materia eller cirkumstellär materia. När explosionen äger rum och lågenergineutrinerna frigörs, färdas chockvågor utåt, passerar genom lager av materia tills de bryter igenom, och det är då ljus, eller

fotoner, produceras vilket vi skulle kunna observera med blotta ögat om en supernova skulle explodera i galaxen Betelgeuse. När denna chockvåg fortsätter att färdas utåt börjar den stöta på cirkumstellär materia. Om förhållandena är rätt kan partikelacceleration äga rum. Denna partikelacceleration är liknar av forskare tillverkade acceleratorerna vi har på jorden, som Large Hadron Collider, men vid en energiskala som skulle vara omöjliga att uppnå på jorden. För att ge konkretisera kan partiklar i astrofysikaliska acceleratorer uppnå energier biljoner gånger större än vad vi kan uppnå i tillverkade acceleratorer. Partikelacceleration kan ske inte bara när chocker färdas utåt och interagerar med cirkumstellär materia, utan också om det svarta hålet som bildades roterar, där materia sugs in i magnetfältets virvlar och producerar 'jettar' av partiklar, där många, många chocker inträffar när de färdas ut. När dessa chocker interagerar med materia i jetten eller med cirkumstellär materia, kan högenergi-neutriner produceras vid giga- till petaelektronvolt (GeV till PeV), som är mellan tusen och en biljard gånger större i energi än lågenergineutrinerna.

Förutom svarta hål kan neutronstjärnor produceras under en supernova vilka är den kvarvarande kärnan av en supernova. Dessa nya stjärnor, som mestadels består av neutroner och är mycket tätt packade, skapar idealiska förhållanden för extrema tillstånd av materia, vilket gör dem utmärkta laboratorier för att studera fysik under de mest extrema förhållandena, som mycket hög densitet och superstark gravitation. Att studera dem för att förstå materia under normala förhållanden kan dock vara knepigt eftersom många neutronstjärnor är svåra att upptäcka eftersom de inte avger tillräcklig strålning. Om neutronstjärnan däremot snurrar tillräckligt snabbt kan partikelacceleration äga rum vid stjärnans poler vilket producerar högenergistrålning. Om polerna är riktade mot jorden kan vi observera dem i 'pulser' när de roterar in och ut ur vår axel. Dessa kallas Pulsarer. Men detta gör det inte möjligt att se djupt in i neutronstjärnans extrema system.

Under en neutronstjärnas livscykel kan den kretsa i binära system med andra neutronstjärnor eller med ett svart hål. Denna omloppsbana får dem att förlora energi genom krusningar i rumtiden, eller gravitationsvågor, vilket får dem att kretsa närmare och närmare varandra, rotera snabbare och snabbare, tills de kolliderar, vilket orsakar en massiv energiutlösning och producerar gravitationsvågor som vi ibland kan upptäcka, kallad en *sammanslagningshändelse*. Under denna korta händelse som varar några sekunder, komprimeras den täta neutronstjärnematerian ytterligare, och tunga element som guld och platina bildas och frigörs i rymden. Denna kompression kan producera och frigöra mycket lågenergi-neutriner. Historien fortsätter: kärnkollapssupernovor och neutronstjärne-sammanslagningar kan orsaka en extremt energisk explosion känd som gammablixt, där en intensiv blixt av gammastrålar, den ljusform med högst energi, produceras.

Antt att supernovor kan producera extrema ljusutsläpp för att observera dem, och neutronstjärnor kan producera ljus inte bara som Pulsarer utan också

gravitationsvågor och extrema ljusuttbrott under sammanslagningen, varför pratar vi då om neutriner? Hittills har vi bara diskuterat dem i produktionssammanhang. Kom ihåg att vi kan ha lågenergi-neutriner som produceras under extrema förhållanden av densitet och temperatur via kärnprocesser och högenergi-neutriner som kräver extrema hastigheter och kollisioner. Båda ger oss olika information om systemet. Dessa olika budbärare, som ljus, gravitationsvågor och neutriner vid olika energier, är fördelen med *multi-messenger* och *multi-energy* astrofysik som ger oss olika pusselbitar av kosmos vilket gör att vi kan undersöka olika områden och mekanismer för att förstå dessa magnifika platser.

Neutriner - en del av pusslet

Neutriner är små subatomära osynliga partiklar. De är de minsta och lättaste kända partiklarna, med mycket lägre massa än atomer eller elektroner. Men till skillnad från elektroner bär neutriner ingen elektrisk laddning. Detta betyder att de inte interagerar med elektriska eller magnetiska fält vilket gör dem mycket svåra att upptäcka eftersom de passerar genom materia som om den inte existerade. Men denna egenskap är också en välsignelse; eftersom de färdas genom rymden utan att interagera kan de användas som 'pekande vapen' mot ursprunget. Även om de sällan interagerar med materia så händer det att de gör det, särskilt när neutrinoenergin ökar. För att fånga dessa neutriner behöver vi en enorm detektor med minimalt brus för att observera dem, som IceCube Neutrino Observatory.

IceCube neutrinoobservatorium

IceCube Neutrino Observatory är en enorm neutrinodetektor på 1 kubikkilometer, belägen vid Sydpolen och begravd mycket djupt i isen, så djupt som 2400 m ned. Detektorn består av över 5000 kameror som övervakar den klara antarktiska isen på jakt efter neutriner. När tillräckligt energiska neutriner passerar genom isen kan de interagera med den och producera laddade partiklar. Cherenkovstrålning produceras när dessa laddade partiklar färdas genom isen snabbare än ljusets hastighet i is. Denna strålning är fotoner med våglängder mellan UV-strålning och optisk strålning, som kamerorna kan detektera. Sedan, med mycket komplexa algoritmer och analyser, många statistiska verktyg och en förståelse för vår 'förorening', kan vi bestämma hur många neutriner som passerade, varifrån de passerade, om de är tillräckligt energiska och andra neutrinoegenskaper vilket gör att vi kan studera det astrofysikaliska universumet i det osynliga av det elektromagnetiska spektrat.

Avhandlingens ämne

I denna avhandling beskriver jag sökandet efter MeV-neutriner från gammablixt och Neutron Star Mergers med hjälp av IceCube-data. Vi använde information från andra budbärare, som gamma-strålar för gammablixt och gravitationsvågor för neutronstjärnesammanslagningar, för att ta reda på hur och när vi skulle söka. I denna process sökte vi efter neutriner från de ljusaste gammablixt genom tiderna, 'Brightest of All Times' eller BOAT, GRB 221009A. Vi fann inget statistiskt signifikant av MeV-neutriner. Ändå satte vi konkurrenskraftiga gränser för den förväntade neutrino-flödet från den källan som teoretiker kan använda för att utveckla sina modeller. Våran var också den första analysen av sitt slag för en gammablixt i IceCube, där vi såg på neutrinoenergier från MeV till PeV. För att söka efter neutriner från neutronstjärnesammanslagningar använde vi gravitationsvågor upptäckta av LIGO-Virgo-KAGRA för att lägga grunden till våra sökningar. Vi utvecklade ett nytt verktyg där, när en varning från en annan multi-messenger-observatorium mottas och om källan skulle kunna vara en kandidat för MeV-neutriner, vi kan utföra en snabb analys med hjälp av satelliten som används av IceCube för att kommunicera med detektorn vid Sydpolen kan se data i realtid och rapportera tillbaka till gemenskapen om våra resultat om huruvida vi såg MeV-neutriner. Vi utvecklade också och förbättrade metoder för att söka efter MeV-neutriner från neutronstjärnesammanslagningar, och producerade den första analysen av sitt slag i IceCube.

Som nämnts tidigare är dock vår förmåga att upptäcka neutriner mer utmanande ju lägre energi de har, med till exempel supernovor som är observerbara med lågenergi-neutriner upp till de satellitgalaxer som kallas Stora Magellanska molnen och Lilla Magellanska molnen. Chansen att en supernovorxplosion sker i vår galax och de satellitgalaxerna är dock runt en gång var 40:e, vilket begränsar hur många vi kan observera via neutriner och därför studera egenskaperna hos. Fram till idag har endast en astrophysikalisk transient observerats med lågenergi-neutriner: Supernova 1987A, som inträffade 1987. Men vi vet att supernovor också kan producera högenergi-neutriner. Därför gjorde vi också en studie för att undersöka hur mycket längre ut vi skulle kunna nå. Vi fann att räckvidden till kärn-kollaps supernovor kan utvidgas till 2000 gånger mer än med lågenergi-neutriner, vilket gör att vi kan nå fler galaxer och därmed fler supernovor.

Arbetet som genomförts i denna avhandling bidrar till att främja sökandet efter neutriner från astrofysikaliska källor, och tillhandahåller nya verktyg och metoder för forskare och hjälper till att ge en pusselbit för att få en komplett bild av dessa extrema händelser.

9. Acknowledgements

It is a bittersweet realization that this journey has come to an end. Having started my Ph.D. only a few weeks after the pandemic began, it has been quite a long and interesting journey. Along the way, I have met many wonderful people who have helped me tremendously in learning and surviving this challenge.

First and foremost, I'd like to thank my main supervisor, *Erin O'Sullivan*, for allowing me to pursue my dream. I truly appreciate the feedback you have given me, helping me see things from a different perspective than I had considered. Thank you for teaching me the meaning of being concise and pragmatic in research. I also want to thank *Carlos Perez de los Heros*; you have made me feel very welcome from day one, and I appreciate our discussions over lunch or coffee. I want to thank the Uppsala and Stockholm groups, *Olga Botner*, *Allan Hallgren*, *Christian Glaser*, *Chad Finley*, *Klas Hultqvist*, *Alan Coleman* and *Thorsten Glüsenkamp* for the enjoyable environment and feedback that I have received throughout these years. You have made me a better researcher.

To my fellow Ph.D. colleagues, I have no words to express how much your support has meant to me. To *Jakob Beise*, thank you for always being there, listening to my ups and downs, sharing awesome trips, and feasting in conference dinners. I am so glad to have met and call you my friend. I hope we can have many more crazy adventures in the future. To *Nils Heyer*, as I said in my previous thesis, I know you aren't a fan of acknowledgments, but again, here you are. Thank you for being there, especially during quite stressful times. *Axel Ponten*, I look forward to sharing more collaboration meeting shenanigans and maybe attending one of your DJ-ing sessions. I promise. To *Martin Ravn*, I am very glad you joined our group. To *Alex Burgman*, I still remember the wonderful email you sent me welcoming me to the group; it set the tone for my next few years. Thank you for supporting me from the beginning, answering all my silly questions, hearing me complain about my code not working (helping me debug when it seemed hopeless!), and giving me insightful knowledge on navigating research life. To *Olga Gudnadottir* and *Christina Dimitriadi*, where to even begin...if you know, you know. Thank you for your endless support and guidance in these last stages, and thank you, Olga, for the help with the Swesih summary. *Jila Shams*, without you, these months would have been much more difficult. Thank you for your guidance in preparing my thesis and for listening to me. *Lorenzo Senis*, thank you for your support.

To my friends, *Ankur*, thank you so much for being there for me. We started during the home office era, and you made it so much more bearable and gave me so much insightful knowledge on navigating research life. I genuinely helpef me survive this. To *Megan*, my dear friend, you have no idea how much your encouragement has meant to me. Thank you for listening to me talk about my paper, my code, or my challenges for the millionth time, and I look forward to many more trips together. To my dearest *Julia*, thank you for your endless support throughout all these years. To my dear *Holly*, thank you so much for all the memes we exchanged, keeping me sane and putting a smile on my face. I really appreciate your conversations.

I also want to thank the IceCube collaboration at large, especially the supernova working group members, *Segev*, *Gwen*, *Karlijn*, *Mathieu* and *Per*. You have made my time much more pleasant. To *Spencer*, I have no words to express my gratitude. You have made it possible for me to survive this in so many ways and helped me survive through all the technical challenges. I really hope our paths cross again at some point. I want to thank my colleagues at the HEP-nuclear division, *Karin*, *Michael*, *Rikard*, *Jana*, *Di*, *Yong Shen*, *Arnaud*, *Axel*, *Rebeca*, *Giulia* and many more for making me feel welcome and for our discussions. I also want to thank my colleagues at the department, especially the Ph.D. council, for making my work as an ombudsman so pleasant.

Finally, to the most important people in my life, my husband *Juuso Mattila* and my mom *Pirjo Valtonen*. I cannot thank you enough for supporting me in this dream. I know it has not been easy to tolerate me during this stressful time. I want to thank you for believing in me despite all kinds of difficulties in life. I know I can always count on you.

References

[1] S. A. Colgate and R. H. White, *THE HYDRODYNAMIC BEHAVIOR OF SUPERNOVAE EXPLOSIONS**, *Astrophysical Journal* **143** (1966) 626.

[2] D. K. Nadyozhin, *THE NEUTRINO RADIATION FOR A HOT NEUTRON STAR FORMATION AND THE ENVELOPE OUTBURST PROBLEM*, *Astrophysics and Space Science* **53** (1978) 131–153.

[3] H. A. Bethe and J. R. Wilson, *REVIVAL OF A STALLED SUPERNOVA SHOCK BY NEUTRINO HEATING*, *Astrophysical Journal* **295** (1985) 14–23.

[4] K. Hirata, T. Kajita, M. Koshiba, M. Nakahata, Y. Oyama et al., *Observation of a neutrino burst from the supernova SN1987A*, *Physical Review Letters* **58** (4, 1987) 1490–1493.

[5] R. M. Bionta, G. Blewitt, C. B. Bratton, D. Casper, A. Ciocio et al., *Observation of a neutrino burst in coincidence with supernova 1987A in the Large Magellanic Cloud*, *Physical Review Letters* **58** (4, 1987) 1494–1496.

[6] E. N. Alexeyev and L. N. Alexeyeva, *Detection of a neutrino signal from SN 1987A on February 23, 1987 at 7:35 UT: Data from the Baksan Underground Scintillation Telescope*, *Astronomy Letters* **34** (11, 2008) 745–752.

[7] R. McCray, *The Physics of Supernova 1987A*, in *Handbook of Supernovae*, pp. 2181–2210. Springer International Publishing, 2017. DOI.

[8] F. Vissani and G. Pagliaroli, *How much can we learn from SN1987A events? Or: An analysis with a two-Component model for the antineutrino signal*, in *4th International Workshop on Neutrino Oscillations in Venice: Ten Years after the Neutrino Oscillations*, pp. 215–231, 7, 2008.

[9] KM3NeT Collaboration, S. Aiello, A. Albert, S. A. Garre, Z. Aly et al., *The KM3NeT potential for the next core-collapse supernova observation with neutrinos*, *The European Physical Journal C* **81** (5, 2021) .

[10] IceCube Collaboration, R. Abbasi, Y. Abdou, T. Abu-Zayyad, M. Ackermann et al., *IceCube Sensitivity for Low-Energy Neutrinos from Nearby Supernovae*, *Astronomy & Astrophysics* **535** (12, 2011) .

[11] S.-K. Collaboration, :, M. Ikeda, A. Takeda, Y. Fukuda et al., *Search for Supernova Neutrino Bursts at Super-Kamiokande*, *The Astrophysical Journal* **669** (2007) .

[12] KM3NeT Collaboration, S. Aiello, A. Albert, M. Alshamsi, S. A. Garre et al., *Implementation and first results of the KM3NeT real-time core-collapse supernova neutrino search*, *The European Physical Journal C* **82** (4, 2022) .

[13] K. Rozwadowska, F. Vissani and E. Cappellaro, *On the rate of core collapse supernovae in the Milky Way*, *New Astronomy* **83** (2, 2021) .

[14] i. Ando, J. F. Beacom and H. Yüksel, *Detection of Neutrinos from Supernovae in Nearby Galaxies*, *Physical Review Letters* **95** (10, 2005) .

[15] R. Davis, D. S. Harmer and K. C. Hoffman, *Search for Neutrinos from the Sun*, *Physical Review Letters* **20** (5, 1968) 1205–1209.

[16] V. P. Utrobin, A. Wongwathanarat, H.-T. Janka and E. Müller, *Supernova 1987A: neutrino-driven explosions in three dimensions and light curves*, *Astronomy & Astrophysics* **581** (9, 2015) A40.
[17] S. Orlando, M. Miceli, M. L. Pumo and F. Bocchino, *SUPERNOVA 1987A: A TEMPLATE TO LINK SUPERNOVAE TO THEIR REMNANTS*, *The Astrophysical Journal* **810** (9, 2015) 168.
[18] R. Indebetouw, M. Matsuura, E. Dwek, G. Zanardo, M. J. Barlow et al., *DUST PRODUCTION AND PARTICLE ACCELERATION IN SUPERNOVA 1987A REVEALED WITH ALMA*, *The Astrophysical Journal* **782** (1, 2014) L2.
[19] M. G. Aartsen, R. Abbasi, Y. Abdou, M. Ackermann, J. Adams et al., *Evidence for High-Energy Extraterrestrial Neutrinos at the IceCube Detector*, *Science* **342** (11, 2013) .
[20] B. P. Abbott, R. Abbott, T. D. Abbott, M. R. Abernathy, F. Acernese et al., *Observation of gravitational waves from a binary black hole merger*, *Physical Review Letters* **116** (2, 2016) .
[21] T. IceCube, Fermi-LAT, MAGIC, AGILE, ASAS-SN et al., *Multi-messenger observations of a flaring blazar coincident with high-energy neutrino IceCube-170922A*, *Science* **361** (7, 2018) .
[22] S. Ansoldi, L. A. Antonelli, C. Arcaro, D. Baack, A. Babić et al., *The Blazar TXS 0506+056 Associated with a High-energy Neutrino: Insights into Extragalactic Jets and Cosmic-Ray Acceleration*, *The Astrophysical Journal* **863** (8, 2018) L10.
[23] B. Abbott, R. Abbott, T. Abbott, F. Acernese, K. Ackley et al., *GW170817: Observation of Gravitational Waves from a Binary Neutron Star Inspiral*, *Physical Review Letters* **119** (10, 2017) 161101.
[24] A. Goldstein, P. Veres, E. Burns, M. S. Briggs, R. Hamburg et al., *An Ordinary Short Gamma-Ray Burst with Extraordinary Implications: Fermi-GBM Detection of GRB 170817A*, *The Astrophysical Journal Letters* **848** (10, 2017) L14.
[25] S. Valenti, J. Sand, David, S. Yang, E. Cappellaro, L. Tartaglia et al., *The Discovery of the Electromagnetic Counterpart of GW170817: Kilonova AT 2017gfo/DLT17ck*, *The Astrophysical Journal Letters* **848** (10, 2017) L24.
[26] D. M. Siegel, *GW170817 –the first observed neutron star merger and its kilonova: Implications for the astrophysical site of the r-process*, *The European Physical Journal A* **55** (11, 2019) 203.
[27] IceCube Collaboration, R. Abbasi, M. Ackermann, J. Adams, J. A. Aguilar et al., *Evidence for neutrino emission from the nearby active galaxy NGC 1068*, *Science* **378** (11, 2022) 538–543.
[28] R. Abbasi, M. Ackermann, J. Adams, J. A. Aguilar, M. Ahlers et al., *Observation of high-energy neutrinos from the Galactic plane*, *Science* **380** (7, 2023) 1338–1343.
[29] K. Murase and I. Bartos, *High-Energy Multimessenger Transient Astrophysics*, *Annual Review of Nuclear and Particle Science* **69** (2019) 477–506.
[30] Y. Fukuda, T. Hayakawa, E. Ichihara, K. Inoue, K. Ishihara et al., *Evidence for Oscillation of Atmospheric Neutrinos*, *Physical Review Letters* **81** (1998) .
[31] Q. R. Ahmad, R. C. Allen, T. C. Andersen, J. D.Anglin, J. C. Barton et al., *Direct Evidence for Neutrino Flavor Transformation from Neutral-Current Interactions in the Sudbury Neutrino Observatory*, *Physical Review Letters* **89**

(2002) .
[32] Q. R. Ahmad, R. C. Allen, T. C. Andersen, J. D. Anglin, G. Bühler et al., *Measurement of the rate of ve + d → p + p + e- interactions produced by 8B solar neutrinos at the sudbury neutrino observatory*, *Physical Review Letters* **87** (8, 2001) 71301–1.
[33] S. Bouquet, *The Jeans' criterion and the gravitational instability*, in *Dynamical Systems, Plasmas and Gravitation*, pp. 151–163. Springer, Berlin, 1999. DOI.
[34] M. S. Longair, *High energy astrophysics*. Cambridge University Press, 2011.
[35] C. Iliadis, *Nuclear Physics of Stars*. Wiley-VCH, Weinheim, second ed., 2015.
[36] S. E. Woosley, A. Heger and T. A. Weaver, *The evolution and explosion of massive stars*, *Reviews of Modern Physics* **74** (11, 2002) .
[37] A. W. Alsabti and P. Murdin, *Supernovae and Supernova Remnants: The Big Picture in Low Resolution*, in *Handbook of Supernovae*, pp. 3–28. Springer International Publishing, 2017. DOI.
[38] L. A. L. Da Silva, *The classification of supernovae*, *Astrophysics and Space Science* **202** (4, 1993) 215–236.
[39] D. Branch and J. C. Wheeler, *Supernova Explosions*. Springer, Berlin, Heidelberg, 1 ed., 2017.
[40] A. Odrzywolek and T. Plewa, *Probing thermonuclear supernova explosions with neutrinos*, *Astronomy & Astrophysics* **529** (5, 2011) .
[41] W. P. Wright, G. Nagaraj, J. P. Kneller, K. Scholberg and I. R. Seitenzahl, *Neutrinos from type Ia supernovae: the deflagration-to-detonation transition scenario*, *Physical Review D* **94** (5, 2016) .
[42] M. D. Kistler, W. C. Haxton and H. Yuksel, *Tomography of Massive Stars from Core Collapse to Supernova Shock Breakout*, *The Astrophysical Journal* **778** (11, 2013) .
[43] A. Haynie and A. L. Piro, *Shock Breakout in Dense Circumstellar Material with Application to PS1-13arp*, *The Astrophysical Journal* **910** (4, 2021) .
[44] E. Waxman and B. Katz, *Shock breakout theory*, in *Handbook of Supernovae*, pp. 967–1015. Springer, Cham, 7, 2016. DOI.
[45] A. J. Calzavara and C. D. Matzner, *Supernova properties from shock breakout X-rays*, *Monthly Notices of the Royal Astronomical Society* **351** (6, 2004) 694–706.
[46] M. C. Molla and SNEWS Collaboration, *SNEWS: A SuperNova Early Warning System in the multi-messenger era*, *Journal of Physics: Conference Series* **2156** (2021) .
[47] S. Gullin, E. O'Connor, J.-S. Wang and J. Tseng, *Neutrino Echos following Black Hole Formation in Core-Collapse Supernovae*, *The Astrophysical Journal* **926** (9, 2021) .
[48] K. Nakamura, S. Horiuchi, M. Tanaka, K. Hayama, T. Takiwaki et al., *Multi-messenger signals of long-term core-collapse supernova simulations : synergetic observation strategies*, *Monthly Notices of the Royal Astronomical Society* **461** (9, 2016) 3296–3313.
[49] W. R. Hix, O. E. Messer, A. Mezzacappa, M. Liebendörfer, J. Sampaio et al., *Consequences of nuclear electron capture in core collapse supernovae*, *Physical Review Letters* **91** (2003) .

[50] H. T. Janka, *Explosion mechanisms of core-collapse supernovae*, 2012. 10.1146/annurev-nucl-102711-094901.
[51] H. T. Janka, *Conditions for shock revival by neutrino heating in core-collapse supernovae*, *Astronomy and Astrophysics* **368** (2001) 527–560.
[52] D. Yakovlev, *Neutrino emission from neutron stars*, *Physics Reports* **354** (11, 2001) 1–155.
[53] I. Tamborra, G. Raffelt, F. Hanke, H.-T. Janka and B. Mueller, *Neutrino emission characteristics and detection opportunities based on three-dimensional supernova simulations*, *Physical Review D* **90** (5, 2014) .
[54] A. Wongwathanarat, E. Müller and H.-T. Janka, *Three-dimensional simulations of core-collapse supernovae: from shock revival to shock breakout*, *Astronomy & Astrophysics* **577** (5, 2015) A48.
[55] E. O'Connor, C. J. Horowitz, Z. Lin and S. Couch, *Core-Collapse Supernova Simulations including Neutrino Interactions from the Virial EOS*, in *Proceedings of the International Astronomical Union*, pp. 107–112, 2017. DOI.
[56] H. T. Janka, *Handbook of Supernovae: Neutrino Emission from Supernovae*. Springer, 11, 2017, 10.1007/978-3-319-21846-5_4.
[57] H. Nagakura and K. Hotokezaka, *Non-thermal neutrinos created by shock acceleration in successful and failed core-collapse supernova*, *Monthly Notices of the Royal Astronomical Society* **502** (3, 2021) 89–107.
[58] David Malin / Australian Astronomical Observatory, "SN 1987A Photo."
[59] A. Neronov, *Introduction to multi-messenger astronomy*, *Journal of Physics: Conference Series* **1263** (6, 2019) 012001.
[60] Y. Oyama, *Evidence of High-energy Neutrinos from SN1987A by Kamiokande-II and IMB*, *The Astrophysical Journal* **925** (2, 2022) 166.
[61] N. Smith, *Interacting Supernovae: Types IIn and Ibn*. Springer, 11, 2017, 10.1007/978-3-319-21846-5_38.
[62] A. Chiotellis, P. Boumis and Z. T. Spetsieri, *The Interaction of Type Ia Supernovae with Planetary Nebulae: The Case of Kepler's Supernova Remnant*, *Galaxies* **8** (2020) .
[63] S. Das and A. Ray, *Modeling Type II-P/II-L Supernovae Interacting with Recent Episodic Mass Ejections from Their Presupernova Stars with MESA and SNEC*, *The Astrophysical Journal* **851** (12, 2017) 138.
[64] R. A. Chevalier and C. Fransson, *Thermal and Non-thermal Emission from Circumstellar Interaction*, in *Handbook of Supernovae*, pp. 875–937. Springer International Publishing, 2017. DOI.
[65] D. Kasen, *Unusual Supernovae and Alternative Power Sources*, in *Handbook of Supernovae*, pp. 939–965. Springer International Publishing, 2017. DOI.
[66] B. T. Zhang and K. Murase, *Ultrahigh-energy cosmic-ray nuclei and neutrinos from engine-driven supernovae*, *Physical Review D* **100** (11, 2019) .
[67] K. Murase, T. A. Thompson, B. C. Lacki and J. F. Beacom, *New Class of High-Energy Transients from Crashes of Supernova Ejecta with Massive Circumstellar Material Shells*, *Physical Review D* **84** (8, 2011) .
[68] S. Razzaque, P. Mészáros and E. Waxman, *High Energy Neutrinos from Gamma-Ray Bursts with Precursor Supernovae*, *Physical Review Letters* **90** (6, 2003) .
[69] K. Ptitsyna and S. Troitsky, *Physical conditions in potential sources of ultra-*

high-energy cosmic rays: Updated Hillas plot and radiation-loss constraints, *Physics-Uspekhi* **53** (2010) .

[70] T. K. Gaisser, R. Engel and E. Resconi, *Cosmic rays and particle physics*. Cambridge University Press, 6, 2016, 10.1017/CBO9781139192194.

[71] V. Zirakashvili and V. Ptuskin, *Numerical simulations of diffusive shock acceleration in SNRs*, *Astroparticle Physics* **39-40** (12, 2012) 12–21.

[72] M. Kachelrieß and R. Tomàs, *High energy neutrino yields from astrophysical sources I: Weakly magnetized sources*, tech. rep., 2006.

[73] S. R. Kelner, F. A. Aharonian and V. V. Bugayov, *Energy spectra of gamma rays, electrons, and neutrinos produced at proton-proton interactions in the very high energy regime*, *Physical Review D* **74** (8, 2006) 034018.

[74] T. J. Moriya, *Mass loss of massive stars near the Eddington luminosity by core neutrino emission shortly before their explosion*, *Astronomy & Astrophysics* **564** (4, 2014) .

[75] A. Suzuki, T. J. Moriya and T. Takiwaki, *Supernova Ejecta Interacting with a Circumstellar Disk. I. Two-dimensional Radiation-hydrodynamic Simulations*, *The Astrophysical Journal* **887** (12, 2019) 249.

[76] M. Nicholl, P. K. Blanchard, E. Berger, R. Chornock, R. Margutti et al., *An extremely energetic supernova from a very massive star in a dense medium*, *Nature Astronomy* **4** (4, 2020) 893–899.

[77] D. A. Perley, J. Sollerman, S. Schulze, Y. Yao, C. Fremling et al., *The Type Icn SN 2021csp: Implications for the Origins of the Fastest Supernovae and the Fates of Wolf-Rayet Stars*, *The Astrophysical Journal* **927** (2022) .

[78] J. E. Andrews, D. Sand, S. Valenti, N. Smith and R. Dastidar, *SN 2017gmr: An Energetic Type II-P Supernova with Asymmetries*, *The Astrophysical Journal* (11, 2019) .

[79] V. Morozova, A. L. Piro and S. Valenti, *Measuring the Progenitor Masses and Dense Circumstellar Material of Type II Supernovae*, *The Astrophysical Journal* **858** (9, 2018) .

[80] F. Förster, T. J. Moriya, J. C. Maureira, J. P. Anderson, S. Blinnikov et al., *The delay of shock breakout due to circumstellar material seen in most Type II Supernovae*, *Nature Astronomy* **2** (9, 2018) 808–818.

[81] T. Pitik, I. Tamborra, C. R. Angus and K. Auchettl, *Is the high-energy neutrino event IceCube-200530A associated with a hydrogen-rich superluminous supernova?*, *The Astrophysical Journal* **929** (2022) .

[82] K. Murase, A. Franckowiak, K. Maeda, R. Margutti and J. F. Beacom, *High-Energy Emission from Interacting Supernovae: New Constraints on Cosmic-Ray Acceleration in Dense Circumstellar Environments*, *The Astrophysical Journal* **874** (3, 2019) .

[83] M. Petropoulou, S. Coenders, G. Vasilopoulos, A. Kamble and L. Sironi, *Point-source and diffuse high-energy neutrino emission from Type IIn supernovae*, *Monthly Notices of the Royal Astronomical Society* **470** (9, 2017) 1881–1893.

[84] K. Murase, *New Prospects for Detecting High-Energy Neutrinos from Nearby Supernovae*, *Physical Review D* **97** (4, 2018) .

[85] K. Murase, T. A. Thompson and E. O. Ofek, *Probing Cosmic-Ray Ion Acceleration with Radio-Submm and Gamma-Ray Emission from Interaction-*

Powered Supernovae, *Monthly Notices of the Royal Astronomical Society* **440** (5, 2014) 2528–2543.

[86] A. Kheirandish and K. Murase, *Detecting High-Energy Neutrino Minibursts from Local Supernovae with Multiple Neutrino Observatories*, *arXiv* (4, 2022) .

[87] V. N. Zirakashvili and V. S. Ptuskin, *Type IIn supernovae as sources of high energy astrophysical neutrinos*, *Astroparticle Physics* **78** (5, 2016) 28–34.

[88] P. Sarmah, S. Chakraborty, I. Tamborra and K. Auchettl, *High energy particles from young supernovae: gamma-ray and neutrino connections*, *Journal of Cosmology and Astroparticle Physics* **2022** (8, 2022) .

[89] N. Senno, K. Murase and P. Meszaros, *Choked Jets and Low-Luminosity Gamma-Ray Bursts as Hidden Neutrino Sources*, *Physical Review D.* (4, 2016) .

[90] S. Razzaque, P. Mészáros and E. Waxman, *HIGH ENERGY NEUTRINOS FROM A SLOW JET MODEL OF CORE COLLAPSE SUPERNOVAE*, *Modern Physics Letters A* **20** (2005) 2351–2367.

[91] A. Heger, C. L. Fryer, S. E. Woosley, N. Langer and D. H. Hartmann, *How Massive Single Stars End their Life*, *The Astrophysical Journal* **591** (2003) .

[92] J. S. Bloom, S. R. Kulkarni, F. Harrison, T. Prince, E. S. Phinney et al., *Expected characteristics of the subclass of Supernova Gamma-ray Bursts (S-GRBs)*, *The Astrophysical Journal* **506** (1998) .

[93] T. Piran, E. Nakar, P. Mazzali and E. Pian, *Relativistic Jets in Core Collapse Supernovae*, *The Astrophysical Journal Letters* **871** (1, 2019) .

[94] Z. Paragi, G. B. Taylor, C. Kouveliotou, J. Granot, E. Ramirez-Ruiz et al., *A mildly relativistic radio jet from the otherwise normal type Ic supernova 2007gr*, *Nature* **463** (1, 2010) 516–518.

[95] L. Izzo, A. de Ugarte Postigo, K. Maeda, C. C. Thöne, D. A. Kann et al., *Signatures of a jet cocoon in early spectra of a supernova associated with a γ-ray burst*, *Nature* **565** (1, 2019) 324–327.

[96] i. Ando and J. F. Beacom, *Revealing the Supernova-Gamma-Ray Burst Connection with TeV Neutrinos*, *Physical Review Letters* **95** (8, 2005) .

[97] S. Razzaque, P. Mészáros and E. Waxman, *TeV neutrinos from core collapse supernovae and hypernovae*, *Physical Review Letters* **94** (3, 2005) .

[98] H. B. J. Koers and R. A. M. J. Wijers, *Enhanced high-energy neutrino emission from choked gamma-ray bursts due to meson and muon acceleration*, *preprint* (11, 2007) .

[99] E. Berger, S. R. Kulkarni, D. A. Frail and A. M. Soderberg, *A Radio Survey of Type Ib and Ic Supernovae: Searching for Engine Driven Supernovae*, *The Astrophysical Journal* **599** (2003) .

[100] A. Bhattacharya, R. Enberg, M. H. Reno and I. Sarcevic, *Charm decay in slow-jet supernovae as the origin of the IceCube ultra-high energy neutrino events*, *Journal of Cosmology and Astroparticle Physics* **2015** (6, 2015) .

[101] R. Enberg, M. H. Reno and I. Sarcevic, *High energy neutrinos from charm in astrophysical sources*, *Physical Review D* **79** (3, 2009) .

[102] T. I. Collaboration, R. Abbasi, Y. Abdou, T. Abu-Zayyad, M. Ackermann et al., *Searching for soft relativistic jets in Core-collapse Supernovae with the IceCube Optical Follow-up Program*, *Astronomy & Astrophysics* **539** (2, 2012)

.
[103] P. C. Duffell and A. Y. Q. Ho, *How Dense a CSM is Sufficient to Choke a Jet?*, *The Astrophysical Journal* **900** (9, 2020) .
[104] H.-N. He, A. Kusenko, S. Nagataki, Y.-Z. Fan and D.-M. Wei, *Neutrinos from Choked Jets Accompanied by Type-II Supernovae*, *The Astrophysical Journal* **856** (3, 2018) .
[105] N. Senno, K. Murase and P. Mészáros, *Constraining high-energy neutrino emission from choked jets in stripped-envelope supernovae*, *Journal of Cosmology and Astroparticle Physics* **2018** (1, 2018) .
[106] S. N. Shore, *Neutron Stars*, in *Encyclopedia of Physical Science and Technology (Third edition)*. third ed., 2003.
[107] L. Tolos and L. Fabbietti, *Strangeness in Nuclei and Neutron Stars*, *Progress in Particle and Nuclear Physics* **112** (2, 2020) .
[108] J. M. Lattimer and M. Prakash, *The Physics of Neutron Stars*, *Science* **304** (4, 2004) 536–542.
[109] M. Kutschera and H. Niewodniczański, *NEUTRON STARS: FORMATION AND STRUCTURE * * *, *Acta Phys. Polon.* **B29** (1998) 25–46.
[110] N. Yasutake, M.-A. Hashimoto and Y. Eriguchi, *Possible Evolutionary Transition from Rapidly Rotating Neutron Stars to Strange Stars Due to Spin-Down*, *Progress of Theoretical Physics* **113** (2005) .
[111] N. Yasutake, M.-a. Hashimoto and Y. Eriguchi, *Possible Evolutionary Transition from Rapidly Rotating Neutron Stars to Strange Stars Due to Spin-Down*, *Progress of Theoretical Physics* **113** (5, 2005) 953–962.
[112] S. Rosswog and M. Liebendörfer, *High-resolution calculations of merging neutron stars - II. Neutrino emission*, *Monthly Notices of the Royal Astronomical Society* **342** (7, 2003) 673–689.
[113] K. Hotokezaka, K. Kyutoku, H. Okawa, M. Shibata and K. Kiuchi, *Binary Neutron Star Mergers: Dependence on the Nuclear Equation of State*, *Phys. Rev. D* **83** (5, 2011) .
[114] B. Abbott, R. Abbott, T. Abbott, F. Acernese, K. Ackley et al., *GW170817: Measurements of Neutron Star Radii and Equation of State*, *Physical Review Letters* **121** (10, 2018) 161101.
[115] D. M. Siegel, *GW170817 –the first observed neutron star merger and its kilonova: Implications for the astrophysical site of the r-process*, *The European Physical Journal A* **55** (11, 2019) 203.
[116] K. Kyutoku and K. Kashiyama, *Detectability of thermal neutrinos from binary neutron-star mergers and implication to neutrino physics*, *Phys. Rev. D* **97** (2018) .
[117] V. Paschalidis, Z. B. Etienne and S. L. Shapiro, *Importance of cooling in triggering the collapse of hypermassive neutron stars*, *Phys. Rev. D* **86** (8, 2012) .
[118] E. Burns, *Neutron star mergers and how to study them*, 12, 2020. 10.1007/s41114-020-00028-7.
[119] M. Cusinato, F. M. Guercilena, A. Perego, D. Logoteta, D. Radice et al., *Neutrino emission from binary neutron star mergers: characterising light curves and mean energies*, *European Physical Journal A* **58** (5, 2022) .
[120] M.-R. Wu, I. Tamborra, O. Just and H.-T. Janka, *Imprints of neutrino-pair flavor conversions on nucleosynthesis in ejecta from neutron-star merger rem-*

nants, *Phys. Rev. D* **96** (11, 2017) .
[121] F. Foucart, R. Haas, M. D. Duez, E. O'Connor, C. D. Ott et al., *Low mass binary neutron star mergers : gravitational waves and neutrino emission*, *Phys. Rev. D* **93** (10, 2015) .
[122] F. Foucart, M. B. Deaton, M. D. Duez, E. O'Connor, C. D. Ott et al., *Neutron star-black hole mergers with a nuclear equation of state and neutrino cooling: Dependence in the binary parameters*, *Phys. Rev. D* **90** (5, 2014) .
[123] G. J. Mathews, A. Kedia, H. I. Kim and I. S. Suh, *Neutron Star Mergers and the Quark Matter Equation of State*, in *15th Conference on Quark Confinement and the Hadron Spectrum, Confinement 2022*, EDP Sciences - Web of Conferences, 2022. DOI.
[124] E. Pian, P. D'Avanzo, S. Benetti, M. Branchesi, E. Brocato et al., *Spectroscopic identification of r-process nucleosynthesis in a double neutron star merger*, *Nature* **551** (10, 2017) 67–70.
[125] S. Dichiara, C. Guidorzi, F. Frontera and L. Amati, *A SEARCH FOR PULSATIONS IN SHORT GAMMA-RAY BURSTS TO CONSTRAIN THEIR PROGENITORS*, *The Astrophysical Journal* **777** (10, 2013) 132.
[126] S. S. Bavera, T. Fragos, E. Zapartas, E. Ramirez-Ruiz, P. Marchant et al., *Probing the progenitors of spinning binary black-hole mergers with long gamma-ray bursts*, *Astronomy & Astrophysics* **657** (1, 2022) L8.
[127] T. Liu, W. M. Gu and B. Zhang, *Neutrino-dominated accretion flows as the central engine of gamma-ray bursts*, *New Astronomy Reviews* **79** (11, 2017) 1–25.
[128] X.-Y. Wang and P. Mészáros, *GRB PRECURSORS IN THE FALLBACK COLLAPSAR SCENARIO*, *ApJ* **670** (2007) .
[129] M. Charisi, S. Márka and I. Bartos, *Catalogue of isolated emission episodes in gamma-ray bursts from Fermi, Swift and BATSE*, *Monthly Notices of the Royal Astronomical Society* **448** (4, 2015) 2624–2633.
[130] Y.-F. Wei, T. Liu and C.-Y. Song, *Black Hole Hyperaccretion in Collapsars. I. MeV Neutrinos*, *The Astrophysical Journal* **878** (6, 2019) 142.
[131] T. Liu, B. Zhang, Y. Li, R. Y. Ma and L. Xue, *Detectable MeV neutrinos from black hole neutrino-dominated accretion flows*, *Physical Review D* **93** (6, 2016) .
[132] F. Halzen and G. Jaczko, *Neutrinos from Gamma Ray Bursts*, *Phys. Rev. D* **54** (1996) .
[133] J. D. Salmonson and J. R. Wilson, *A MODEL OF SHORT GAMMA-RAY BURSTS: HEATED NEUTRON STARS IN CLOSE BINARY SYSTEMS*, *ApJ* **578** (2002) 310–316.
[134] S. Razzaque, P. Mészáros and B. Zhang, *GeV AND HIGHER ENERGY PHOTON INTERACTIONS IN GAMMA-RAY BURST FIREBALLS AND SURROUNDINGS*, *ApJ* **613** (2004) 1072–1078.
[135] A. V. Borisov and P. E. Sizin, *Plasmon decay to a neutrino pair via neutrino electromagnetic moments in a strongly magnetized medium*, in *Particle Physics at the Year of Centenary of Bruno Pontecorvo*, pp. 122–124, 6, 2015. DOI.
[136] R. D. Blandford and R. L. Znajek, *Electromagnetic extraction of energy from Kerr black holes*, *Monthly Notices of the Royal Astronomical Society* **179** (7,

1977) 433–456.
[137] X. Cao, E.-W. Liang and Y.-F. Yuan, *EPISODIC JET POWER EXTRACTED FROM A SPINNING BLACK HOLE SURROUNDED BY A NEUTRINO-DOMINATED ACCRETION FLOW IN GAMMA-RAY BURSTS*, *The Astrophysical Journal* **789** (6, 2014) 129.
[138] C. Y. Song, T. Liu and Y. F. Wei, *Neutrinos and gravitational waves from magnetized neutrino-dominated accretion discs with magnetic coupling*, *Monthly Notices of the Royal Astronomical Society* **494** (5, 2020) 3962–3970.
[139] S. Woosley and J. Bloom, *The Supernova–Gamma-Ray Burst Connection*, *Annual Review of Astronomy and Astrophysics* **44** (9, 2006) 507–556.
[140] J. L. Hewett, H. Weerts, K. S. Babu, J. Butler, B. Casey et al., *Planning the Future of U.S. Particle Physics (Snowmass 2013): Chapter 2: Intensity Frontier*, *arXiv* (1, 2014) .
[141] J. A. Formaggio and G. P. Zeller, *From eV to EeV: Neutrino Cross Sections Across Energy Scales*, *Reviews of Modern Physics* **84** (9, 2012) .
[142] K. Scholberg, *Supernova Neutrino Detection*, *Annual Review of Nuclear and Particle Science* **62** (11, 2012) 81–103.
[143] G.-y. Huang and Q. Liu, *Hunting the Glashow Resonance with PeV Neutrino Telescopes*, *Journal of Cosmology and Astroparticle Physics* **2020** (12, 2020) .
[144] M. G. Aartsen, R. Abbasi, M. Ackermann, J. Adams, J. A. Aguilar et al., *Detection of a particle shower at the Glashow resonance with IceCube*, *Nature* **591** (3, 2021) 220–224.
[145] I. Frank and I. Tamm, *Coherent Visible Radiation of Fast Electrons Passing Through Matter*, in *Selected Papers*, pp. 29–35. Springer Berlin Heidelberg, Berlin, Heidelberg, 1991. DOI.
[146] D. Zaborov, *High-energy neutrino astronomy and the Baikal-GVD neutrino telescope*, *Physics of Atomic Nuclei* **84** (9, 2021) 513–518.
[147] Y. Wang, *Neutrino Detectors: Present and Future*, in *Physics Procedia*, vol. 37, pp. 22–33, Elsevier B.V., 2012. DOI.
[148] C. Kraus and S. J. Peeters, *The rich neutrino programme of the SNO+ experiment*, *Progress in Particle and Nuclear Physics* **64** (4, 2010) 273–277.
[149] L. Cadonati, F. P. Calaprice and M. C. Chen, *Supernova Neutrino Detection in Borexino*, *Astroparticle Physics* **16** (2, 2002) 361–372.
[150] F. An, G. An, Q. An, V. Antonelli, E. Baussan et al., *Neutrino Physics with JUNO*, *Journal of Physics G: Nuclear and Particle Physics* **43** (2, 2016) .
[151] T. N. The NOvA Collaboration and D. Ayres, *NOvA Proposal to Build a 30 Kiloton Off-Axis Detector to Study Neutrino Oscillations in the Fermilab NuMI Beamline*, *arXiv* (3, 2005) .
[152] DUNE collaboration, B. Abi, R. Acciarri, M. A. Acero, G. Adamov et al., *Supernova Neutrino Burst Detection with the Deep Underground Neutrino Experiment*, .
[153] K. Zuber, *HALO, a supernova neutrino observatory*, *Nuclear and Particle Physics Proceedings* **265-266** (8, 2015) 233–235.
[154] N. Raj, V. Takhistov and S. J. Witte, *Pre-Supernova Neutrinos in Large Dark Matter Direct Detection Experiments*, *Physical Review D* **101** (2, 2020) .
[155] M. G. Aartsen, M. Ackermann, J. Adams, J. A. Aguilar, M. Ahlers et al., *Measurement of atmospheric tau neutrino appearance with IceCube DeepCore*,

Physical Review D **99** (2, 2019) .
[156] IceCube Collaboration, M. G. Aartsen, M. Ackermann, J. Adams, J. A. Aguilar et al., *The IceCube Neutrino Observatory: Instrumentation and Online Systems*, *Journal of Instrumentation* **12** (12, 2017) .
[157] A. Achterberg, M. Ackermann, J. Adams, J. Ahrens, K. Andeen et al., *First Year Performance of The IceCube Neutrino Telescope IceCube Collaboration*, *Astroparticle Physics* (2006) 155–173.
[158] D. Chirkin and W. Rhode, *Propagating leptons through matter with Muon Monte Carlo (MMC)*, *arXiv* (2016) .
[159] Nadege Iovine, *Combined Search for Neutrinos from Dark Matter Annihilation in the Galactic Centre using IceCube and ANTARES*. PhD thesis, University of Mons, Mons, 2017.
[160] U. F. Katz and C. Spiering, *High-energy neutrino astrophysics: Status and perspectives*, 7, 2012. 10.1016/j.ppnp.2011.12.001.
[161] S. Sclafani and M. Hünnefeld, *A Search for Neutrino Sources with Cascade Events in IceCube*, in *37th International Cosmic Ray Conference*, 7, 2021. DOI.
[162] D. F. Cowen, *Tau neutrinos in IceCube*, *Journal of Physics: Conference Series* **60** (3, 2007) 227–230.
[163] J. L. Kelley, *Event triggering in the IceCube data acquisition system*, in *AIP Conference Proceedings*, vol. 1630, pp. 154–157, American Institute of Physics Inc., 2014. DOI.
[164] J. M. Santander, *Observation of Cosmic-Ray Anisotropy at TeV and PeV Energies in the Southern Sky*. PhD thesis, University of Wisconsin-Madison, Madison, 2013.
[165] M. G. Aartsen, G. C. Hill, A. Kyriacou, S. Robertson, A. Wallace et al., *Measurement of the multi-TeV neutrino interaction cross-section with IceCube using Earth absorption*, *Nature* **551** (11, 2017) 596–600.
[166] C. Evoli, *The Cosmic-Ray Energy Spectrum*, 12, 2020. 10.5281/ZENODO.4396125.
[167] M. G. Aartsen, M. Ackermann, J. Adams, J. A. Aguilar, M. Ahlers et al., *Atmospheric and Astrophysical Neutrinos above 1 TeV Interacting in IceCube*, *Physical Review D* **91** (1, 2015) .
[168] V. Valković, *Radioactive Nuclides in Nature*, in *Radioactivity in the Environment*, pp. 5–32. Elsevier, 2000. DOI.
[169] A. Schukraft, *A view of prompt atmospheric neutrinos with IceCube*, *Nuclear Physics B Proceedings Supplement* (2, 2013) .
[170] R. Enberg, M. H. Reno and I. Sarcevic, *Prompt neutrino fluxes from atmospheric charm*, *Physical Review D* (6, 2008) .
[171] ANTARES Collaboration, *A Deep Sea Telescope for High Energy Neutrinos*, .
[172] D. Freiherr and H. Von Zuydtwyck, *HitSpooling: An Improvement for the Supernova Neutrino Detection System in IceCube*, tech. rep., Deutsche Physikalische Gesellschaft., 2015.
[173] B. Riedel, *Modeling and Understanding Supernova Signals in the IceCube Neutrino Observatory*. PhD thesis, University of Wisconsin-Madison, Madison, 10, 2014.
[174] V. V. Baum, *Search for Low Energetic Neutrino Signals from Galactic*

Supernovae and Collisionally Heated Gamma-Ray Bursts with the IceCube Neutrino Observatory. PhD thesis, Mainz University, Mainz, 2017. 10.25358/openscience-1372.

[175] V. V. Baum, *Search for Low Energetic Neutrino Signals from Galactic Supernovae and Collisionally Heated Gamma-Ray Bursts with the IceCube Neutrino Observatory*. PhD thesis, 2017.

[176] M. G. Aartsen, R. Abbasi, Y. Abdou, M. Ackermann, J. Adams et al., *An improved data acquisition system for supernova detection with IceCube*, in *33RD INTERNATIONAL COSMIC RAY CONFERENCE*, vol. 27, p. 0444, 2013.

[177] B. Riedel, *Modeling and Understanding Supernova Signals in the IceCube Neutrino Observatory*. PhD thesis, 2014.

[178] S. Olofsson and E. Setterquist, *Investigation into the anomalous trigger rates in the IceCube Neutrino Observatory on Febraury 5th 2013*, tech. rep., 2013.

[179] G. Kroll, B. Riedel and V. Baum, *On the detection of galactic core collapse supernovae with IceCube*, in *33RD INTERNATIONAL COSMIC RAY CONFERENCE*, p. 0445, 2013.

[180] R. Abbasi, M. Ackermann, J. Adams, S. K. Agarwalla, J. A. Aguilar et al., *Search for Galactic Core-collapse Supernovae in a Decade of Data Taken with the IceCube Neutrino Observatory*, *The Astrophysical Journal* **961** (1, 2024) 84.

[181] S. Tilav, T. K. Gaisser, D. Soldin and P. Desiati, *Seasonal variation of atmospheric muons in IceCube*, .

[182] R. Abbasi, Y. Abdou, T. Abu-zayyad, M. Ackermann, J. Adams et al., *IceCube – Astrophysics and Astroparticle Physics at the South Pole*, in *32ND INTERNATIONAL COSMIC RAY CONFERENCE*, vol. 36, 2011.

[183] R. Cross, A. Fritz and S. Griswold, *Eleven Year Search for Supernovae with the IceCube Neutrino Observatory*, in *International Cosmic Ray Conference*, Proceedings of Science, 2019. DOI.

[184] S. Griswold, S. BenZvi, N. Uberoi and R. Cross, *ASTERIA: A Supernova TEst Routine for IceCube Analysis*, 7, 2020.

[185] M. D. Fulton, S. J. Smartt, L. Rhodes, M. E. Huber, V. A. Villar et al., *The Optical Light Curve of GRB 221009A: The Afterglow and the Emerging Supernova*, *The Astrophysical Journal Letters* **946** (3, 2023) L22.

[186] S. Lesage, P. Veres, M. S. Briggs, A. Goldstein, D. Kocevski et al., *Fermi-GBM Discovery of GRB 221009A: An Extraordinarily Bright GRB from Onset to Afterglow*, *The Astrophysical Journal Letters* **952** (8, 2023) L42.

[187] M. A. Williams, J. A. Kennea, S. Dichiara, K. Kobayashi, W. B. Iwakiri et al., *GRB 221009A: Discovery of an Exceptionally Rare Nearby and Energetic Gamma-Ray Burst*, *The Astrophysical Journal Letters* **946** (3, 2023) L24.

[188] Z. Cao, F. Aharonian, Q. An, Axikegu, L. X. Bai et al., *A tera–electron volt afterglow from a narrow jet in an extremely bright gamma-ray burst*, *Science* **380** (6, 2023) 1390–1396.

[189] E. Burns, D. Svinkin, E. Fenimore, D. A. Kann, J. F. Agüí Fernández et al., *GRB 221009A: The BOAT*, *The Astrophysical Journal Letters* **946** (3, 2023) L31.

[190] B. Stern and I. Tkachev, *GRB 221009A, its precursor and two afterglows in the Fermi data*, *MNRAS* **000** (3, 2023) 1–5.

[191] B. J. Morsony, D. Lazzati and M. C. Begelman, *TEMPORAL AND ANGULAR PROPERTIES OF GAMMA-RAY BURST JETS EMERGING FROM MASSIVE STARS*, *ApJ* **665** (2007) 569–598.
[192] X.-Y. Wang, Z. Li, E. Waxman and P. Mészáros, *NONTHERMAL GAMMA-RAY/X-RAY FLASHES FROM SHOCK BREAKOUT IN GAMMA-RAY BURST-ASSOCIATED SUPERNOVAE*, *ApJ* **664** (2007) 1026–1032.
[193] M. Modjaz, C. P. Gutierrez and I. Arcavi, *New Regimes in the Observation of Core-Collapse Supernovae*, *Nature* **3** (8, 2019) 717–724.
[194] E. Nakar and R. Sari, *Relativistic shock breakouts - A variety of gamma-ray flares: From low-luminosity gamma-ray bursts to type ia supernovae*, *Astrophysical Journal* **747** (3, 2012) .
[195] X.-Y. Wang, Z. Li, E. Waxman and P. Mészáros, *NONTHERMAL GAMMA-RAY/X-RAY FLASHES FROM SHOCK BREAKOUT IN GAMMA-RAY BURST-ASSOCIATED SUPERNOVAE*, *ApJ* **664** (2007) 1026–1032.
[196] X.-Y. Wang and P. Mészá Ros, *GeV PHOTONS FROM THE UPSCATTERING OF SUPERNOVA SHOCK BREAKOUT X-RAYS BY AN OUTSIDE GAMMA-RAY BURST JET*, tech. rep., 2006.
[197] G. J. Feldman and R. D. Cousins, *A Unified Approach to the Classical Statistical Analysis of Small Signals Typeset using REVT E X 1*, *Phys. Rev. D* **57** (1999) .
[198] I. Tamborra, B. Mueller, L. Huedepohl, H.-T. Janka and G. Raffelt, *High-resolution supernova neutrino spectra represented by a simple fit*, *Phys. Rev. D.* **86** (11, 2012) .
[199] A. Kheirandish, A. Pizzuto and J. Vandenbroucke, *Searches for neutrinos from fast radio bursts with IceCube*, *Proceedings of Science(ICRC 2019)* (8, 2019) .
[200] M. G. Aartsen, M. Ackermann, J. Adams, J. A. Aguilar, M. Ahlers et al., *A Search for MeV to TeV Neutrinos from Fast Radio Bursts with IceCube*, *The Astrophysical Journal* **890** (2, 2020) 111.
[201] D. Turcan, *Search for Neutrinos from Gamma-Ray Bursts Using Super-Kamiokande*, in *28th International Cosmic Ray Conference*, pp. 2713–2716, 2003.
[202] S. Fukuda, Y. Fukuda, M. Ishitsuka, Y. Itow, T. Kajita et al., *SEARCH FOR NEUTRINOS FROM GAMMA-RAY BURSTS USING SUPER-KAMIOKANDE*, *The Astrophysical Journal* **578** (2002) 317–324.
[203] LIGO/Virgo, *GraceDB Public Alert S200114f*, 1, 2020.
[204] E. Abdikamalov, G. Pagliaroli and D. Radice, *Gravitational Waves from Core-Collapse Supernovae*, in *Handbook of Gravitational Wave Astronomy*. 10, 2022. DOI.
[205] LIGO-Virgo-KAGRA, *LIGO, VIRGO AND KAGRA OBSERVING RUN PLANS*, 2024.
[206] LIGO-Virgo-KAGRA, *LVK Public Alerts Analysis*, 2023.
[207] The LIGO Scientific Collaboration, the Virgo Collaboration, B. P. Abbott, R. Abbott, T. D. Abbott et al., *GWTC-1: A Gravitational-Wave Transient Catalog of Compact Binary Mergers Observed by LIGO and Virgo during the First and Second Observing Runs*, *Physical Review X* **9** (11, 2019) .
[208] R. Abbott, T. Abbott, F. Acernese, K. Ackley, C. Adams et al., *GWTC-2.1: Deep extended catalog of compact binary coalescences observed by LIGO and*

Virgo during the first half of the third observing run, *Physical Review D* **109** (1, 2024) 022001.

[209] R. Abbott, T. Abbott, F. Acernese, K. Ackley, C. Adams et al., *GWTC-3: Compact Binary Coalescences Observed by LIGO and Virgo during the Second Part of the Third Observing Run*, *Physical Review X* **13** (12, 2023) 041039.

[210] A. Fritz, *Kernkollaps-Supernovae: Eine Suche mit dem IceCube Neutrino-Observatorium*. PhD thesis, Johannes Gutenberg-Universitat Mainz, Mainz, 6, 2022.

[211] E. Kankare, S. Mattila, S. Ryder, M. A. Perez-Torres, A. Alberdi et al., *Discovery of a very highly extinguished supernova in a luminous infrared galaxy*, *The Astrophysical Journal* **689** (11, 2008) .

[212] O. D. Fox, H. Khandrika, D. Rubin, C. Casper, G. Z. Li et al., *A Spitzer Survey for Dust-Obscured Supernovae*, *Monthly Notices of the Royal Astronomical Society* **506** (9, 2021) 4199–4209.

[213] F. Mannucci, M. Della Valle and N. Panagia, *How many supernovae are we missing at high redshift?*, *Monthly Notices of the Royal Astronomical Society* **377** (2007) 1229–1235.

[214] IceCube Collaboration, R. Abbasi, M. Ackermann, J. Adams, J. A. Aguilar et al., *IceCube Data for Neutrino Point-Source Searches Years 2008-2018*, *arXiv* (1, 2021) .

[215] R. Abbasi, M. Ackermann, J. Adams, J. A. Aguilar, M. Ahlers et al., *The IceCube high-energy starting event sample: Description and flux characterization with 7.5 years of data*, *Physical Review D* **104** (7, 2021) .

[216] D. A. Perley, C. Fremling, J. Sollerman, A. A. Miller, A. S. Dahiwale et al., *The Zwicky Transient Facility Bright Transient Survey. II. A Public Statistical Sample for Exploring Supernova Demographics*, *The Astrophysical Journal* **904** (2020) .

[217] B. J. Shappee, J. L. Prieto, D. Grupe, C. S. Kochanek, K. Z. Stanek et al., *THE MAN BEHIND THE CURTAIN: X-RAYS DRIVE THE UV THROUGH NIR VARIABILITY IN THE 2013 ACTIVE GALACTIC NUCLEUS OUTBURST IN NGC 2617*, *The Astrophysical Journal* **788** (5, 2014) 48.

[218] M. J. Graham, S. R. Kulkarni, E. C. Bellm, S. M. Adams, C. Barbarino et al., *The zwicky transient facility: Science objectives*, *Publications of the Astronomical Society of the Pacific* **131** (7, 2019) .

[219] T. Jayasinghe, C. S. Kochanek, K. Z. Stanek, B. J. Shappee, T. W. Holoien et al., *The ASAS-SN catalogue of variable stars I: The Serendipitous Survey*, *Monthly Notices of the Royal Astronomical Society* **477** (7, 2018) 3145–3163.

[220] R. Abbasi, Y. Abdou, T. Abu-Zayyad, J. Adams, J. A. Aguilar et al., *Constraints on high-energy neutrino emission from SN 2008D*, *Astronomy & Astrophysics* **527** (3, 2011) A28.

[221] M. Aartsen and Icecube Collaboration, *IceCube-Gen2: The Window to the Extreme Universe*, *Journal of Physics G: Nuclear and Particle Physics* **48** (4, 2021) .

Acta Universitatis Upsaliensis

Digital Comprehensive Summaries of Uppsala Dissertations from the Faculty of Science and Technology 2426

Editor: The Dean of the Faculty of Science and Technology

A doctoral dissertation from the Faculty of Science and Technology, Uppsala University, is usually a summary of a number of papers. A few copies of the complete dissertation are kept at major Swedish research libraries, while the summary alone is distributed internationally through the series Digital Comprehensive Summaries of Uppsala Dissertations from the Faculty of Science and Technology. (Prior to January, 2005, the series was published under the title "Comprehensive Summaries of Uppsala Dissertations from the Faculty of Science and Technology".)

Distribution: publications.uu.se
urn:nbn:se:uu:diva-535303

ACTA UNIVERSITATIS
UPSALIENSIS
2024